UNIWERSYTET JANA KOCHANOWSKIEGO W KIELCACH

SZKOŁA DOKTORSKA

WYDZIAŁ NAUK ŚCISŁYCH I PRZYRODNICZYCH

INSTYTUT FIZYKI

Yehor Bondar

LAMBDA TRANSVERSE POLARIZATION IN PROTON–PROTON INTERACTIONS IN NA61/SHINE AT THE CERN SPS

**Doctoral dissertation prepared
under the supervision of
dr hab. Grzegorz Slawomir Stefanek
Auxiliary supervisor:
dr Tobiasz Czopowicz**

Kielce 2025

ACKNOWLEDGEMENTS

Yehor Bondar

Lambda transverse polarization in proton-proton interactions in NA61/SHINE at the CERN SPS

Abstract

The transverse polarization of Λ hyperons produced in inclusive collisions of unpolarized protons with unpolarized targets was first observed in the 1970s. For over 40 years, such studies have been conducted for proton collisions with various targets at widely varying beam energies (or beams) and for various hyperon production angles. Several theoretical models have been proposed to describe the experimental data in this regard. Nevertheless, the polarization mechanism of Λ particles and other hyperons remains incompletely understood.

The main goal of this thesis is to measure the Λ hyperon transverse polarization in proton-proton interactions at a beam momentum of 158 GeV/c in the fixed-target experiment NA61/SHINE at the CERN SPS. The NA61/SHINE Collaboration recorded these data in 2009- 2011. The project adapted methods for polarization studies used by other experiments to the NA61/SHINE case and developed techniques that are most suitable for this analysis. They were applied to a NA61/SHINE physics analysis for the first time.

The obtained results are compared to the phenomenological function fitted to many experimental data, as well as new results from CERN (LHC, SPS), DESY, and Fermilab experiments, and predictions from the theoretical model. The biases related to the detector acceptance, data preparation technique, and analysis methodology were corrected using Monte Carlo simulations with two models. It was also shown that the precession of Λ hyperons in a magnetic field is negligible. The systematic uncertainties were estimated and discussed. The measured transverse polarization is consistent with results from other experiments and the model predictions. Unfortunately, the current measurement, due to significant statistical and systematic uncertainties, does not resolve the tensions that arise from the results of previous experiments.

The methodology, techniques, and software elaborated in this work will be used for the analysis of the high-precision proton-proton interaction data to be recorded in 2025. Furthermore, the study of Λ transverse polarization can be extended by analyzing of the data on light ion collisions recorded by the NA61/SHINE Collaboration in 2025 and planned for after Long Shutdown 3 of the CERN accelerator complex.

Yehor Bondar

Polaryzacja poprzeczna hiperonów Lambda w zderzeniach proton-proton w eksperymencie NA61/SHINE przy akceleratorze CERN SPS

Streszczenie

Polaryzacja poprzeczna hiperonów Λ produkowanych w inkluzywnych zderzeniach niespolaryzowanych protonów z niespolaryzowanymi tarczami była obserwowana po raz pierwszy w latach 70 XX wieku. Od ponad 40 lat badania tego typu były i są prowadzone dla zderzeń protonów z różnymi tarczami przy bardzo różnej energii wiązki (lub wiązek) oraz dla różnych kątów produkcji hiperonów. Zaproponowano również kilka modeli teoretycznych opisujących dane eksperymentalne dla tego zagadnienia. Pomimo to mechanizm polaryzacji cząstek Λ oraz innych hiperonów nie jest w pełni zrozumiały.

Głównym celem niniejszej pracy jest pomiar poprzecznej polaryzacji hiperonu Λ w oddziaływaniach proton-proton przy pędzie wiązki 158 GeV/c w eksperymencie z nieruchomą tarczą NA61/SHINE przy akceleratorze CERN SPS. Dane te zostały zarejestrowane przez współpracę NA61/SHINE w latach 2009-2011. W ramach projektu dostosowano metody badań polaryzacji używane w innych eksperymentach do przypadku NA61/SHINE i opracowano techniki najlepiej pasujące do tej analizy. Zostały one po raz pierwszy użyte w analizie fizycznej w ramach eksperymentu NA61/SHINE.

Uzyskane wyniki porównano z funkcją fenomenologiczną dopasowaną do wielu danych eksperymentalnych, nowymi wynikami eksperymentów zrealizowanych w CERN (LHC, SPS), DESY i Fermilab oraz przewidywaniami modelu teoretycznego. Korekty związane z ograniczoną akceptacją detektora, techniką przygotowania danych i metodologią analizy wykonano za pomocą symulacji Monte Carlo z dwoma modelami. Wykazano również, że precesja hiperonów Λ w polu magnetycznym jest pomijalna. Oszacowano i szczegółowo omówiono niepewności systematyczne. Mierzona polaryzacja poprzeczna jest zgodna z wynikami innych eksperymentów i przewidywaniami modelu. Niestety, obecny pomiar obarczony znacznymi niepewnościami statystycznymi i systematycznymi, nie wyjaśnia rozbieżności pojawiających się w wynikach poprzednich eksperymentów.

Metodologia, techniki i oprogramowanie opracowane przy okazji tej pracy zostaną wykorzystane do analizy precyzyjnych danych dotyczących oddziaływań proton-proton, które zostaną zarejestrowane w 2025 r. Ponadto badanie polaryzacji poprzecznej hiperonów *Lambda* można będzie rozszerzyć na analizę danych dotyczących zderzeń lekkich jonów zarejestrowanych przez współpracę NA61/SHINE w 2025 r. i tych, które zostaną zebrane po trzecim długim postoju (Long Shutdown 3) kompleksu akceleratorów CERN.

Contents

Chapter 1

Introduction

Starting in the 1920s, experiments conducted by Otto Stern and Walther Gerlach led to the discovery of a previously unknown property of particles called spin. Despite simple physical interpretations like "internal angular momentum" or "property of a particle spinning around its own axis", spin is, in fact, a purely quantum property of the elementary particles. Nowadays, such an essential property in the quantum world has real significance in broad branches of applied natural science. Spin is especially important in particle physics. The transverse polarization of hyperons (baryons containing one or more strange s quarks), observed in unpolarized beams since the 1970s, is still under investigation. Over the decades, a wealth of experimental data has been collected for various hyperons and anti-hyperons, and numerous theoretical models have been proposed to explain the origin of this polarization. However, a complete and universally accepted understanding of the underlying mechanisms remains unclear, making it an active and compelling area of research. In particular, studies of the lightest hyperon, the Λ particle, in hadron collisions are particularly extensive due to its decay mode into proton and pion, where the proton tends to be emitted along the spin direction of the decaying Λ hyperon.

Changes in hyperon polarization were one of the earliest proposed signatures for probing the hot and dense nuclear matter in heavy-ion collisions. The observation of changes in transverse polarization in proton-proton, proton-nucleus, and nucleus-nucleus collisions may also help to indicate the beginning of the creation of large clusters of strongly interacting matter – the onset of QGP fireball [1, 2].

The possibility of studying these effects by the NA61/SHINE fixed target experiment at the Super Proton Synchrotron (SPS) located at the European Organization for Nuclear Research (CERN) [3] is the subject of this thesis. The NA61/SHINE detector is a large-acceptance spectrometer covering the forward hemisphere down to $p_{\mathrm{T}} \approx 0$ GeV/c. The experiment recorded about 60 million proton-proton interactions, providing an opportunity for measuring of Λ transverse polarization.

Furthermore, the comprehensive data collected by the NA61/SHINE collaboration during the Run 3 (2022–2025) at beam momentum 150A GeV/c (corresponding to $\sqrt{s_{NN}} \approx 16.8$ GeV) on O+O and Pb+Pb collisions as well as high-statistics $p+p$ interactions at 300 GeV/c ($\sqrt{s_{NN}} = 23.8$ GeV) will enable systematic studies of system size and energy dependence of the Λ transverse polarization and the verification of theoretical models' predictions. A detailed introduction to the hyperon polarization is provided in Chapter 2.

1.1 Structure of this thesis

Chapter 2 describes the theoretical basis of the thesis. Chapter 3 presents the NA61/SHINE facility at the CERN SPS, including its physics program, detector components, and the key aspects of the accelerator complex. Chapter 4 contains selected aspects of the data reconstruction. Chapter 5 focuses on the analysis of data. Chapter 6 is dedicated to the results on transverse polarization measurements and their comparison with the world data and theoretical models. Chapter 7 summarizes the results and presents the outlook for future studies. Supplementary information is given in Appendices A- D.

1.2 Author's contribution

This thesis presents pioneering measurements of the transverse polarization of Λ hyperons in proton-proton collisions at the beam momentum 158 GeV/c ($\sqrt{s}$ = 17.3 GeV) in the fixed-target experiment NA61/SHINE using the data recorded in 2009–2011.

For the measurement, I reconstructed the Λ candidate particles, evaluated potential biases associated with the selection cuts, extracted signal yields, corrected the yields for the detector acceptance and other biases, performed cross-checks, as well as estimated and discussed statistical and systematic uncertainties.

Besides the work presented in this thesis, I served as the deputy coordinator of the NA61/SHINE Monte Carlo group. I was responsible for the Monte Carlo data production for this analysis and others, as well as for enhancing the detector description and response simulation in the MC software.

I presented my results at the numerous NA61/SHINE collaboration meetings and the following conferences:

- The 21st Zimányi School Winter Workshop on Heavy Ion Physics, 06–10.12.2021, Budapest, Hungary. Oral presentation.
- The XXIXth International Conference on Ultra-relativistic Nucleus-Nucleus Collisions (Quark Matter 2022), 04–10.04.2022, Kraków, Poland. Poster.
- The New Trends in High-Energy and Low-x Physics, 01–05.09.2024, Sfantu Gheorghe, Romania. Oral presentation.
- The XXXIth International Conference on Ultra-relativistic Nucleus-Nucleus Collisions (Quark Matter 2025), 06–12.04.2025, Frankfurt am Main, Germany. Poster.
- The 21st International Conference on QCD in Extreme Conditions (XQCD 2025), 02—04.07.2025, Wroclaw, Poland. Poster.

I have published my results in the article:

- Y. Bondar and W. Florkowski. "Lambda transverse polarization in NA61/SHINE at the CERN SPS: feasibility studies". *Acta Phys. Polon. B*, vol. 55, no. 9-A1, 2024, DOI: 10.5506/APhysPolB.55.9-A1.

and has served as the Primary Investigator of the NCN PRELUDIUM grant. I am a co-author of 13 papers published by the NA61/SHINE collaboration since 2022.

Additionally, I actively participated in the detector commissioning in 2021 and the data-taking campaigns in 2021–2025, controlling the experimental conditions and the data acquisition process.

Chapter 2

Hyperon Polarization: Theory, Phenomology and Experimental Results

This chapter offers an overview of the theoretical and experimental status of hyperon transverse polarization, with a particular focus on the Λ hyperon. While a detailed understanding of the Standard Model is presumed, a summary is included in Appendix A.2 for reference. Section 2.1 covers the historical context of the strangeness and Λ discovery. In Sec. 2.2, basic properties of Λ baryon (hyperon) are reviewed, Sec. 2.3 introduces Λ and other hyperons' polarization. The last three Secs. 2.4, 2.5, and 2.6 briefly discuss other properties of hyperon polarization.

2.1 Historical Foundations

2.1.1 Spin discovery and the Stern-Gerlach experiment

The Stern-Gerlach experiment [4], conceived by Otto Stern in 1921 and successfully conducted with Walther Gerlach in early 1922, is a cornerstone in the history of quantum mechanics. This experiment demonstrated the quantization of angular momentum, revealing the intrinsic quantum properties of atomic-scale systems.

In the original experiment, a beam of silver atoms was sent through a spatially varying magnetic field. The atoms were deflected before they struck a detector screen, such as a glass slide. The magnetic field gradient deflected particles with non-zero magnetic moments from a straight path. The screen revealed discrete points of accumulation rather than a continuous distribution, indicating their quantized spin.

The Stern-Gerlach experiment contradicted the predictions of classical physics, which expected a continuous distribution of deflections. Instead, the experiment showed that particles possess an intrinsic angular momentum, known as spin. This spin is closely analogous to the angular momentum of a classically spinning object, but it takes only specific quantized values.

The discovery of spin predates its theoretical understanding. It was later understood that elementary particles can be divided into two classes: fermions and bosons. Fermions, such as electrons, protons, and neutrons, possess half-integer spin. In contrast, bosons, such as mesons and photons, possess integer spin (including zero).

The Stern-Gerlach experiment and the subsequent discovery of spin have had profound implications for the development of quantum mechanics. They have led to a deeper understanding of the quantum world and paved the way for advancements in fields such as quantum computing

and high-temperature superconductivity.

2.1.2 Strangeness and Λ discovery

The Λ hyperon was first detected in the cosmic-ray background in 1951, only five years after the initial evidence of the K^0-meson's existence. These particles are identifiable by their specific decay patterns and remain unseen until they decay due to their electrically neutral nature.

As research progressed, accelerator experiments became essential. At the Cosmotron in BNL, an intriguing discovery was made. Researchers utilized the large MIT multi-plate cloud chamber to measure the lifetime of Λ [5]. It was observed that the lifetime of both Λ and K^0 surpassed that of all previously discovered particles, except for neutrons. While, for instance, the Δ baryon rapidly decays after its creation (within 10^{-24} seconds), the Λ hyperon's mean lifetime is approximately 14 orders of magnitude longer. Furthermore, it was noted that these peculiar particles are always produced in pairs. Pais and Nishijima [6] provided an explanation for this phenomenon, attributing the production of strange particles to the strong force and their decay to the weak force. The associated production of these weakly decaying particles was further elucidated by Nishijima and Nakano [7–9]. They introduced an extra quantum number, termed η-number, strangeness S. For Λ, K^-, and $\bar{K}^0$, the strangeness S is -1, while for their antiparticles, S is 1. They proposed that strangeness is conserved in strong interactions. However, processes involving the weak force alter the strangeness number by one.

A more comprehensive explanation for the associated production of strangeness was offered within the quark model [10]. This model introduces a strange quark (s) with a strangeness content of $S = -1$ and its antiparticle ($\bar{s}$ with $S = 1$) as the sole carrier of strangeness. As the strong interactions mandate the conservation of strangeness, the production of a single strange hadron is forbidden. With increasing collision energy, more weakly decaying strange particles were discovered, which were given the names Σ, Ξ, and Ω. With the help of the quark model, one strange quark was assigned to Λ and Σ, two to Ξ, and three to Ω particles, thus also assigning the strangeness quantum number -1, -2, and -3, correspondingly. Proton, neutron and Δ baryons are strangeless ($S = 0$). The name *hyperon* was given to the baryons containing one or more strange quarks.

Subsequently, further research programs systematized our understanding of the properties of strange particles. The resurgence of strangeness exploration coincided with the theories on the quark-gluon plasma (QGP), where a significant change in the production of strangeness was predicted and observed. The Λ hyperon plays an important role in such studies.

2.1.3 V^0 identification

When Λ and K^0 particles decay, they generate a distinctive V-shaped energy deposition in a detector, resulting in what is known as V^0 decay. The "V" represents the decay topology, while the superscript "0" denotes the parent particle's charge. This pattern must be identified among numerous particle tracks to detect strange neutral particles. It involves pairing each positively

charged track with every negatively charged track. When these tracks converge at a certain point, they likely originate from a single decay vertex. If one track is positively charged and the other negatively charged, and their combined momentum points to the primary interaction vertex, they are likely either pions produced in K_S^0 decay or a $p\pi^-$ pair resulting from Λ decay.

Determining whether the unseen mother particle was Λ is challenging. Decays of Σ^0 present even more difficulties, as it is virtually impossible to distinguish this particle from Λ. Σ^0 decays electromagnetically into Λ and γ soon after its creation (mean lifetime $\tau_{\Sigma_0} = 7.4 \times 10^{-20}$ s). Therefore, in experimental particle physics, it is a common practice to measure a sum of Λ produced via strong interactions and Λ originating from Σ^0 decays [11].

2.2 Λ hyperon properties

The Λ hyperon consists of *uds* quarks, with a strangeness content of $S = -1$ and isospin $I = 0$. Its ground state exhibits positive parity and the spin value $J = 1/2$. The mass of the particle is $m_\Lambda = 1.115683(6)$ GeV and the mass difference between Λ and its antiparticle $\overline{\Lambda}$ is negligible [12]. The mean lifetime is $\tau = (2.632 \pm 0.020) \times 10^{-10}$ s, or $c\tau = 7.89$ cm. Table 2.1 presents the decay modes, with the most prominent one being the V^0 decay type, where more than half of the Λ decays lead to a final-state proton and π^-.

Decay modes	Fraction (Γ_i/Γ)
$p\pi^-$	**$(64.1 \pm 0.5)\%$**
$n\pi$	(35.9 ± 0.5) %
$n\gamma$	$(8.3 \pm 0.7) \times 10^{-4}$
$p\pi^-\gamma$	$(8.5 \pm 1.4) \times 10^{-4}$
$pe^-\nu_e$	$(8.34 \pm 0.14) \times 10^{-4}$
$p\mu^-\nu_\mu$	$(1.51 \pm 0.19) \times 10^{-4}$

Table 2.1: Λ decay modes. A fraction is defined as the ratio of the decay width of the mode to the total width Γ of the particle decay [12].

The most common production channels in nucleon-nucleon interactions resulting in Λ and Σ production, along with their respective energy thresholds, are as follows:

$$N + N \rightarrow \Lambda + K + N \qquad (\sqrt{s_{NN}} > 2.55 \text{ GeV}),$$
$$N + N \rightarrow \Sigma + K + N \qquad (\sqrt{s_{NN}} > 2.63 \text{ GeV}),$$
$$N + N \rightarrow \Lambda + K + \Delta \qquad (\sqrt{s_{NN}} > 2.88 \text{ GeV}),$$
$$N + N \rightarrow \Lambda + \overline{\Lambda} + N + N \qquad (\sqrt{s_{NN}} > 4.11 \text{ GeV}),$$

Non-direct (secondary) decay channels from other baryons are mainly from strange baryons,

for example:

$$\Sigma^0(uds) \rightarrow \Lambda + \gamma \,(c\tau = 22.2 \text{ pm})\,,$$
$$\Xi^0(uss) \rightarrow \Lambda + \pi^0 \,(c\tau = 8.71 \text{ cm})\,,$$
$$\Xi^-(dss) \rightarrow \Lambda + \pi^- \,(c\tau = 4.91 \text{ cm})\,,$$
$$\Omega^-(sss) \rightarrow \Lambda + K^- \,(c\tau = 2.46 \text{ cm})\,.$$

In the Λ decay to proton and π^-, the daughter proton distribution function has the following form:

$$\frac{dN}{d\Omega} = N_0 \frac{1}{4\pi}(1 + \alpha \cos\theta)\,, \tag{2.1}$$

where Ω is the solid angle, N_0 is normalization factor, θ is the angle between daughter proton momentum and Λ spin vector in the hyperon rest frame, and $\alpha = 0.747 \pm 0.009$ is the parameter of the Λ hyperon parity-violating weak decay asymmetry [12].

2.3 Hyperon transverse polarization

2.3.1 Definition of polarization

Three mutually orthogonal unit vectors define a Λ production plane coordinate system (see Fig. 2.1):

$$\hat{n}_x = \frac{\vec{p}_{\text{beam}} \times \vec{p}_\Lambda}{|\vec{p}_{\text{beam}} \times \vec{p}_\Lambda|}\,,$$
$$\hat{n}_z = \frac{\vec{p}_\Lambda}{|\vec{p}_\Lambda|}\,,$$
$$\hat{n}_y = \hat{n}_z \times \hat{n}_x\,, \tag{2.2}$$

where $\vec{p}_\Lambda$ is the Λ momentum in the laboratory frame, and $\vec{p}_{\text{beam}}$ is the incident beam proton momentum.

Figure 2.1: Production plane coordinate system.

The distributions of daughter protons in the Λ rest frame, using (2.1), might be described by the following formula:

$$\frac{1}{N_0}\frac{dN}{d\cos\theta_i} = f(\cos\theta_i) = \frac{1 + \alpha P_i \cos\theta_i}{2}\,, \tag{2.3}$$

where P_i ($i = x, y, z$) are components of the polarization vector $\vec{P}$, which describes the orientation and degree of spin polarization. The magnitude $|\vec{P}|$ quantifies the total polarization: $|\vec{P}| = 1$ represents a case where the spin of each Λ produced in collision is aligned along a specific

direction, while $|\vec{P}| < 1$ indicates partial polarization.

According to parity conservation in the strong interaction, P_y and P_z should be equal to zero if the incident proton beam is unpolarized. Thus, the measurements of P_y and P_z are typically used to check for experimental biases. In the NA61/SHINE experimental setup, the proton beam is unpolarized, so we expect the values P_y and P_z to be consistent with zero.

In the case of collisions involving identical unpolarized hadrons, such as in $p+p$ interactions, the hyperon polarization is an odd function of the Feynman-x x_F variable: $P(-x_F) = -P(x_F)$ due to the forward-backward symmetry. This implies $P(x_F = 0) = 0$. Feynman-x variable x_F is a dimensionless variable defined here as:

$$x_F = \frac{p_z^*}{p_{max}^*} \, , \tag{2.4}$$

where p_z^* is the longitudinal momentum of a produced particle in the center of mass (CMS) system, and p_{max}^* is the maximum possible longitudinal momentum. It is usually selected as the beam momenta in CMS $p_{max}^* = p_{beam}^* \approx \sqrt{s_{NN}}/2$ in the ultra-relativistic approximation. In this thesis, $p_{beam} = 158$ GeV/c in the lab frame and $p_{beam}^* = 8.5839$ GeV/c. Regions with positive ($x_F > 0$) and negative ($x_F < 0$) Feynman-x variable are referred to as *forward* and *backward* regions, respectively. Other variables used in this thesis are defined in Appendix A.1.

2.3.2 World data on transverse hyperon polarization

The polarization of Λ hyperons produced in inclusive reactions with unpolarized protons on unpolarized targets has been studied for more than 35 years. The polarization has been studied over a wide range of reaction energies and various production angles of the Λ's. The experiment at the CERN ISR has obtained a significant dependence of the polarization on the center–of–mass energy from $\sqrt{s} = 53$ GeV to $\sqrt{s} = 62$ GeV [1]. The polarization of Λ particles and other hyperons has now been observed and investigated in many high-energy experiments in $p+p$ and $p+N$ collisions, with a wide variety of hadron beams and kinematic settings at different initial nucleon energies ranging from 6 to ≈ 2000 GeV [13–23].

A relatively consistent kinematic behavior of the polarization in proton-nucleus collisions has been observed. The magnitude of polarization increases almost linearly with the transverse momentum p_T of the Λ hyperon, from $P_\Lambda = 0$ at $p_T = 0$ GeV/c up to a value of about 1 GeV/c, where a plateau is reached. The absolute polarization also rises with the Feynman variable x_F with values around -0.3 at $x_F \approx 0.6$. Data from several experiments are shown in Fig. 2.2. When measurements were conducted on proton and nuclear targets, a minor dependence of P on the nuclear mass number of the target was observed [2]. Λ polarization has been measured using diverse beams, including $e^\pm$, $\pi^\pm$, $K^\pm$, Σ^-, neutrons, photons, and neutrinos on various nuclear targets [13, 19, 24–30]. The measured polarization was found to be consistent with zero for both π^+ and K^+ beams. The polarization of Λ particles for $x_F > 0$ is almost always found to be negative, as in the original $p+p$ experiment [1]. A notable exception to this rule is the positive polarization measured in $K^- + p$ [13] and $\Sigma^- + N$ [19] interactions, where the beam particles
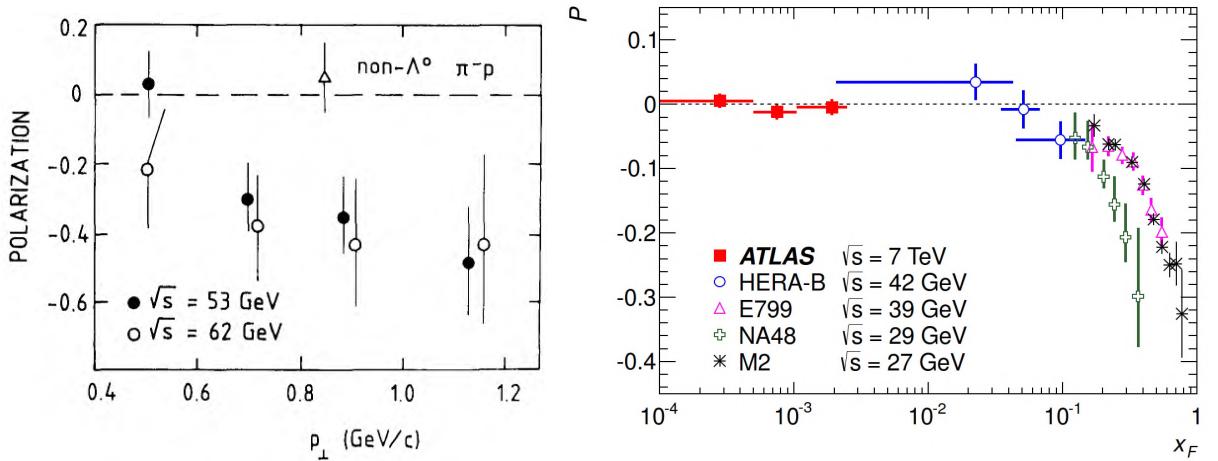
Figure 2.2: *Left*: The Λ transverse polarization in the $p+p$ interaction as a function of transverse momenta $p_\perp$ (Source: [1, 2]). *Right*: The Λ transverse polarization measured by ATLAS [14] compared to measurements from lower center-of-mass energy experiments. HERA-B data are taken from Ref. [15], NA48 from Ref. [16], E799 from Ref. [17], and M2 from Ref. [18].

contain valence[1] s quarks, and in quasireal photoproduction [20, 24, 31] measured by HERMES Collaboration. In 2018, the Belle collaboration [32] observed Λ (and $\overline{\Lambda}$) polarization in e^+e^- annihilation. The polarization was found to increase with the increase of the fraction of the outgoing quark (or antiquark) momentum carried by the hyperon. Since no initial-state hadrons are present, this phenomenon is attributed entirely to the hadronization process.

The similar behavior was observed for Ξ^0 (uss) and Ξ^- (dss) [33, 34], while displaying opposite sign for Σ^+ (uus) and Σ^- (dds) [35, 36]. Notably, the Σ^0 (uds) hyperon shares the polarization sign of $\Sigma^\pm$ despite having identical valence quark content to Λ [37]. Antihyperons produced in $p+N$ scattering contain no valence quarks in common with the beam and were expected to have no polarization. Indeed, the studies of Ω^- (sss) and $\overline{\Lambda}$ ($\overline{uds}$) show zero polarization [38, 39]. However, significant polarization is observed for reactions $p + N \to \overline{\Xi}^+$ and $p+p \to \overline{\Sigma}^-$ with the same sign and magnitude as those of the corresponding hyperons [40–42]. These observations have presented a decade-long puzzle in non-perturbative QCD. Figure 2.3 summarizes these findings, comparing: (*left*) hyperons sharing at least one valence quark with the proton beam, and (*right*) hyperons with no valence quark overlap with the beam.

The presence of longitudinal polarization P_z (along momentum) in a sample of Λ hyperons could be due to the Λs that are decay products of the Ξ^- and the parity violation in the Ξ decay will induce a non-vanishing longitudinal polarization in the Λ. Given the enhanced production of multi-strange antibaryons in a quark-gluon plasma (QGP), the longitudinal polarization of $\overline{\Lambda}$ hyperons has been suggested as a potential signature for QGP formation [44].

A comprehensive data review on hyperon polarization can be found in Refs. [2, 45, 46]. Currently, there are only a handful of results on Λ polarization in nucleus-nucleus interactions [21, 47–49], see Sec. 2.4.

---

[1]Valence quarks are the constituent quarks that determine the quantum numbers of a hadron. Sea quarks are transient quark-antiquark pairs that emerge from quantum fluctuations within the hadron and do not affect its overall quantum numbers.

9
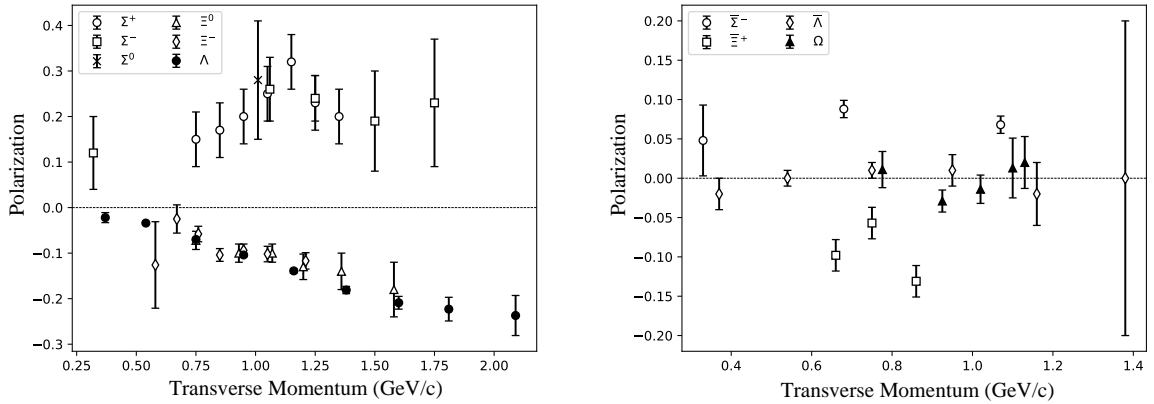
Figure 2.3: Transverse polarization of hyperons versus transverse momentum in fixed-target experiments. *Left*: Results for various hyperons in 400 GeV/c proton collisions (except Σ^0 at 28.5 GeV/c) from Refs. [33–38]. *Right*: Ω^- and antihyperon polarizations in 800 GeV/c proton collisions (except $\overline{\Lambda}$ at 400 GeV/c) from Refs. [38–40, 42]. Figures taken from Ref. [43].

2.3.3 Theoretical models describing hyperon transverse polarization

The phenomenon of transverse polarization of Λ and other hyperons has been addressed through various theoretical approaches, which can be broadly categorized into semiclassical descriptions based on the spin-orbit interaction in QCD. These are:

(i) Lund Model [50, 51],

(ii) DeGrand-Miettinen [52, 53],

(iii) SU(6) quark model [38, 54],

(iv) Regge phenomenology [26, 55, 56].

Detailed reviews of models can be found in Refs. [2, 57–60], and other models are presented in Refs. [61–64]. None of the models was able to account for the complete set of available measurements. In particular, no model could explain the puzzling pattern of antihyperon polarization, shown in Fig. 2.3.

The notably different approach is the framework of QCD factorization, initially developed by Sivers [65] and Collins [66]. These approaches use the spin-dependent and transverse momentum-dependent (TMD) functions of distribution of quarks in a polarized proton [65] or the functions of fragmentation of polarized quarks into hadrons [66], or higher-twist contribution [67–69]. Broader reviews are available at Ref. [70].

Lund String Fragmentation Model

The Lund string fragmentation model [51] offers a phenomenological description of hadronization inspired by the QCD principle of color confinement. In this framework, the interaction between a separating quark (q) and antiquark ($\bar{q}$) is modeled as a one-dimensional relativistic color flux

10

tube, or "string". The potential energy of this string, $V(d) = \kappa d$, increases linearly with the separation distance d, where $\kappa \approx 1$ GeV/fm is the string tension. As the string stretches, it eventually breaks by producing a new $q'\bar{q}'$ pair from the vacuum. This fragmentation process repeats until the remaining string segments form color-neutral hadrons.

The model explains the transverse polarization of Λ hyperons through the dynamics of proton fragmentation, as depicted in Fig. 2.4.
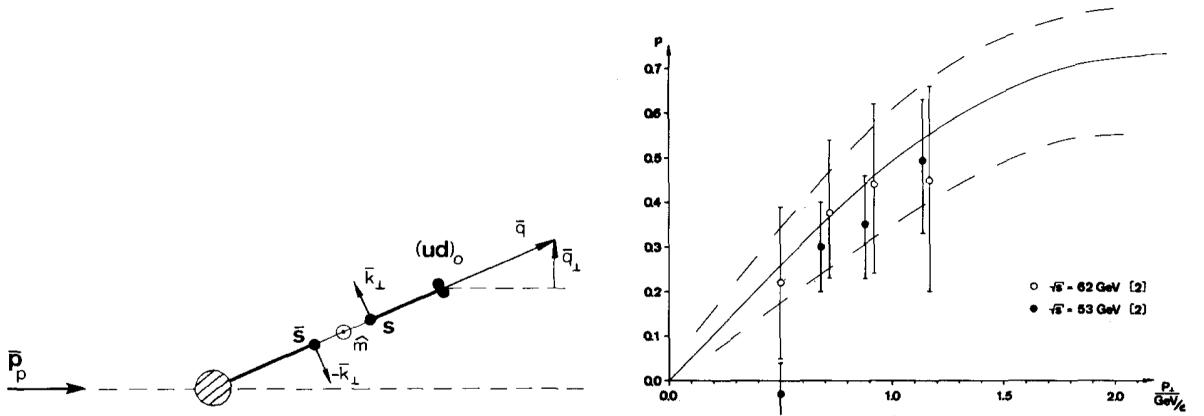

Figure 2.4: *Left*: A schematic picture of a scattered spin zero *ud*-diquark from proton. An $s\bar{s}$ pair is created from the color force field; their transverse momenta give rise to an orbital angular momentum in the direction to the reader. *Right*: The Λ transverse polarization P as a function of Λ transverse momentum. The solid line corresponds to the model prediction, while the dashed curves indicate its theoretical uncertainty. Data points are taken from [1]. Figures are taken from [50]. Due to the opposite sign convention, polarization is positive.

This framework makes distinct predictions for other hyperons based on their quark content and diquark spin structure. For the Σ^0, which contains a spin-one *ud* diquark, the model correctly predicts a smaller, oppositely signed polarization ($P_{\Sigma^0} \approx -1/3 P_\Lambda$). Furthermore, the model is consistent with the observed zero polarization for $\overline{\Lambda}$ and Ω^-, as their production mechanisms do not involve a spectator diquark from the incident proton.

DeGrand-Miettinen model

The fundamental observation underlying the model is that the *s* quark involved in the recombination resides in the sea of the proton and carries a tiny fraction ($x_s \approx 0.1$) of its momentum. However, it is a valence quark in the Λ and must carry a large fraction ($\approx \frac{1}{3}$) of the Λ's momentum. Since the Λ also carries a large fraction x_F of the proton's momentum, recombination induces a significant increase in the longitudinal momentum of the *s* quark, from $x_s P$ to $\frac{1}{3} x_F P$.

At the same time, the *s* quark carries transverse momentum: on average, $p_{Ts} = p_{TD} = p_{T\Lambda}/2$, where p_{Ts}, p_{TD}, $p_{T\Lambda}$ are the transverse momenta of the *s* quark, the *ud* diquark, and Λ, respectively. Therefore, the velocity vector of the *s* quark is not parallel to the change in momentum induced by
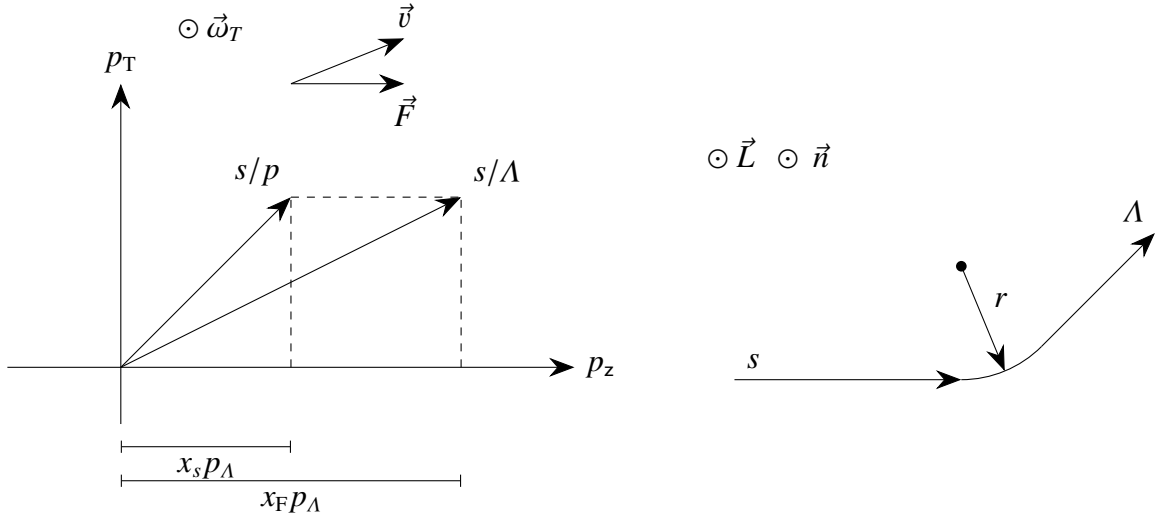
Figure 2.5: *Left*: Momentum vectors for the *s* quark in the scattering plane in the sea of the proton labeled as (s/p) and in the Λ (labeled as s/Λ). The recombination force $\vec{F}$ is along the beam direction, and the Thomas frequency $\vec{\omega}_T$ is out of the scattering plane. *Right*: Semiclassical trajectory of the *s* quark in an attractive potential showing the distance of the orbit from the origin r, and the orientations of the scattering plane $\vec{n}$ and of the particle's orbital angular momentum $\vec{L}$ (out of the page).

recombination. That being the case, the quark's spin will feel the effects of Thomas precession:

$$\vec{\omega}_T = \frac{\gamma}{\gamma + 1} \frac{\vec{F}}{m_q} \times \vec{v}, \tag{2.5}$$

where $\vec{F}$ is the force applied by the di-quark, $\vec{v}$ is the *s* quark's velocity and $\gamma = (1 - v^2)^{-1/2}$ is the Lorenz factor. It results in the effective interaction potential:

$$U = \vec{S} \cdot \vec{\omega}_T = -\frac{1}{r} \frac{\partial V}{\partial r} \vec{L} \cdot \vec{S}, \tag{2.6}$$

where $V(r)$ is the potential, $\vec{L}$ and $\vec{S}$ are the orbital angular momentum and spin of *s* quark. As the potential is attractive, $\vec{L} \cdot \vec{n} > 0$ where $\vec{n} = \vec{p}_{\text{beam}} \times \vec{p}_\Lambda$ is normal to the production plane, and $\vec{n} \cdot \vec{S} > 0$. This leads to the polarization [53]:

$$P(p_T, x_F) = -\frac{3}{\Delta x_0} \frac{1 - 3\xi}{((1 + 3\xi)/2)^2} \frac{1}{M^2} p_T, \tag{2.7}$$

where

$$M^2 = \frac{m_d^2 + p_{TD}^2}{1 - \xi} + \frac{m_s^2 + p_{Ts}^2}{\xi} - m_\Lambda^2 - p_{T\Lambda}^2, \tag{2.8}$$

where $\xi(x_F) = \frac{x_s}{x_F} = \frac{1}{3}(1 - x_F) + 0.1 x_F$ is a fraction of *s* quark longitudinal momentum, $m_s = \frac{1}{2}$ GeV and $m_d = \frac{2}{3}$ GeV are masses of *s* quark and *ud* diquark, and $\Delta x_0 = 5$ GeV^{-1} is hadronic size scale.

The Thomas precession model provides predictions for hyperon polarization in various

collision systems [71]. The model establishes a simple rule for polarization signs: slow partons preferentially recombine with their spins oriented downward in the scattering plane. In contrast, fast partons recombine with spins upward (a consequence of the attractive potential reversing the orbital angular momentum L sign).

While the model correctly predicts polarization signs, it exhibits limitations in quantitative predictions. It predicts equal polarization magnitudes for $p+p \rightarrow \Lambda$ and $p+p \rightarrow \Xi^-$ processes. At the same time, experimental data indicate that the latter is approximately half as large. The predicted polarization magnitude for $K^-+p \rightarrow \Lambda$ matches $p+p \rightarrow \Lambda$, contrary to experimental observations of twice larger polarization. The model correctly predicts vanishing polarization for $\overline{\Lambda}$ and Ω^- in $p+p$ interactions (composed entirely of sea quarks) and in $\Sigma^-+p \rightarrow \overline{\Lambda}$, but fails for $\overline{\Xi}$ production.

Despite these limitations, the model successfully reproduces polarization data in the low-x_F region, which is particularly relevant for our measurements. This fact makes it an important theoretical reference for our analysis of hyperon polarization phenomena.

Scaling Law Behaviour: Phenomenological fit to data

Based on dimensional analysis, the polarization P for $p+N$ collisions can be expressed [46] as

$$P = A^\alpha F(p_T)D(x_{A+}, x_{A-}) = A^\alpha F(p_T)[G(x_{A+} - x_2) - \sigma G(x_{A-} + x_2)], \qquad (2.9)$$

where $x_{A\pm} = (x_R \pm x_F)/2$, $x_R = p^*/p^*_{max}$, p^* and p^*_{max} are the momentum of the produced hadron and the maximum possible value of it, respectively, in the c.m. reference frame, and A is the mass number of the target nucleus N. The functions $F(p_T)$ and $G(x_{A\pm})$ are intended to be determined through the analysis of experimental data. Additional shift x_2 and a signature parameter σ are introduced to take into account a possible violation of the relation $P(x_F) = -P(-x_F)$ for asymmetric $p+N$ collisions. For $p+p$ interactions, $x_2 \equiv 0$, $\sigma \equiv 1$, and $A^\alpha \equiv 1$.

As polarization saturates at $p_T \approx 1$ GeV/c, the expression $F(p_T) = (1 - e^{-\kappa p_T^3})$ was used, which is sharply rising for low p_T and is practically constant for higher p_T. For the $G(x_{A\pm})$, the expression

$$G(x_{A\pm}) = \frac{c}{2\omega} \sin{(\omega(x_{A\pm} - x_1))} \qquad (2.10)$$

was used to reproduce such features as an approximately linear dependence of P_Λ on the x_F and non-linear, sometimes oscillating behavior of the hyperon polarization for other reactions.

Consequently, a new phenomenological expression for Λ hyperon polarization for $p+p$ interactions is presented:

$$P(x_F, p_T) = c(1 - e^{-\kappa p_T^3}) \cos(\omega(x_R/2 - x_1)) \sin(\omega x_F/2)/\omega, \qquad (2.11)$$

where $x_1 = \eta_0 - \eta_1 e^{-\delta p_T^3}$, $\omega = 3.045$, $\eta_0 = 0.412$, $\eta_1 = 0.33$, $\delta = 4.7$, $c = -1.22$. These values were calculated via a fit of experimental data for $p+p$ and $p+N$ collisions with $\chi^2/N_{DOF} = 326.0/260$. This fitted curve, along with the experimental data used for fit, is presented in Fig. 2.6.
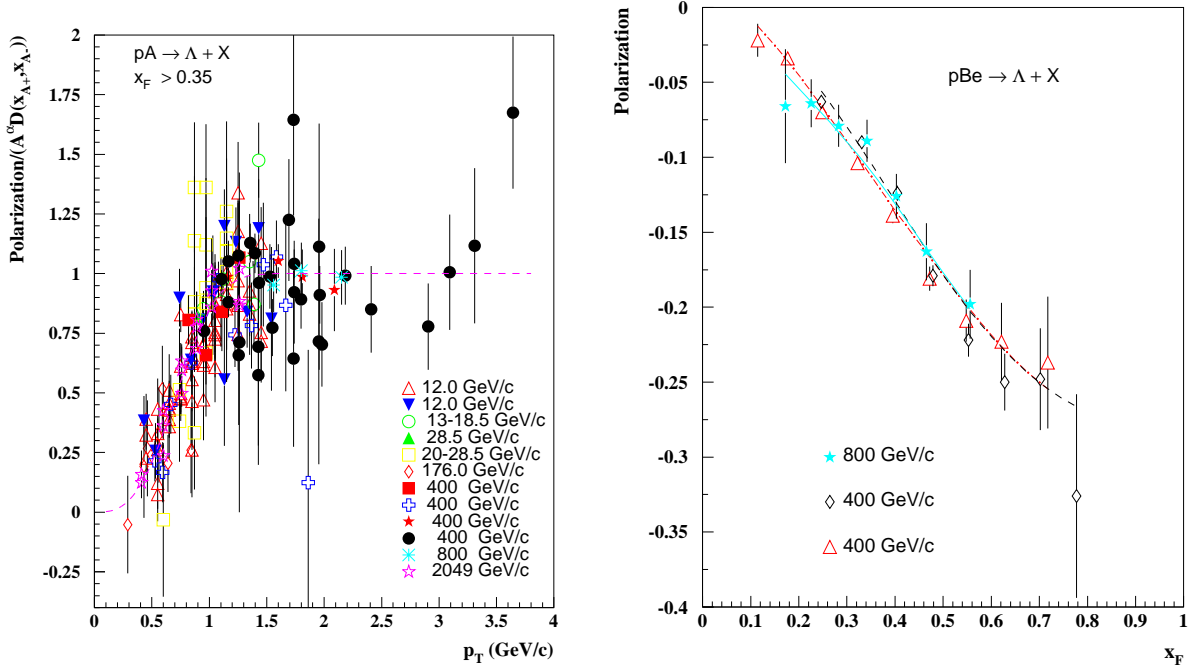
Figure 2.6: *Left*: Ratio of P_Λ and $A^\alpha D(x_{A+}, x_{A-})$ showing independence from beam energy ($x_F \geq 0.35$) and target type. The data confirm the scaling behavior and factorization of p_T and x_F dependencies assumed in Eq. (2.9). *Right*: The x_F dependence of P_Λ from the p+Be data at 400 and 800 GeV/c, with a fitting curve describing the trend. Figures taken from [46].

This phenomenological fit will be presented in Sec. 6, labeled as "world data parametrization", as well as the DeGrand-Miettinen model in comparison with some world data measurements and the results of this thesis.

2.4 Change of transverse polarization as an indication of QGP

System size dependence of transverse polarization is one of the possible signals suggested for the identification of the created quark-gluon plasma (QGP) [2]. In this context, the exploration of hyperon polarization properties at energies of several GeV is highly intriguing. Despite the substantial data on Λ production acquired from SPS [72], GSI [73], AGS [74–76], and RHIC [77–80], there are limited findings on Λ polarization in nucleus-nucleus interactions [21, 47–49].

Other indicators of the phase transition from regular nuclear matter to a quark-gluon plasma may include alteration in the polarization characteristics of secondary particles in nucleus-nucleus collisions compared to nucleon-nucleon collisions. Several polarization observables have been suggested as potential signatures of this phase transition. These include a decrease in the transverse polarization of Λ in central collisions [81, 82], nonzero longitudinal polarization of Λ [44, 83, 84], non-zero J/ψ polarization at low p_T [85], anisotropy in dielectron production from vector mesons decay [86], global hyperon polarization [87] (see next section), and spin alignment of vector mesons in non-central events [88].

Since polarization is predominantly a "kinematic" effect, in a QGP, any memory of the direction or polarization of the quarks is erased. Λ hyperons created from the QGP at mid-

rapidity are expected to exhibit zero transverse polarization, as Λ hyperons are formed by the recombination of uncorrelated quarks or sea quarks, in contrast to those in the fragmentation regions (formed through normal hadronic interactions), which should possess polarization. However, the separation of the central (quark-matter "fireball") and fragmentation regions is not well established. The presence of secondary interactions, which may overlap in rapidity with the primary ones that create the QGP, may obscure the effect.

In the scenario of relativistic nucleus-nucleus collisions, it is expected that Λ particles originating from the region where the critical density for QGP formation has been reached are produced through the coalescence of independent slow-sea u, d, and s quarks. As a result, the plasma generates Λ with zero transverse polarization [82]. In the event of QGP formation, a depolarization effect compared to the proton-induced reaction should be noticeable. A depolarization effect of up to 30–40% is anticipated for central events, and it has been demonstrated that this measurable depolarization effect can be observed at the Λ transverse momenta $p_\mathrm{T} \geq (0.6 - 0.8)$ GeV/c [82].

2.5 Global and local Λ polarization

Another intriguing phenomenon is the so-called global polarization [87, 88]. Systems in non-central heavy-ion collisions possess a large orbital angular momentum, which is reflected in the polarization of secondary particles along the direction of the system's angular momentum.

Consistent with zero results were reported in 2007 at $\sqrt{s_{NN}} = 62.4$ and 200 GeV [89]. In 2017, the STAR Collaboration [90] measured non-zero global polarization of Λ and $\overline{\Lambda}$ hyperons in Au+Au collisions at $\sqrt{s_{NN}} = 7 - 39$ GeV, $e.g.$, $P_\Lambda(\%) = 1.80 \pm 0.6$ (stat.) for $\sqrt{s_{NN}} = 7.7$ GeV. ALICE collaboration measurement in Pb+Pb collisions at $\sqrt{s_{NN}} = 2.76$ and 5.02 TeV [91] averaged polarization $P_\Lambda(\%) = 0.01 \pm 0.06 \pm 0.03$, thus consistent with zero, and HADES [92] measurement $P_\Lambda(\%) = 5.3 \pm 1.0 \pm 1.3$ for Au+Au collisions at $\sqrt{s_{NN}} = 2.42$ GeV confirms the earlier observed trend of global polarization decreasing with increasing collision energy. Prospects also include the studies of the global polarization of other hyperons [93].

In contrast, local polarization refers to the hyperons' spin alignment along the beam direction. It varies with momentum and rapidity, reflecting more complex fluid dynamic effects such as thermal shear and inhomogeneous vorticity within the QGP. The first observation by STAR [94] and subsequent observation by ALICE [95] collaborations challenged initial hydrodynamic predictions and prompted refinements in theoretical models. This observation aligns with theoretical predictions that link polarization to the thermal vorticity and shear-induced spin effects in the QGP (for a comprehensive theoretical review, see [96, 97]).

2.6 Future prospects of hyperon polarization measurements

A comprehensive understanding of spin dynamics is crucial for interpreting the mechanisms of hadron production in high-energy collisions. Future research directions encompass several promising avenues:

(i) Transverse polarization studies of other hyperons and antihyperons, such as Ξ^-, which can be accessed by Λ angular distribution measurements.

(ii) $\Lambda\Lambda$ and $\Lambda\overline{\Lambda}$ spin correlations as sensitive probes of production mechanisms [98].

(iii) Global and local Λ polarization in nucleus-nucleus collisions, particularly as signatures of vorticity in the quark-gluon plasma [97].

(iv) In-jet Λ polarization measurements to probe fragmentation dynamics [99, 100].

(v) Study polarized quark and gluon transverse momentum dependent (TMD) parton distribution functions, fragmentating functions, and higher-twist contributions [68].

Precise measurements of hyperon polarization in nucleus-nucleus collisions at $\sqrt{s_{NN}}$ of several GeV can be conducted using the high luminosity at CBM experiment at FAIR ($\sqrt{s_{NN}} \approx$ $2.3 - 5.3$ GeV) [101], and NICA experiment ($\sqrt{s_{NN}} \approx 4 - 11$ GeV) with MPD/SPD and BM@N setup [102–105]. The SPASCHARM project aims to study the spin structure of hadrons and the spin dependence of the strong interaction between matter and antimatter, including transverse polarization at polarized beam momenta up to 45 GeV/c [57]. The fixed-target setup at LHCb [43, 106, 107] offers the ability to collect data at a center-of-mass energy per nucleon $\sqrt{s_{NN}} \in (29, 115)$ GeV in region $-0.1 < x_F < 0.04$ and $p_T \in (0.15, 6)$ GeV/c, which might also be a source of knowledge about Λ polarization.

Chapter 3

The NA61/SHINE Experiment

NA61/SHINE (**S**PS **H**eavy **I**on and **N**eutrino **E**xperiment) is a fixed target experiment at the CERN Super Proton Synchrotron (SPS) accelerator complex [3]. It was proposed in November 2006. A pilot run was conducted in 2007, and the first physics run took place in 2009.

The NA61/SHINE Collaboration comprises about 150 physicists from almost 30 institutions. Before CERN Long Shutdown 1 (LS1) in 2013, it was the second-largest active non-LHC experiment at CERN. The rich physics program of NA61/SHINE is described in Sec. 3.1. This program is feasible due to the significant acceptance of the NA61/SHINE hadron spectrometer based on Time Projection Chambers, as well as a variety of beams (Sec. 3.2) and different targets. The detector system of NA61/SHINE is described briefly in Sec. 3.3. The hardware and software components of NA61/SHINE were inherited from the NA49 experiment [108]. The experiment is continuously upgraded to achieve its physics goals, including a significant overhaul of the corresponding software and calibration procedures.

3.1 Physics program

NA61/SHINE is a collaborative effort that unites experts from heavy-ion physics, neutrino physics, and cosmic-ray physics. Each field relies on the precise measurement of hadron production, utilizing the SPS accelerator's energy range. While their requirements for beam energies, collision systems, and physical observables vary, they share a common goal of advancing our understanding of fundamental physics.

The heavy-ion program is particularly ambitious, aiming to provide systematic data through the precise measurements of proton-proton, proton-nucleus, and nucleus-nucleus collisions. This scan includes data on $p+p$, Be+Be, Ar+Sc, Xe+La, and Pb+Pb collisions, at beam momenta ranging from $13A$ to $150A$ GeV/c, as shown in Fig. 3.1. These data are crucial for interpreting phenomena in heavy-ion reactions and include a groundbreaking two-dimensional scan in the mass of colliding nuclei and collision energy to investigate the onset of deconfinement [109] and search for the critical point of strongly interacting matter [110].

Meanwhile, the neutrino and cosmic-ray programs are more specialized. The neutrino physics program covers analyses of proton-nucleus collisions to allow the calculation of the beam composition and initial neutrino fluxes for experiments at J-PARC and Fermilab facilities [111–114]. The cosmic-ray program focuses on hadron spectra measurements vital for experiments like KASCADE and observatories such as the Pierre Auger. These experiments focus on cosmic rays with extraordinarily high energies, capable of initiating a series of reactions in the atmosphere
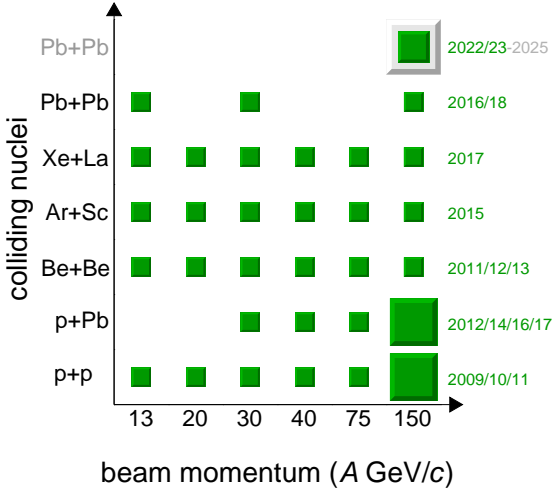
Figure 3.1: Summary of the two-dimensional scan in collision energy and system size, performed by the NA61/SHINE experiment. Green indicates already collected data, while grey marks data that has been taken recently or will be collected in the future. The box size reflects the statistics of the collected data.

known as extensive air showers [115, 116]. To decipher the origins of these cosmic rays, scientists rely on sophisticated models to interpret the data collected by ground-based detector arrays. The accuracy of these models hinges on the precise understanding of hadron production during collisions, particularly involving pions and light nuclei. However, the scarcity of data has led to inconsistencies in current models, prompting NA61/SHINE to prioritize the measurement of these pivotal reactions [117].

3.2 Beams

The CERN accelerator chain, with its components relevant for NA61/SHINE beams, is shown in Fig. 3.2. The accelerator sequences for protons and ions (depicted with Pb ions for ions) differ in injector chains up to the Proton Synchrotron (PS).

Protons are ejected from hydrogen gas and accelerated to 750 keV for injection into LINAC2. Conversely, lead ions are only stripped down to the Pb^{29+} state, with an energy of $2.5A$ keV. Both types of beams are then directed into linear accelerators (LINACs), which increase the energies of the protons to 50 MeV and the lead energies to $4.2A$ MeV.

Upon departing LINAC3, a slender 0.3 μm carbon foil further strips the lead beam, and Pb^{54+} is isolated by the following spectrometer. The proton beam progresses from the LINAC to the PS booster (PSB), accelerating up to 1.4 GeV, while the lead beam advances to the Low Energy Ion Ring (LEIR), boosting its energy to $72A$ MeV. The two accelerator chains converge at the Proton Synchrotron (PS). Upon extraction from the PS, the proton beam carries a momentum of 14 GeV/c, and the lead beam is accelerated to $5.9A$ GeV/c. Exiting the PS, the lead beam is entirely stripped to Pb^{82+} by passing through a 1 mm thick aluminum foil. Subsequently, the beams are channeled into the Super Proton Synchrotron (SPS), where they are accelerated to
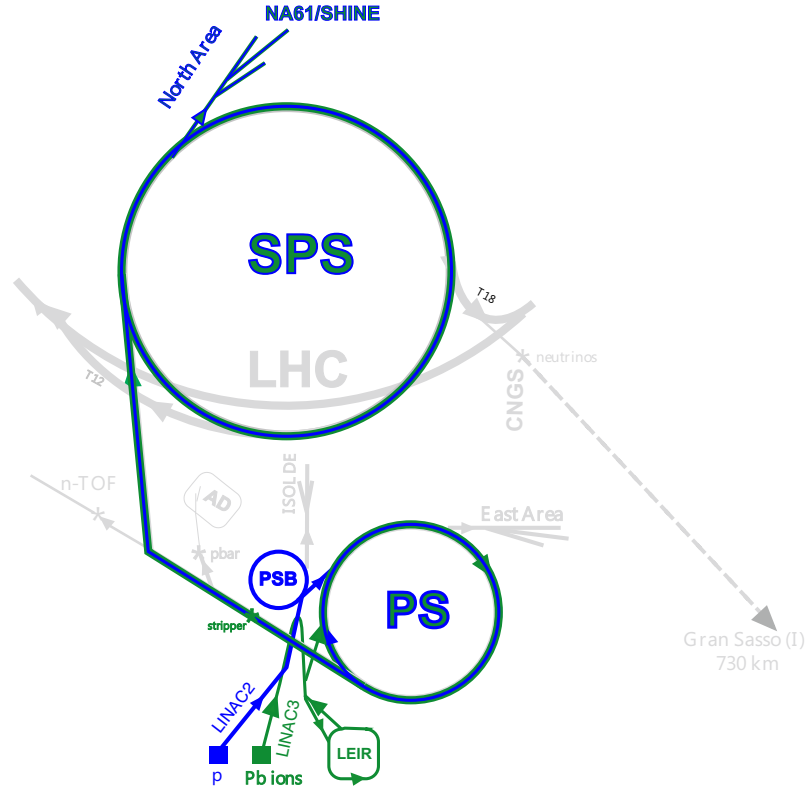
Figure 3.2: Schematic layout of the CERN accelerator complex relevant for the NA61/SHINE ion and proton beam operation. (Top view, not to scale) [3].

400 GeV/c for protons and between 13A GeV/c and 150A GeV/c for ions. The beams are then dispatched to the North Area from the SPS. Typically, the duration of the spill (extraction) is 10 seconds, delivering approximately 10^{13} protons or 10^8 lead ions. This extraction occurs once during the SPS's supercycle, lasting approximately 30 to 60 seconds, serving multiple users (experiments).

3.2.1   H2 beamline and secondary proton beam

The extracted beam from the SPS is directed toward a primary target, T2, where secondary particles are produced. The T2 target station hosts several beryllium (Be) plates of different lengths. From these, the target plate is chosen that best optimizes the yield of the requested secondary particle momentum and type. Beams for NA61/SHINE are usually produced using a target length of 100 or 180 mm. The secondary proton beams utilized by NA61/SHINE (ranging from 13 to 350 GeV/c) are derived from a primary proton beam at 400 GeV/c via the H2 beamline. Since 2015, the primary ^{40}Ar and ^{131}Xe ion beams in the momentum range from 13A GeV/c to 150A GeV/c have been utilized by NA61/SHINE. Two large spectrometers carry out momentum selection within the beam in the vertical plane. These spectrometers select particles based on their rigidity (momentum-to-charge ratio).

Additionally, the beamline features devices that provide data on beam position, profile, and

intensity at various points, as well as particle identification detectors. The quality of the beam as delivered to the experiment is contingent upon both the physics of beam production (initial distributions) and its transport along the beamline (such as the precision of electrical current settings in magnets). This thesis focuses on the proton beams used between 2009 and 2011, which were among the various beams employed throughout the experiment. In proximity to the target, the beam width and angular distribution width are approximately 2.5 mm and 0.9 mrad, respectively, for a beam momentum of 158 GeV/c.

3.3 Detector components

The detector system of NA61/SHINE used from 2009 to 2011 is illustrated in Fig. 3.3 and briefly described below (for a detailed description, see Ref. [3]). The figure also shows the coordinate system utilized in the experiment and, consequently, throughout this thesis. The origin of the coordinate system is located in the center of the second vertex magnet, which encompasses the VTPC-2, as shown in the picture. The z-axis points downstream (relative to the beam particle flux) along the nominal beam direction. The horizontal x-axis runs towards the Jura mountains (left if one looks downstream), while the vertical y-axis points upwards.

3.3.1 Beam detectors and the trigger

When dealing with proton and hadron beams, the beam's momentum reaching the experiment is precisely defined. However, certain aspects related to these beams are not accurately determined by the beamline and require event-by-event measurements. One critical aspect is the trajectory of the projectile. The trajectory of the projectile is assumed to be linear and is determined using three multiwire proportional chambers known as Beam Position Detectors (BPD-1, BPD-2, and BPD-3), as depicted in Fig. 3.3. These detectors serve three essential purposes:

(i) Transverse position constraint: the collision vertex's transverse position cannot be assumed constant due to the secondary beam's width at the target. Using only TPC (Time Projection Chamber) tracks extrapolated to the target is insufficient due to the low track multiplicities associated with hadron beams.

(ii) Angle determination: the angle at which the projectile strikes the target defines the collision's longitudinal and transverse directions.

(iii) Online beam monitoring: the detectors also monitor beamline stability during data acquisition.

Additionally, the beamline does not inherently specify the type of projectile. Two Cherenkov detectors are employed to identify hadrons delivered to the experiment. The first detector, CEDAR (shown in Fig. 3.3), operates as a differential Cherenkov counter. It contains gaseous nitrogen for beam momenta below 60 GeV/c and helium for higher momenta. CEDAR is

20
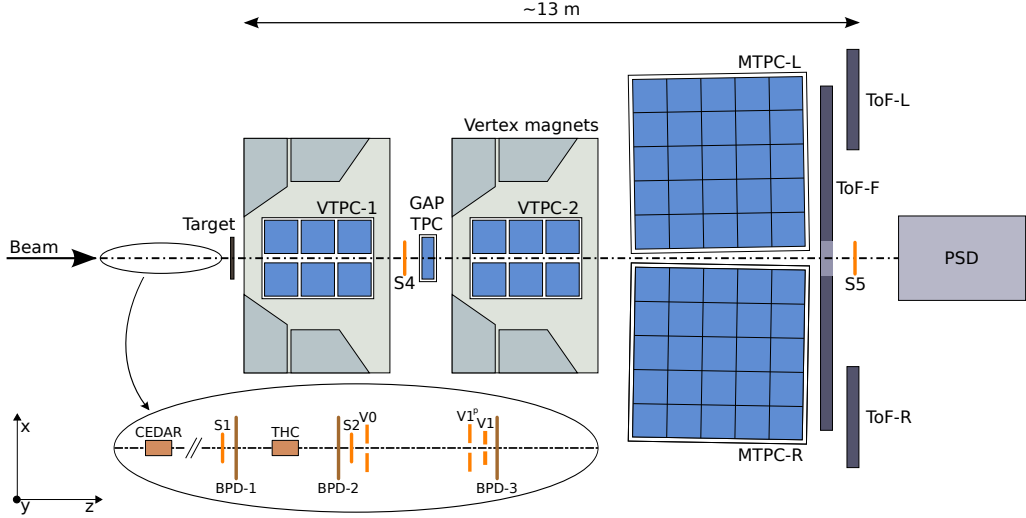
Figure 3.3: The schematic layout of the NA61/SHINE detector system is depicted as a horizontal cut in the beam plane (top view, not to scale). Additionally, it illustrates the coordinate system employed in the experiment and the configuration of beam detectors utilized with secondary proton beams from 2009 to 2011.

sensitive to a narrow range of opening angles of Cherenkov light cones. The Cherenkov angle is mathematically expressed as $\cos\theta = 1/n\beta$, where n represents the refractive index (dependent on gas pressure), and β is the velocity of the beam particle divided by the speed of light in a vacuum.

The NA61/SHINE experiment employs a second Cherenkov detector, THC (Threshold Cherenkov Detector). The THC is filled with either carbon dioxide, nitrogen, or helium, depending on the beam energy. The detector's pressure is carefully adjusted to make it sensitive to particles with masses lower than the desired mass. These particles must also travel at velocities high enough to produce Cherenkov radiation. By doing so, THC effectively "vetoes" undesired particles. Overall, the combination of THC and the first Cherenkov detector (CEDAR) ensures a proton beam purity level of 99%.

The experiment utilizes two types of triggers crucial for proton-proton interactions (see Table 3.2). The first one, the T1 trigger, is used to select beam protons and is formed by a coincidence of two plastic scintillation counters (S1 and S2) with CEDAR. Additionally, it operates in anti-coincidence with THC and veto scintillation counters V0, V1, and $V1^p$ (see Ref. [3] for details). The positions and geometrical properties of these counters are shown in Table 3.1. The veto counters have holes through which the beam passes. Their primary purpose is to identify and exclude events in which the beam particle deviates significantly from the nominal beam axis. Such deviations may occur due to interactions with beamline equipment or when the particle hits the target from the side. The S1 counter also serves as a start detector for TPC drift time measurement and time-of-flight measurements. The second, the T2 trigger, is based on anti-coincidence of the beam triggers with a small scintillator S4 placed downstream of the target (see Fig. 3.3). An event is classified as an inelastic interaction if a beam particle is detected upstream from the target but does not appear downstream (*i.e.*, it misses S4). However, there

Detector	Dimensions $x \times y \times z$ (mm) or diameter $\times z$ (mm)	Hole diameter (mm)	Position z (m)
S1	$60 \times 60 \times 5$		-36.42
S2	$\varnothing = 28 \times 2$		-14.42
S3	$\varnothing = 26 \times 5$		-6.58
S4	$\varnothing = 20 \times 5$		-2.11
S5	$\varnothing = 20 \times 5$		9.80
V0	$\varnothing = 80 \times 10$	$\varnothing = 10$	-14.16
V0^p	$300 \times 300 \times 10$	$\varnothing = 20$	$\approx$ -14
V1	$100 \times 100 \times 10$	$\varnothing = 8$	-7.20
V1^p	$300 \times 300 \times 10$	$\varnothing = 20$	-7.23
BPD-1	$48 \times 48 \times 32.6$		-36.20
BPD-2	$48 \times 48 \times 32.6$		-14.90
BPD-3	$48 \times 48 \times 32.6$		-6.93
Typical thin target position			-5.81

Table 3.1: Summary of typical beam detector parameters: dimensions, positions along the beamline (z coordinates). The positions of most of these detectors varied in time by a few centimeters due to dismounting and remounting in subsequent runs.

Trigger	Configuration
T1	$S1 \times S2 \times \overline{V0} \times \overline{V1} \times \overline{CEDAR}$ (proton beam trigger)
T2	$S1 \times S2 \times \overline{V0} \times \overline{V1} \times \overline{CEDAR} \times \overline{S4}$ (proton interaction trigger)

Table 3.2: Trigger configurations used for p+p interactions data taking.

are cases where elastically scattered beam particles also miss S4 and instances where products of inelastic interactions hit S4. In the first scenario, an elastic event is incorrectly counted as inelastic, while in the second scenario, an inelastic event is lost.

3.3.2 Targets

The versatility of the NA61/SHINE facility is highlighted by its ability to employ a variety of targets. The target is placed in an accessible area in front of VTPC-1. The beam detectors are reconfigured for each target to fit the new target's holder and ensure that the downstream veto counters and BPD-3 are appropriately aligned with the target. Data collection has been conducted using an assortment of thin targets, including carbon, lead, lanthanum, scandium, and beryllium, with thicknesses ranging from 0.5% to 4% of the nuclear interaction length (λ_I), as well as a T2K carbon target replica (190% λ_I) and a liquid hydrogen target. The target thickness is typically optimized to reduce the likelihood of secondary interactions within the target itself.

For the specific study of proton-proton interactions, a liquid hydrogen target (LHT) was used, measuring 20.29 cm in length (2.8% of nuclear interaction length) and 3 cm in diameter, with a density of approximately $\rho_{LH} = 0.07$ g/cm^3. Data collection occurred with the target filled (target inserted configuration) and, to a lesser extent, with the liquid removed (target removed configuration), where the container held gaseous hydrogen at about 0.5% of ρ_{LH}. The latter setup

allowed for the calculation of data-driven corrections for interactions with materials adjacent to the liquid hydrogen (see, *e.g.*, Refs. [118–120]).

3.3.3 Time Projection Chambers

NA61/SHINE's primary detection instruments are four large-volume Time Projection Chambers (TPCs) depicted in Fig. 3.3, which were previously part of the NA49 experiment. The TPCs detect charged particles, which they image as three-dimensional trajectories of energy deposition within the gas that fills the chambers. These energy depositions enable the particle identification through the dE/dx technique, discussed in Sec. 4.4. The Vertex TPCs are located inside two superconducting dipole magnets with the magnetic field of 1.5 T in the first and 1.1 T in the second magnet for data taking at beam momentum $150A$ GeV/c and higher, resulting in the total bending power of 9 Tm. It allows one to measure the charge signs and momenta of particles by analyzing the curvature and bending direction of their tracks during reconstruction. The Main TPCs extend the detection volume, enhancing the dE/dx measurements. Additionally, a smaller GAP-TPC is situated on the beamline between the Vertex TPCs to ensure coverage in areas the larger TPCs miss. The principle of TPCs operation is illustrated in Fig. 3.4, and the main parameters are described in Table 3.3.
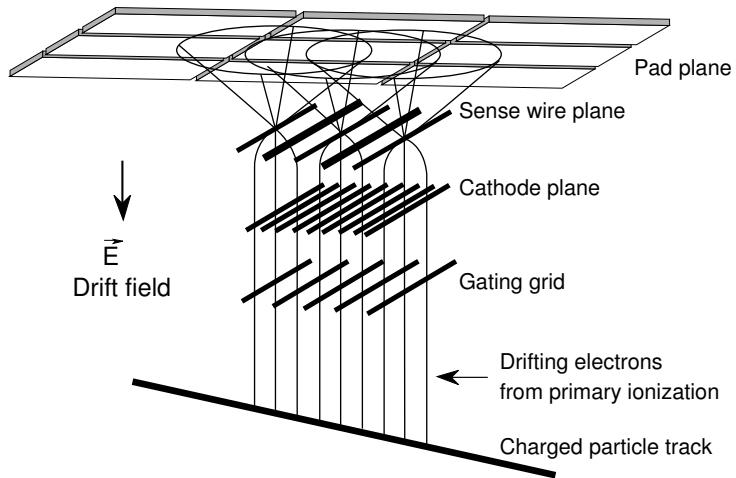
Figure 3.4: Illustration of the principle of operation of the NA61/SHINE TPCs. The figure is taken from Ref. [108].

The most substantial part of each TPC is the gas-filled sensitive volume, which contains an Ar/CO_2 mixture and is encased by a field cage. This setup facilitates primary ionization, where a passing charged particle ionizes the gas atoms. The field cage establishes a uniform vertical electric field that propels the electrons upward (along the y-axis of the NA61/SHINE coordinate system; see Fig. 3.4) and quickly reaches a steady drift velocity due to collisions with the gas.

The Vertex TPCs are positioned within a magnetic field, ideally aligning with the electric field, although the magnet structure introduces some inhomogeneities away from the VTPC

	VTPC-1	VTPC-2	GTPC	MTPC-L/R
Length (cm)	250	250	30	390
Width (cm)	200	200	81.5	390
Height (cm)	98	98	70	180
No. of pads	26886	27648	672	63360
Pad size (L×W) (mm)	$3.5 \times 28(16)$	3.5×28	4.0×28	$3.6 \times 40, 5.5 \times 40$
Drift length (cm)	66.60	66.60	58.97	111.74
Drift velocity (cm/μs)	1.4	1.4	1.3	2.5
Drift field (V/cm)	195	195	173	170
Drift voltage (kV)	13	13	10.2	19
Gas mixture Ar:CO$_2$ ratio	90:10	90:10	90:10	95:5
No. of sectors	2×3	2×3	1	5×5
No. of padrows	72	72	7	90
No. of pads per padrow	192	192	96	192, 128

Table 3.3: Parameters of the VTPCs, MTPCs, and GTPC in NA61/SHINE. The L value in size represents the transverse direction, and the W value indicates the direction along the beam (excluding MTPC rotation). To address the regions with high track density, the pad length is 16 mm only in the two upstream sectors in VTPC-1, and the five sectors nearest to the beam in the MTPCs feature narrower pads, resulting in more pads per padrow.

centers. This results in the drift velocity deviating from the nominal vertical direction, causing electrons from primary ionization not to follow perfectly vertical paths. This phenomenon is known as the $\vec{E} \times \vec{B}$ effect. The drift velocity $\vec{u}$ in the presence of electric and magnetic fields can be described by the following formula [121]:

$$\vec{u} = -\frac{v_d}{E}\frac{1}{1 + \frac{v_d^2 B^2}{E^2}}\left(\vec{E} - \frac{v_d}{E}\vec{E} \times \vec{B} + \frac{v_d^2}{E^2}\left(\vec{E} \cdot \vec{B}\right)\vec{B}\right), \tag{3.1}$$

that might be derived from the Langevin equation of motion of a charged particle in electric and magnetic fields, assuming that the velocity vector $\vec{u}$ remains constant over time, taking into account the friction resulting from interactions with the gas, and v_d is a drift velocity magnitude measured in the absence of the magnetic field.

The drift velocity depends on the magnitude of the electric field, as well as the gas mixture, temperature, and pressure. The gas mixture for MTPCs consists of Ar and CO$_2$ with a ratio of 95:5, which has slightly different proportions than the mixture for VTPCs and GAP-TPC. A higher argon content increases the drift velocity, enabling electrons to traverse the larger heights of MTPCs in a similar time frame as in VTPCs. Both v_d and the electric field $\vec{E}$ are approximately constant within the active volume of a given TPC. The dimensionless value $(v_d \cdot B/E)$ for $B = 1.5$ T (VTPC-1) is approximately 1.08.

When the magnetic field $\vec{B}$ is significantly non-uniform, the drift velocity $\vec{u}$ depends on the location in space. Therefore, $\vec{r}(t)$, which represents the position of primary ionization electrons

drifting in TPCs as a function of time t, is a numerical solution of a differential equation

$$\vec{u}(\vec{r}) = \frac{d\vec{r}}{dt}.$$
(3.2)

In the presence of a strong magnetic field, the path in VTPCs forms a curve on the $x - z$ plane, while in MTPCs, it is a straight line. The drift, controlled by Eq. (3.2), concludes in readout proportional chambers located at the top of TPCs (see Fig. 3.4). Each large TPC houses multiple such chambers, known as sectors. Each sector comprises three wire layers: the gating grid, cathode plane, and sense wires.

When activated, the gating grid generates an electric field that prevents drifting electrons and gas ions from entering the chamber. During the readout phase, it briefly opens to let electrons in and then closes to block slow-moving ions that could disrupt the electric field. The cathode plane divides the drift volume with a uniform electric field from the amplification section. The sense wire plane forms the latter, which includes thin sense wires interspersed with thick grounded wires. Near the sense wires, the electric field is so intense that electrons accelerate enough to ionize the gas. This process repeats, leading to gas amplification, where the electron count increases by a factor of about 10^4. It is important to note that each sector has its own high-voltage supply, resulting in different amplification factors for sectors, which vary over time and are taken into account in dE/dx calibration (see Sec. 4.4).

The amplified electron count collected on the wires is sufficient to induce an electric signal on the pad plane, which the electronics can detect. Each pad plane is divided into rows of pads (padrows) roughly aligned along the x direction (MTPCs are rotated by about $1°$ relative to the nominal beam direction). While padrows are parallel to each other, pads are tilted at varying angles to align with average track trajectories at a given point, optimizing tracking and dE/dx resolution. Each pad is linked to a separate electronics channel, resulting in approximately 180 000 channels in the entire system. A portion of the electronics (motherboards responsible for initial signal processing) was upgraded from NA49, offering ten times faster data acquisition – up to about 70 events per second.

The spatial position of each pad is known. Electrons originating from vertically separated locations in the sensitive volume travel different drift distances and arrive at different times. These times are recorded with a 200 ns sampling along with signal intensity, and allow for determining the location of primary ionization (where the track passed) from the solution of Eq. (3.2). Since the signal from a single track is spread over several pads of a given padrow in several time slices, a cluster is formed from signals on these pads and time slices to determine the primary ionization origin. The centroid of this cluster defines the origin point.

As each cluster corresponds to a different padrow, the maximum number of clusters on the track is determined by the total number of padrows that the track crosses: 72 clusters in each of VTPCs, 7 in GTPC, and 90 in MTPC-L/R. It should be highlighted that clusters are artificial constructs associated with NA61/SHINE reconstruction algorithms. From a macroscopic perspective, actual primary ionization occurs continuously in space along the track.

3.3.4 Other components

The NA61/SHINE setup from 2009 to 2011 included a few additional detection systems that were not previously detailed, as they do not directly affect the results presented in this thesis. Nonetheless, for the sake of completeness, they are briefly mentioned:

(i) Time-of-Flight (ToF) walls enhance particle identification in areas where the $\mathrm{d}E/\mathrm{d}x$ method is less effective due to overlapping Bethe-Bloch curves.

(ii) The Projectile Spectator Detector (PSD), a type of hadron calorimeter, is essential for determining the centrality in collisions involving nuclei.

In addition to the advancements made from the NA49 configuration, the NA61/SHINE setup includes helium-filled beam pipes within the VTPCs' gas chambers. This modification is not related to the detectors but serves to reduce the presence of delta electrons. The reduction of these electrons is crucial for minimizing the variability in track density from one event to another within the TPCs, thereby decreasing the systematic uncertainties associated with measuring fluctuations in nucleus-nucleus collisions [3].

The Detector Control System (DCS) consists of software and hardware that control and monitor the working conditions of all detectors, ensuring the experiment's stable and reliable operation.

Chapter 4

Data Processing

This chapter outlines additional steps required before analysis. The calibration and reconstruction procedures in NA61/SHINE were initially based on the NA49 algorithms. Section 4.1 provides the details on the Monte Carlo simulation of $p+p$ collisions and the detector response used in this work. Section 4.2 describes the reconstruction chain, and Sec. 4.2.2 focuses on V^0 reconstruction. Section 4.3 briefly discusses the main calibration steps. Finally, Sec. 4.4 shows mode details about the energy loss ($\mathrm{d}E/\mathrm{d}x$) measurements and calibration.

4.1   Monte Carlo computer simulations

Particle detectors are not flawless, and there are various reasons why particles can remain undetected or poorly measured. One reason is limited geometrical acceptance, meaning that particles originating from specific kinematic regions might not pass through the detector and remain undetectable. Another factor is the suboptimal detector response, which refers to the detector's ability to accurately identify and measure particles as they traverse it.

It is crucial to properly simulate the detector response to address these inherent biases and ensure an accurate analysis of the reconstructed data. The resulting corrections are crucial for determining the actual properties and yields of the particles produced in the recorded $p+p$ interactions. The Monte Carlo (MC) simulations relevant to this work focused solely on the inelastic interactions of the beam protons within the liquid-hydrogen target and the subsequent reconstruction of events. This approach effectively eliminates the contribution of elastic scattering events, achieved through specific event selection cuts as described in Sec. 5.2.2.

The process of simulating the detector response involved several steps. Initially, inelastic hadronic interaction events were generated. The NA61/SHINE opted for the EPOS-1.99 model [122–124] (further referred to as EPOS) due to its superior agreement with data, and the Fritiof model (FTFPBERT) [125, 126], further referred to as FTFP, included in the GEANT [127–129] package. Both EPOS and FTFP models have zero Λ transverse polarization: $P \equiv P_x \equiv 0$, and, as was discussed in Sec. 2.3.1, for the unpolarized beam and target, $P_y \equiv P_z \equiv 0$.

The resulting particles were then propagated through the detector material, using the GEANT4 software package [127, 128, 130]. This simulation accounted for the influence of the magnetic field and various physics processes, including particle decay. Dedicated NA61/SHINE packages were used to model the detector response, incorporating distortions and inefficiencies that account for various detector effects, including the impact of non-uniform electric and magnetic fields, as well as time offsets in the electronic channels. Both the simulated and experimental data were

stored in identical formats for consistency. However, not all aspects of the detector response were simulated. The simulation of energy loss dE/dx was absent due to its complicated structure, as discussed in Sec. 4.4.

Subsequently, the simulated events underwent reconstruction using the same data reconstruction chain described in Sec. 4.2. The reconstructed tracks obtained from the simulation were matched with their corresponding original simulated tracks by comparing their cluster positions.

4.2 Reconstruction

The reconstruction in NA61/SHINE has been carried out offline using the DSPACK package, an object-oriented, client-server, and data-management system (see Ref. [131]) for the data recorded before Long Shutdown 2. The analyses presented in this thesis utilize the SHINE framework, which is based on the ROOT framework [132] (Release v5.34/39) and includes libraries that describe the NA61/SHINE detector and additional analytical tools. The NA61/SHINE reconstruction chain consists of several steps:

(i) Cluster finding in the TPCs. The *cluster* is a signal located on adjacent pads and time slices identified by analyzing signals from TPC pads across all event time slices. The cluster's 3D position is calculated as the weighted mean of pads (x, z) coordinates and time slices (y), where the weights are the charges deposited in each pad and time slice.

(ii) Reconstruction of local tracks in each TPC separately. Neighboring clusters are connected to local tracks. For MTPC-L and MTPC-R (located outside magnets), tracks are fitted with straight lines. The Kalman Filter algorithm is used for track fitting in VTPC-1 and VTPC-2, where tracks curve in the magnetic field.

(iii) Merging track segments from different TPCs to form global tracks. Local tracks are matched and merged into a global track, which is refitted using clusters from all local tracks. This process enables the determination of track parameters, such as the electric charge sign and momentum (for energy loss, see Sec. 4.4 for details). A minimum of 10 clusters is necessary, with the precision of momentum measurement being influenced by both the track's shape and the magnetic field. Under the full magnetic field used for beam momentum 158 GeV/c, the momentum resolution obtained is about $\sigma(p)/p^2 \approx 10^{-4}$ (GeV/c)$^{-1}$ [108].

(iv) Determining the primary vertex. The interaction vertex (*primary vertex*) position is the point of interaction between the beam particle and the nucleon from the target. The primary vertex position (x and y coordinates) is determined using the incident projectile track detected in the Beam Position Detectors (BPD). At least two signals from BPD-3 and either BPD-1 or BPD-2 are required for a straight-line fit. The z-coordinate of the primary vertex is obtained by backward extrapolating all global reconstructed tracks toward the target using the fourth-order Runge-Kutta method [133]. The intersection point where

most global tracks converge defines the z-coordinate of the primary vertex (see details in Sec. 4.2.1).

(v) Matching the ToF signals hits with the TPC tracks.

After reconstructing the simulated event, the process of matching simulated tracks to reconstructed tracks is carried out. Due to challenges such as hits from different particles merging into a single cluster or two closely spaced simulated tracks being reconstructed as a single track, a dedicated procedure was developed to address the lack of a direct one-to-one correspondence between simulated and reconstructed tracks. The procedure begins by matching simulated GEANT hits to reconstructed clusters. For each cluster, the algorithm identifies the nearest hit within 2 cm for TPCs. A minimum of 10 hits in a track is required to be considered reconstructable. Cluster matching efficiency is defined as the ratio of clusters matched to hits versus the total number of clusters.

In the second step of the matching procedure, the best match between simulated and reconstructed tracks is determined based on the number of shared hit-cluster combinations. The algorithm examines each reconstructed track, identifies all associated clusters, and checks for hits linked to these clusters. It then evaluates all simulated tracks associated with these clusters. The algorithm selects the best candidate from these potential matches based on the highest number of shared hit-cluster points. Given the low track multiplicities in the analyzed events compared to heavy ion collisions, the tracks are spatially well-separated. The physics performance of the TPC system was studied using a GEANT software [127, 128, 130] simulation of the detector, giving 99% reconstruction efficiency in a large region of acceptance [3].

4.2.1 Primary vertex finding and fitting

Proper identification and precise measurement of the primary interaction vertex are crucial for accurate physics analysis. The algorithm for identifying the primary vertex involves extrapolating tracks backward to the target z center. The extrapolated track parameters are collected. A cut is imposed on the extrapolated (x, y) position. This cut is defined by the following relation:

$$\left(\frac{x_i - x_{PV}}{\sigma_{x,i}}\right)^2 + \left(\frac{y_i - y_{PV}}{\sigma_{y,i}}\right)^2 < \sigma_{max}^2 \,, \tag{4.1}$$

Here, (x_i, y_i) represents the track position extrapolated to z of the target center, $\sigma_{x,i}$ and $\sigma_{y,i}$ denote the uncertainties in the extrapolated track position, and (x_{PV}, y_{PV}) refers to the primary vertex seed position, provided by the intersection of the BPD beam track with the target. The $\sigma_{max} = 3$ is a parameter indicating the permissible track deviation from the vertex seed position.

Once compatible tracks are selected, a vertex position is estimated. Three options are currently available for position estimation: a one-dimensional fit in z, the direct assignment of the beam-target intersection, and a three-dimensional fit of the vertex position (x_{PV}, y_{PV}, z_{PV}). The direct vertex assignment is only suitable for thin targets. An application of the fully three-

dimensional least-squares-based fitter is restricted to the data quality assessment. Its resolution is lower than that of the other two fitting methods.

The one-dimensional vertex z-fit is performed by adjusting the vertex z-position. It utilizes the BPD track as a constraint on the x and y vertex positions. An objective function f_{obj} is constructed and minimized by varying z_{PV} is given by:

$$f_{\text{obj}}(z_{\text{PV}}) = \sum_{i \in T} \left[\ln \left(1 + \frac{(x_i(z_{\text{PV}}) - x_{\text{PV}})^2}{2\sigma_{x,i}^2(z_{\text{PV}})} \right) + \ln \left(1 + \frac{(y_i(z_{\text{PV}}) - y_{\text{PV}})^2}{2\sigma_{y,i}^2(z_{\text{PV}})} \right) \right]. \tag{4.2}$$

This sum encompasses all tracks included in the fit that satisfy Eq. (4.1). The natural logarithm of a modified χ^2 contribution term is taken to mitigate the impact of outliers. The conditions of whether the fit is **converged** are discussed in Appendix B.1.

4.2.2 V^0 reconstruction

The neutral particles do not interact electromagnetically with the gas molecules in the TPC, so they do not create ionization trails like charged particles do. If they decay into positively and negatively charged particles, they leave tracks that resemble the letter "V".

V^0 decay vertices are reconstructed based on their decay topology. For each pair of positively and negatively charged tracks, a backward extrapolation is performed using the Runge-Kutta method [133] with a step of 2 cm, and the distance of the closest approach (l_{DCA}) is calculated for each combination of tracks. If l_{DCA} is less than 2.5 cm in the x and y directions, the pair is considered a V^0 candidate, suggesting a possible V^0 decay. The momentum of a V^0 track is determined as the total momentum of the V^0 decay products.

Several cuts are applied to optimize the procedure, minimizing the loss of true V^0-vertices while removing as many false V^0s as possible. To begin with, the secondary vertex should be positioned no further than 78 cm (z > −658 cm) upstream from the center of the NA61 liquid-hydrogen target to reduce background from interactions with the beam instrumentation. Another cut ensures that the V^0 track originates from the primary interaction vertex. The difference between the primary vertex position and the crossing point defined by the intersection of the V^0 track and the plane spanned by vectors parallel to the x and y axes, both originating from the primary interaction vertex, must be below 25 cm in both the x and y directions, see Fig. 4.1. This cut is particularly useful for reducing background due to off-time particles. The only kinematic cut applied is $p_{\text{T}}^{\text{AP}} < 0.5$ GeV/c, where p_{T}^{AP} is Armenteros-Podolanski transverse momentum [134] (see Appendix A.1 for the definition) and defined as the absolute value of one of the daughter particle's momentum component transverse to the original V^0 direction of motion. This cut primarily serves to reduce accidental combinations and electron-positron pairs from the $\gamma \to e^- e^+$ reaction.

For each V^0 candidate passing the cuts, the momentum of both daughter tracks is recalculated along with the position of the secondary vertex. It is accomplished by treating the daughter tracks as a pair originating from the same vertex and fitting the three vertex coordinates and
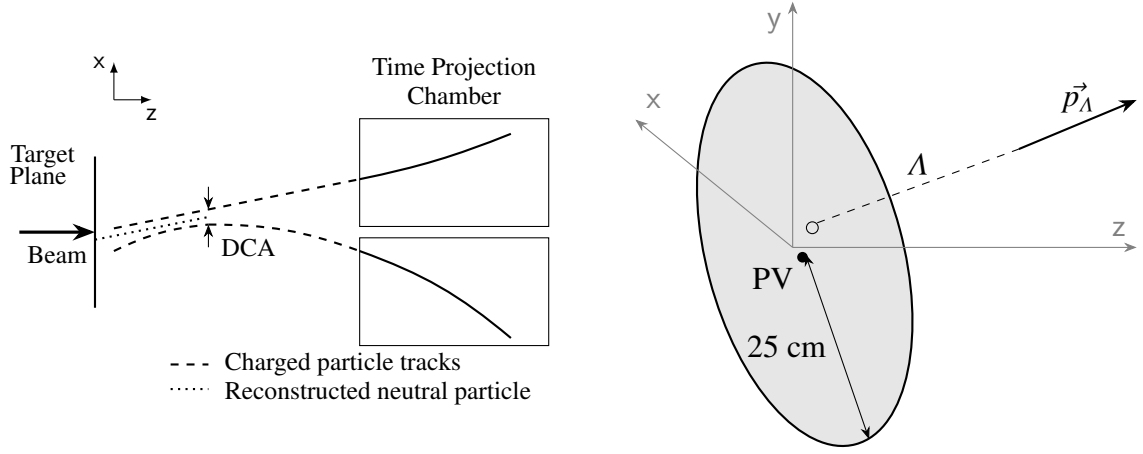
Figure 4.1: *Left:* Schematic definition of distance of the closest approach (DCA). *Right:* The filled circle represents the primary vertex PV, the open circle denotes the point of intersection of the xy plane and Λ momentum, the gray circle of radius 25 cm is spanned in the xy plane at $z = z_{PV}$.

2×3 momentum components together. The fitting is done by applying a Levenberg-Marquard algorithm [135, 136], with the minimization function is

$$\chi^2 = \sum_{\text{all clusters of the two tracks}} \left(\frac{(x - x^{\text{fit}})^2}{\sigma_x^2} + \frac{(y - y^{\text{fit}})^2}{\sigma_y^2} \right), \tag{4.3}$$

where x, y, σ_x, σ_y are cluster positions and their corresponding uncertainties, and $x^{\text{fit}}, y^{\text{fit}}$ are coordinates of the fitted track trajectories at the same z coordinate as the cluster. The convergence criteria selected for the last minimization iteration give χ^2 decrease of less than 0.001 relative to the previous value.

4.3 Calibration

A calibration procedure was conducted to enhance the accuracy of the obtained results. Some calibration coefficients, such as the relative geometrical positions of the detectors, are related to the detector settings and remain constant throughout the data collection period. However, other coefficients change gradually over time; an example of such a coefficient is the electron drift velocity in TPCs. Data calibration involves two steps, which may vary depending on the year of data collection (details provided for the 2009–2011 runs). The first step involves direct measurements, such as detector positions and temperatures. The second step involves extracting corrections to the measured parameters from the data, known as data-based corrections. Notably, the order of individual calibration steps is crucial, and many of these steps require re-reconstruction of preceding data before executing subsequent calibration steps, following a detailed procedure described in Refs. [137, 138].

Among the most important calibration tasks are:

(i) Measurement of gains on segments (chips, pads) of TPC detectors using the radioactive

Krypton spectrum of $^{83}_{46}$Kr.

(ii) Determination of the time constants (T_0, $T_{0\text{det}}$, $T_{0\text{offset}}$) necessary for the time measurement in the detector. For example, the time constant T_0 is the delay between the particle passing through the S1 counter (triggering the time measurement) and the start of the readout from the TPC pad detectors.

(iii) Calibration of drift velocity v_{drift} in VTPC-1, VTPC-2, GTPC, MTPC-L, MTPC-R detectors.

(iv) Measurement and calibration of magnetic fields in VTX-1, VTX-2 magnets and VTPC detectors using $K_S^0 \to \pi^+\pi^-$ invariant mass analysis.

(v) Data-based residual correction of the positions of the three BPD beam detectors relative to geodetically measured positions and the position of the BPD detectors relative to the position of the VTPC-1 chamber (the so-called BPD-TPC alignment).

(vi) Data-based residual correction in TPC detector positions – residual correction of individual cluster (spatial points) positions relative to fitted particle tracks.

(vii) Data-based calibration of energy loss dE/dx measured in TPC detectors (see Sec. 4.4 for details).

(viii) Data-based calibration of geometry and time-of-flight in ToF counters.

4.4 Energy loss (dE/dx) calibration

4.4.1 Energy loss of an ionizing particle

When an ionizing particle traverses through a TPC gas and ionizes atoms, it undergoes a random energy loss described by a skewed Landau (or Landau-Vavilov) distribution.

This distribution, known as a straggling function, becomes more Gaussian-like with increased atom collisions. In the NA61/SHINE energy range $0.1 \lesssim \beta\gamma \lesssim 1000$, the average energy loss per unit length is well described by the Bethe-Bloch function, with the general parametrization as shown in Ref. [12]:

$$-\left\langle \frac{dE}{dx} \right\rangle = Kz^2 \frac{Z}{A} \frac{1}{\beta^2} \left[\frac{1}{2} \log \frac{2m_ec^2\beta^2\gamma^2 W_{\max}}{I^2} - \beta^2 - \frac{\delta(\beta\gamma)}{2} \right], \tag{4.4}$$

where $K = 4\pi N_A r_e^2 m_e c^2 = 0.307075\ \text{MeV} \cdot \text{cm}^2$ with r_e as classical electron radius, z is the electric charge number of incident particle, Z is the atomic mass of atoms in the medium, $W_{\max}$ is the maximum kinetic energy transfer to a free electron in a single collision, I is the mean excitation energy, and $\delta(\beta\gamma)$ is the density effect correction to the ionization energy. The particular parameterization of the Bethe-Bloch function for the NA61/SHINE setup and other details may

be found in Refs. [139–141]. Equation (4.4) relates energy loss to momentum and particle mass, making it challenging to uniquely determine a particle's mass (and therefore species) from energy loss measurements. Figure 4.2 illustrates exemplary Bethe-Bloch functions for particles of different masses and known momenta. In practical cases, most relativistic particles (*e.g.*, cosmic-ray muons) have mean energy loss rates close to the minimum; they are referred to as "minimum-ionizing particles," or MIPs. The energy loss of the MIP is often taken as a reference, and the mean energy loss of other particles is measured in units of this minimum value, which is usually referred to as "1 MIP".
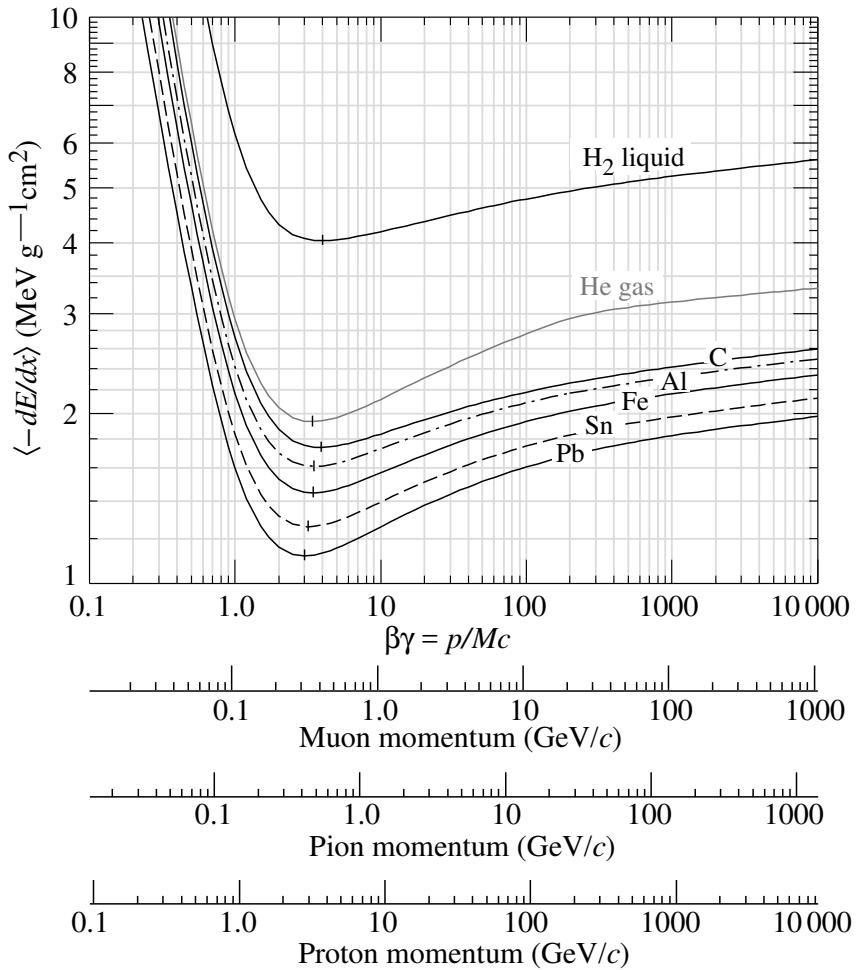
Figure 4.2: Mean energy loss rate in liquid (bubble chamber) hydrogen, gaseous helium, carbon, aluminum, iron, tin, and lead. Radiative effects relevant to muons and pions are not included. The figure is taken from Ref. [12].

4.4.2 Track dE/dx value

Corrected cluster charges lead to the calculation of track dE/dx, a truncated mean of cluster charges on a track. The energy loss probability distribution follows the Landau-Vavilov distribution [12], characterized by strong asymmetry and an extended high-energy tail. Since this distribution lacks a defined mean and variance, the truncated mean approach is employed using

the lowest 50% of ionization energy values. This truncation effectively removes the long tail and narrows the dE/dx distribution, thereby enhancing particle identification capability. However, the truncated mean is systematically lower and dependent on the number of clusters (N) in the truncation.

The correction for the *bias* involves dividing the uncorrected truncated mean by a rational function of N, determined through a fitting process. Despite this correction, the variance of the truncated mean still depends on N, parametrized as proportional to $1/N$. Fitting dE/dx distributions requires a complex model function, such as that developed by Marco van Leeuwen [142].

The track dE/dx, a truncated mean, differs from energy loss (dE/dx) and does not follow the Bethe-Bloch function precisely, but exhibits a similar pattern. The calibration of the sector constants aims to ensure that the truncated mean follows the Bethe-Bloch distribution. However, the comparison reveals an overshoot of 0.5% to 2%, depending on the reaction [143]. The bias increases with decreasing beam energy and is consistent for different reactions at the same energy.

Chapter 5

Analysis Methodology

This chapter offers technical insights into the analysis procedure. Section 5.2 digs into the event and track selection process. Section 5.3 covers the invariant mass fit and the acceptance utilized in the analysis. Moving on, Sec. 5.4 details the implementation of the Monte Carlo correction method. Section 5.5 describes the validation of the methodology presented in the previous sections through MC correction tests, which involves applying unfolding to the MC samples. Finally, the chapter concludes with discussions on statistical and systematic uncertainties.

5.1 Goal definition and methodology

The goal of the thesis is to obtain values of Λ hyperon transverse polarization in several bins of x_F and p_T. To achieve this goal, it is required to get the spatial distributions of daughter protons in the Λ rest frame. The fit of the function given in Eq. (2.3) to the distributions of $\cos\theta_x$, $\cos\theta_y$, $\cos\theta_z$ of protons provides the value of the polarization components P_x, P_y, P_z. The most important is the P_x component that represents the desired transverse polarization. The steps required to achieve the goal are:

 (i) Dedicated study of the **event and track selection cuts** and their optimization relative to signal-to-background ratio and introduced biases.

 (ii) Calculation of **uncorrected number of** Λ hyperons (yields) at different bins of (x_F, p_T) and daughter proton momentum direction in Λ rest frame $\cos\theta_x$, $\cos\theta_y$, $\cos\theta_z$ by invariant mass distributions fit.

 (iii) Development of a **correction** procedure of the Λ spectra on geometrical acceptance, reconstruction efficiency, and other biases, with the use of Monte Carlo simulations performed for this purpose. Validation of this procedure was done through MC correction tests on simulated datasets with known input polarization.

 (iv) **Applying** the **correction** procedure to the measured Λ spectra.

 (v) Calculation of the **polarization value** by fitting the distributions of Λ hyperons based on daughter proton direction at the Λ rest frame $\cos\theta_x$, $\cos\theta_y$, $\cos\theta_z$ at different bins of (x_F, p_T).

 (vi) Calculation of **statistical and systematic uncertainties**.

The overall analysis procedure consists of the steps presented below.

5.2 Data selection

5.2.1 The experimental data and Monte Carlo

Between 2009 and 2011, NA61/SHINE conducted extensive data collection, recording a total of over 60 million events on $p+p$ interactions at 158 GeV/c. After applying the event and track quality cuts described in Sec. 5.2.2, approximately 30 million events, containing about 1 million Λ candidates, were selected for further analysis. The MC datasets comprise about 290 million events of inelastic $p+p$ interactions generated by the EPOS model (see Sec. 4.1) and about 220 million events generated by the FTFP model.

Although this NA61/SHINE data sample has the largest number of events in the history of the experiment before the Long Shutdown 2, the number of events is still many times lower than several other experiments measuring Λ polarization, like approximately 10^9 events in LHCb measurement [23] and 3.2×10^9 in HADES [22].

5.2.2 Event selection

Event selection criteria are divided into two groups: the upstream cuts (using information measured by counters mounted upstream from the target) and the downstream cuts. The first group, independent of the physics of the investigated collisions, is applied only to the experimental data. The event selection aims to minimize the presence of off-target, off-time, and elastic interactions in the dataset for the analysis. To achieve this, the following event cuts are applied:

(i) To ensure that the recorded events originate from a primary interaction vertex within the liquid hydrogen target, events that fulfill the requirements for the T2 trigger (see Sec. 3.3.1 and Table 3.2) are specifically chosen (referred to as the *T2 cut*).

(ii) Beam proton trajectory verification (*BPD cut*) involves two conditions. First, a measured signal must be present in both planes of BPD-3 (the closest BPD to the target). Second, there should be a signal in at least one of the other two BPDs (BPD-1 and BPD-2). This selection is not applied to MC datasets. Instead, the beam trajectory from the data is used in MC to mimic beam broadening.

(iii) Events where beam particles arrive within the $\pm 1.5 \mu s$ time window around the triggering particle (relative to the interaction time) are rejected to avoid misidentifying off-time particles as collision products or secondary interactions. Such overlaps could distort the measurements by creating indistinguishable reconstructed collisions. The selection is based on the time distribution of beam particles traversing the S1 counter, measured relative to the trigger signal generated by the interaction particle (see Fig. 5.1). This approach has been proven sufficient for suppressing contamination from overlapping events using proton beams. The remaining off-time interactions are recorded in the TPCs. However, they are spatially separated by requiring a minimum 2 cm shift in the y-coordinate of their

reconstructed positions in the target plane relative to the primary interaction. This spatial displacement, combined with the temporal cut (the *WFA cut*), ensures the rejection of residual off-time contributions. This cut is not applied to MC datasets because the beam simulation upstream of the target is not present.
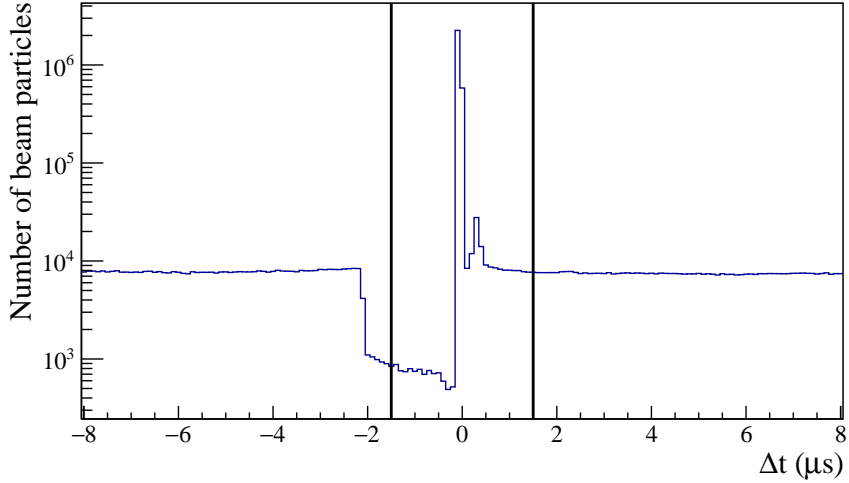
Figure 5.1: Examples of time distribution Δt when particles pass through the S1 counter with respect to the trigger signal. Cut values are shown as thick black lines. Events with entries inside the region $|\Delta t| < 1.5\,\mu s$ (except the peak of the triggering particle at $\Delta t \approx 0$) are removed. See text for details.

(iv) Event must include at least one track reconstructed in the TPCs, originating from the primary $p+p$ interaction vertex. Events with converged primary vertex position fit (see Sec. 4.2.1) are accepted (referred to as the *Fitted Vertex cut*).

(v) Primary vertex position: the validity of the fitted primary interaction vertex position is verified. Only events with the z-coordinate of the primary vertex falling within the target ($z \in [-591.2, -570.9]$ cm) are considered (*Vertex z cut*). The distribution of the z-coordinate of the primary vertices before the cut was applied is illustrated in Fig. 5.2 (*top*), and is compared to the Monte Carlo dataset using the FTFP model. The distribution of (x, y) coordinates of the fitted interaction point after this cut is shown in Fig. 5.2 (*bottom*).

The statistics of recorded and selected events are summarized in Table 5.1. The Monte Carlo datasets are generated with per-year statistics proportions matching those of the recorded collision data from the 2009–2011 period. By matching the MC statistical weights to the data on a year-by-year basis, the simulation dataset accurately averages over the time-dependent fluctuations in detector efficiencies, beam conditions, and calibration constants. This procedure ensures that the corrections derived from the MC, which accounted for detector acceptance and reconstruction biases, are not skewed by the specific conditions of a single, disproportionately simulated year.
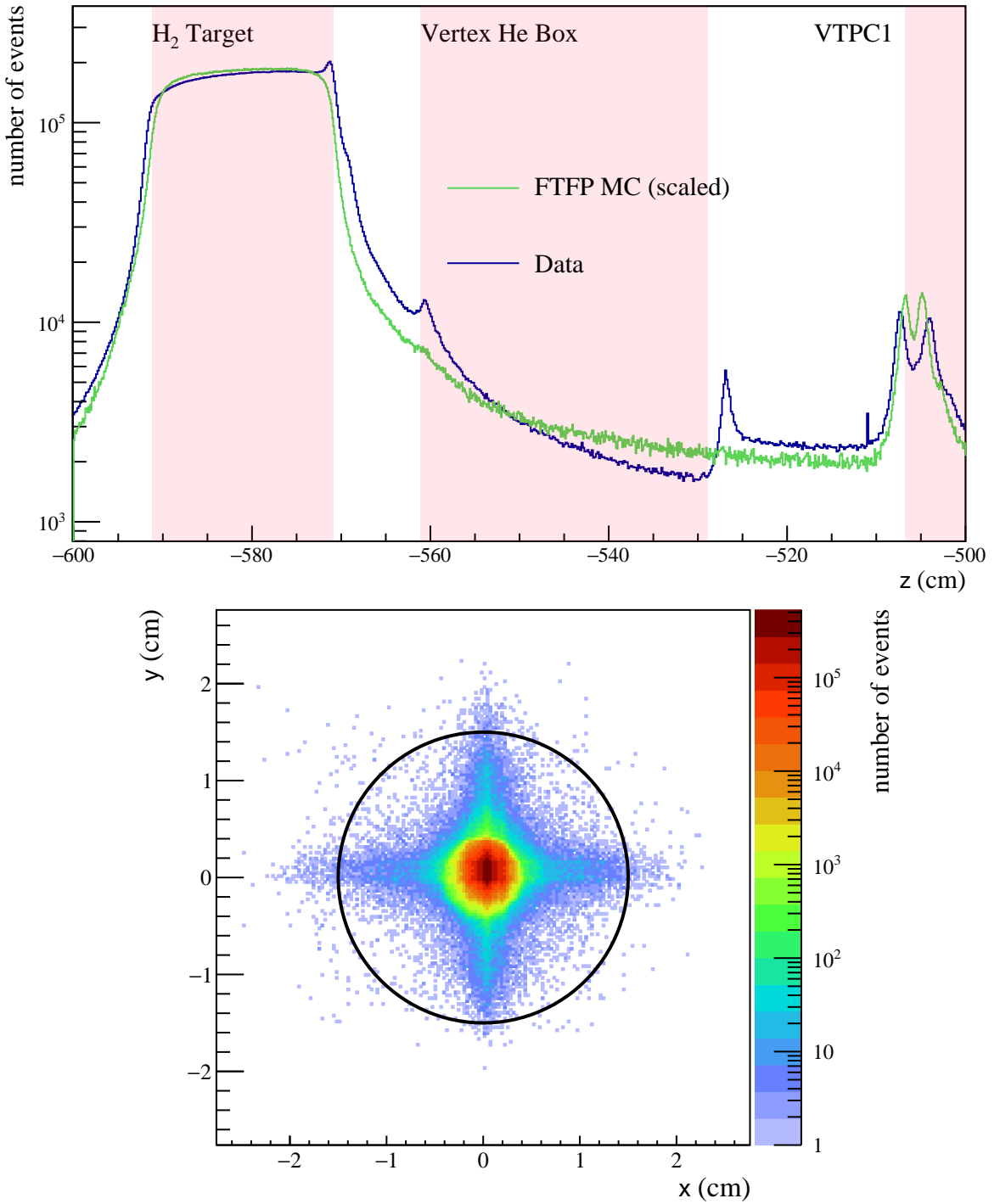
Figure 5.2: Position of the fitted z-coordinate (*top*) and (x, y) (*bottom*) of the interaction point in *p+p* interactions. The bottom panel displays the (x, y) distribution for the events that pass the Vertex z cut. The distribution from the FTFP MC dataset is scaled to the data so that they have equal integral over the z interval *inside* the target. The black circle represents the size (3 cm in diameter) and target position. The *Vertex He Box* was not simulated in MC due to technical reasons. See text for details.

Year	$p+p$ events recorded (mln)	Total selected events (mln)
2009	3.8	1.4
2010	43.1	21.4
2011	13.7	7.4
Total	60.6	30.1

Selection step	Events (mln)		
	Data	EPOS	FTFP
Total	60.6	290	222
T2 cut	52.3	239	182
WFA cut	49.7	–	–
BPD cut	44.7	–	–
Fitted Vertex	38.6	228	175
Vertex z cut	30.1	201	158

Table 5.1: Summary of the recorded high-statistics $p+p$ interactions at 158 GeV/c in NA61/SHINE. *Left*: Statistics per years. *Right*: Statistics for each event selection cut applied. The WFA and BPD cuts are not applied to MC datasets because the beam simulation upstream of the target is absent. See text for details.

Following the application of the described event selection criteria, a final data sample of approximately 30 million events is selected for the subsequent physics analysis. The MC datasets are processed with the same selection chain, resulting in approximately 201 million selected events from the EPOS MC generator and 158 million events from the FTFP simulations. The substantially larger size of the simulated samples, relative to the collision data, is crucial to ensure that the statistical uncertainties from MC datasets in the corrected result are smaller compared to statistical uncertainties from data and other sources of systematic uncertainties.

5.2.3 Track and V^0 selection

The selection of pairs of tracks (further referred to as Λ *candidates*) aims to minimize contamination from secondary interactions and other sources of nonvertex or poor-quality tracks. The applied track cuts are described below.

Particle identification through energy loss (dE/dx) parameter

The selection criterion that has the most significant impact on the Λ analysis is responsible for particle identification (PID) of proton and pion candidates, as depicted in Fig. 5.3. The variable used to differentiate positively charged protons and negatively charged pions from other charged particles is called dE/dx or particle energy loss (as discussed in Sec. 4.4). The strength of the dE/dx cut is determined based on the dE/dx resolution parameter σ(dE/dx), representing the momentum-dependent width of the Gaussian fitted dE/dx distribution (see Ref. [144]).

Tracks are considered candidates for protons or pions if their value dE/dx falls within 3σ of the corresponding Bethe-Bloch value. The significance of this selection is demonstrated in Fig. 5.4, where the absence of the cut results in a poorly defined Λ peak, obscured by a substantial combinatorial background from pion and proton candidates. However, it should be noted that this cut admits particles other than pions and protons, which contribute to the background in an invariant mass spectrum. Therefore, the term "candidates" is used to denote tracks allowed by the cut.
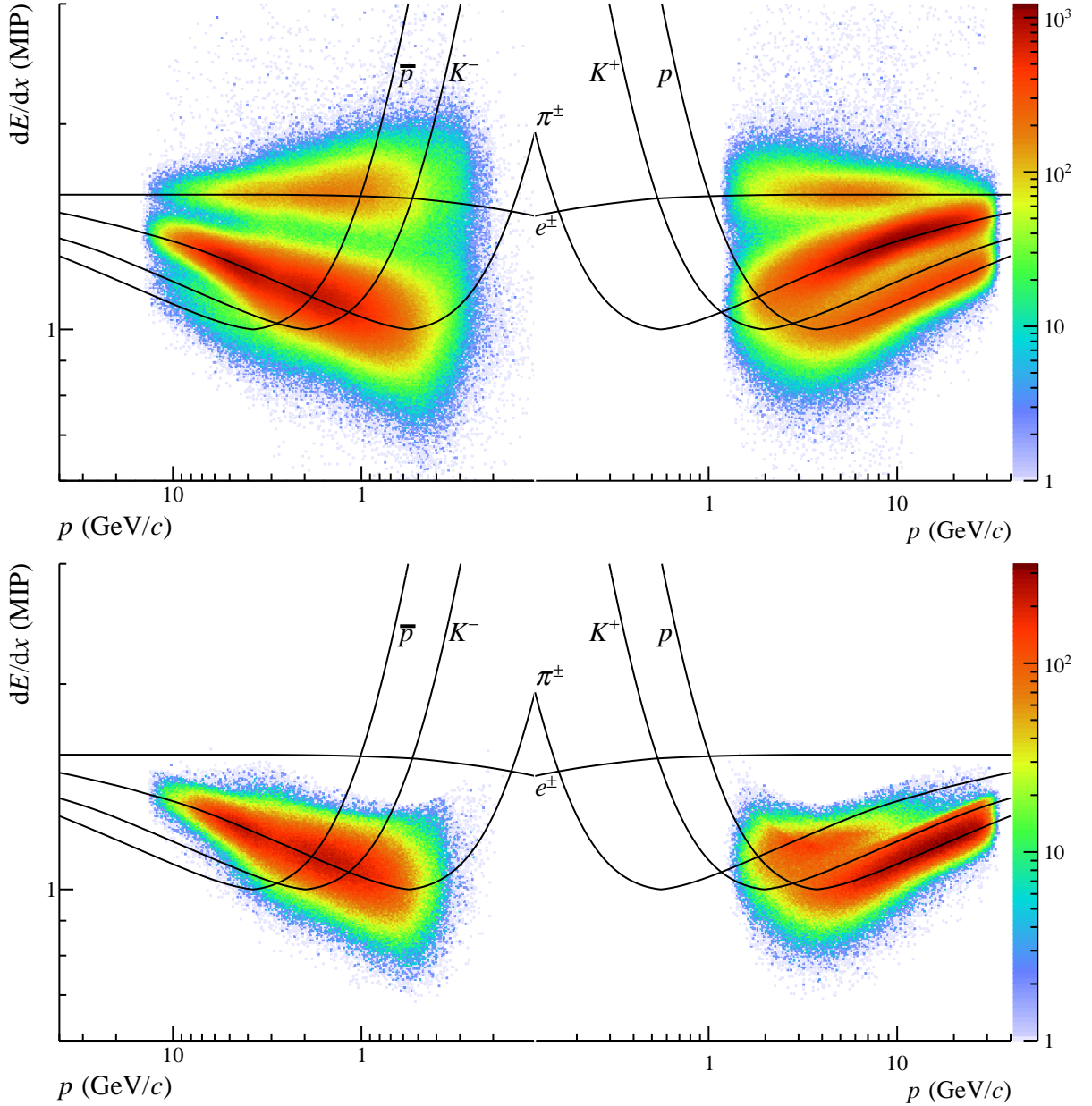
Figure 5.3: The distribution of dE/dx versus total momentum for charged particles in Λ candidates before (*top*) and after (*bottom*) track dE/dx cuts in the kinematic region $x_F \in (-0.4, 0.4)$ and $p_T \in (0, 1.2)$ GeV/c. Negatively charged particles are on the left, and positively charged particles are on the right. The black curves are the expectations for the dependence of the mean energy loss on momentum for $e^\pm$, $\pi^\pm$, $K^\pm$, p, $\bar{p}$ based on the Bethe-Bloch function. See text for details.
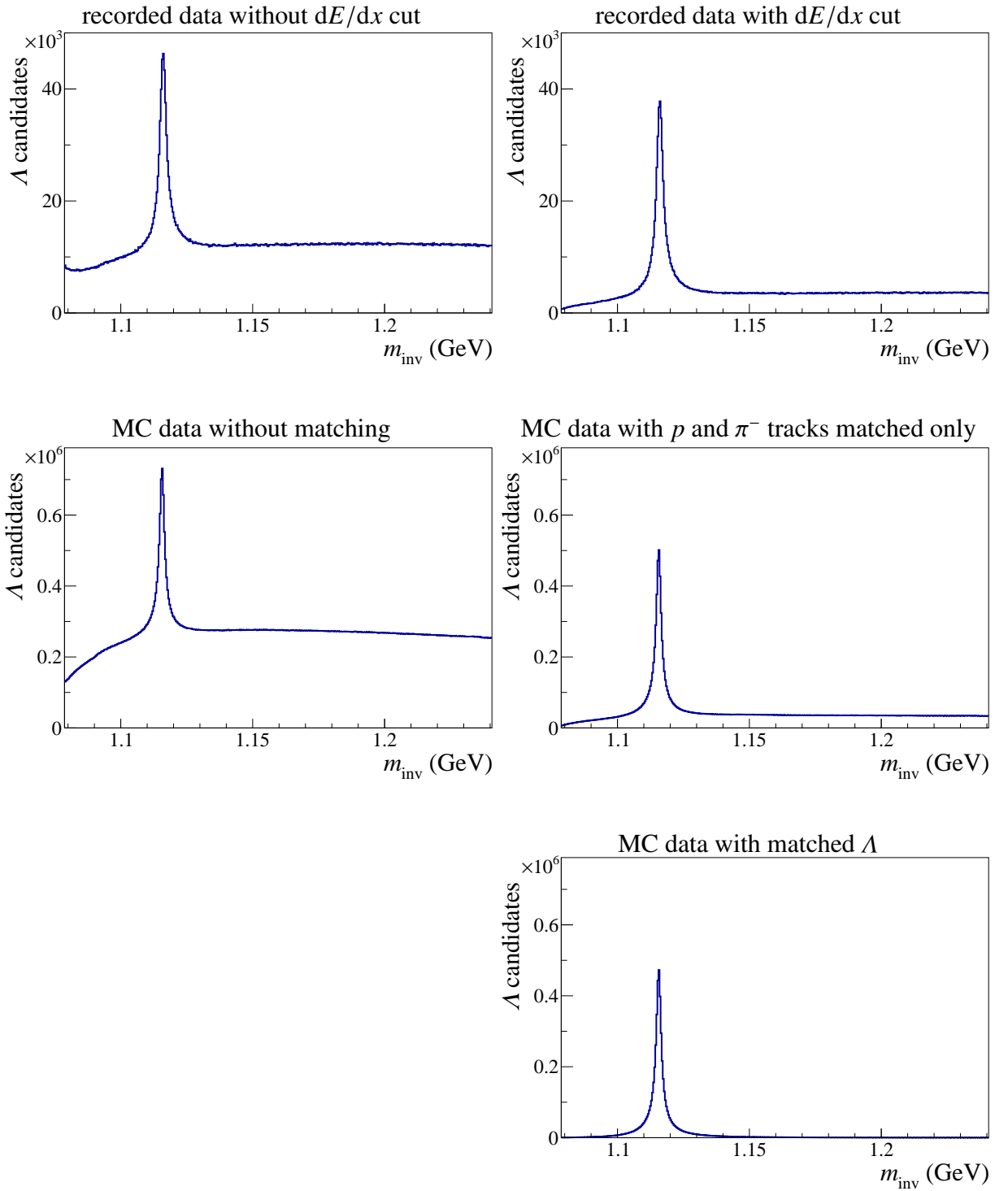
Figure 5.4: Qualitative illustration of the invariant mass distributions $m_{\text{inv}}(p\pi^-)$ after event selection cuts. The data are shown without dE/dx cut (*top left*) and with dE/dx cut (*top right*), while Monte Carlo simulations are shown with different selection criteria: no matching (*middle left*), matching p and π^- tracks (*middle right*), and matched Λ (*bottom right*). The distributions are presented for demonstrative purposes, highlighting the expected peak structure of the Λ hyperon signal and background.

This criterion can only be applied to experimental data because there is no corresponding dE/dx simulation for MC data. Instead, the **matching** of reconstructed tracks to simulated ones is used. The dE/dx cut in data corresponds best (in terms of signal-to-background ratio) to a cut on matched proton and π^- in MC data (*i.e.*, for a simulated track, a corresponding reconstructed track exists and has enough common clusters in TPCs), as shown in Fig. 5.4. Matching Λ, as denoted in this figure, means that both reconstructed tracks are matched to the simulated tracks that emerge from the same vertex of Λ decay produced in a $p+p$ interaction within the target volume.

Number of reconstructed VTPC clusters

For accuracy in particle trajectory measurements, tracks are selected with a minimum of 15 points reconstructed in both VTPC-1 and VTPC-2. Lower values of this cut imply worse momentum resolution. Examples of the distributions of the total number of VTPC clusters in the bins $x_F \in (-0.4, -0.3)$, $p_T \in (0.8, 1.2)$ GeV/c and $x_F \in (-0.1, -0.05)$, $p_T \in (0.8, 1.2)$ GeV/c are shown in Fig. 5.5. To remove background, for EPOS and FTFP MC, matched Λ particles are selected; for data, a dE/dx cut is applied with invariant mass limited to $m_\Lambda \pm 20$ MeV, where $m_\Lambda = 1.115683(6)$ GeV is the Λ hyperon mass [12] (see Sec. 5.3.1 for invariant mass definition). The figure shows consistent descriptions of the distribution in the data and MC. For the kinematic region $x_F < -0.3$, as seen in the figure, the peak of the distribution of the total number of clusters for the pion candidates lies between 10 and 20. Introducing a stronger (stricter) cut, such as the standard requirement of a minimum of 15 clusters, biases this distribution by cutting into its peak. This effect is a significant contributor to the systematic uncertainty and leads to a bias in the final polarization value. Due to this sensitivity, the region $x_F < -0.3$ was excluded from further analysis.

Decay path cut

The Λ hyperon travels on average $c\tau \approx 8$ cm before decaying. However, this distance is significantly larger due to the Lorentz boost along the hyperon's direction of flight. For example, for a Λ particle in the midrapidity region, the rapidity in the laboratory frame is $y = y_{\text{beam}}/2 = 2.9$, the Lorentz factor is $\gamma = \cosh y = 9.2$, and the mean flight path is $\gamma c\tau \approx 73$ cm. The distance between the primary and secondary vertices, defined as the difference between the Λ decay vertex and the primary vertex $\Delta z = z_\Lambda - z_{\text{PV}}$ (see Fig. 5.6), depends on rapidity, with values varying widely – from zero to several meters. Thus, the strategy of Λ candidates selection with Δz cut requires optimization.

The optimization is performed using reconstructed Monte Carlo data, with each (x_F, p_T) bin analyzed independently. Within each bin, a range of Δz values from 5 to 35 cm with a step of 5 cm is evaluated. The signal significance is calculated as $N_{\text{sig}}/\sqrt{N_{\text{sig}} + N_{\text{bkg}}}$, where N_{sig} and N_{bkg} represent the Λ signal and background yields in $(x_F, p_T, \cos\theta_x)$ bins (see Sec. 5.3 for invariant mass distributions fit) to determine the optimal selection value for Δz cut. Distributions of this
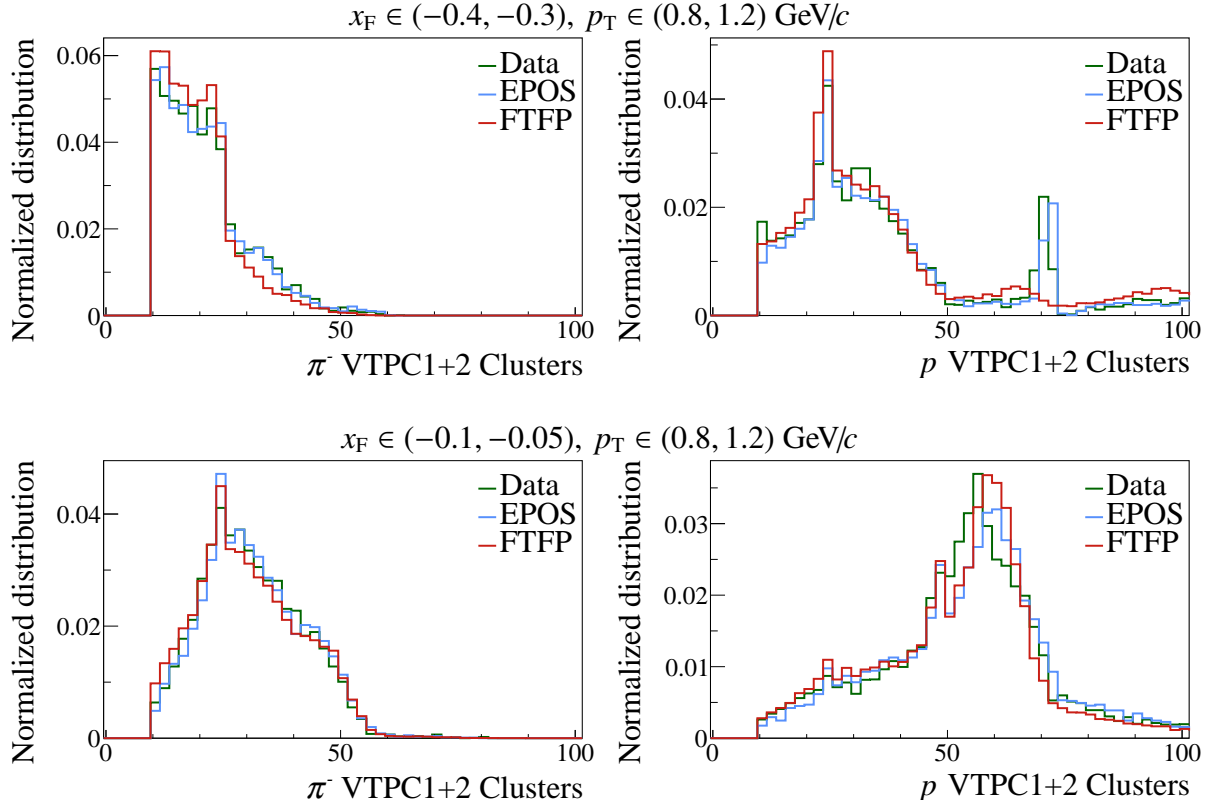
Figure 5.5: Comparison of the distributions of the total number of clusters in VTPCs in negatively (*left*) and positively (*right*) charged tracks of Λ hyperon candidates for data (green lines), EPOS (blue lines), and FTFP (red lines) MC datasets in $x_{\text{F}} \in (-0.4, -0.3)$ (*top*) and $x_{\text{F}} \in (-0.1, -0.05)$ (*bottom*), $p_{\text{T}} \in (0.8, 1.2)$ GeV/c bins. The distributions were obtained before the cut on the number of reconstructed VTPC clusters was applied.
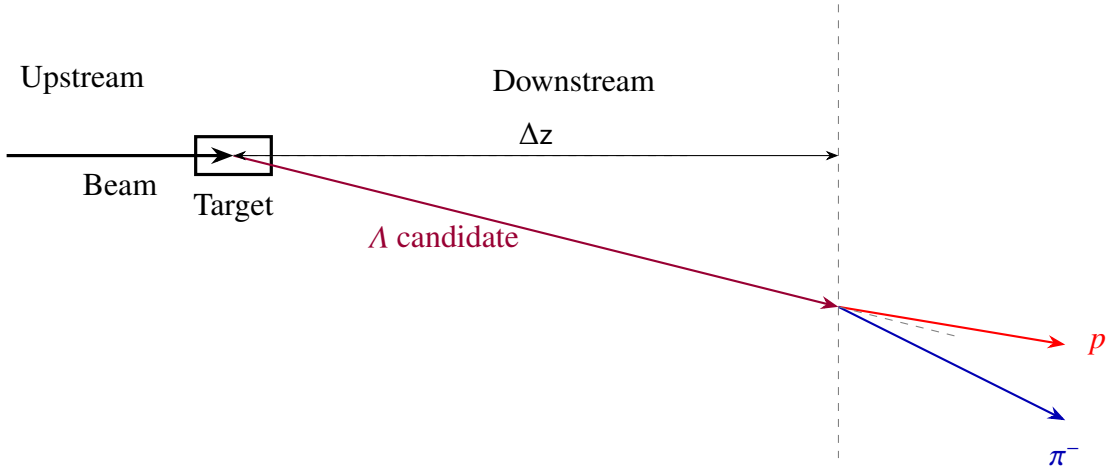
Figure 5.6: Definition of Δz variable used for the Λ candidate selection (see text).

value across $\cos\theta_x$ bins are plotted as a function of the cut values in Fig. 5.7 for two (x_F, p_T) bins. As a result, the value of 10 cm gives the highest significance for all (x_F, p_T) bins considered in the final analysis. The values 15 and 20 cm give the highest significance for the kinematic region $x_F > 0.2$.
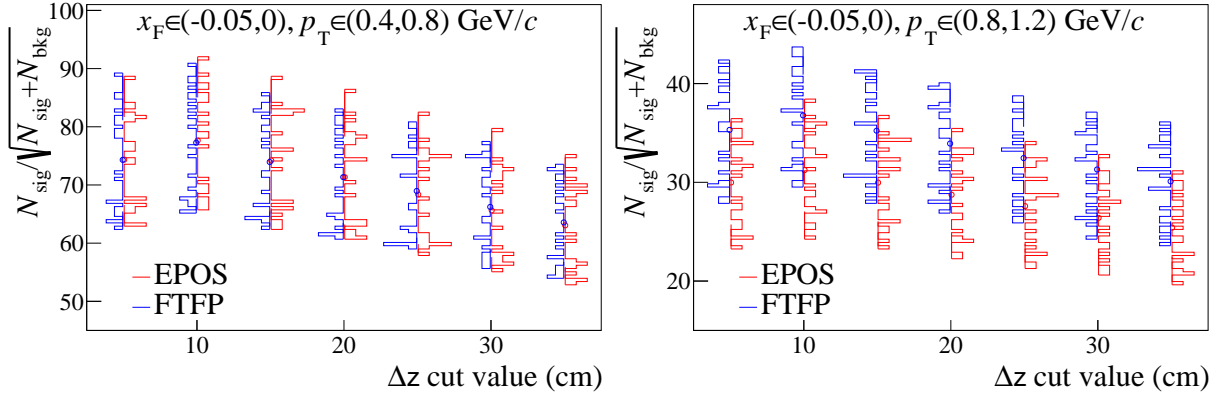
Figure 5.7: The statistical significance $N_{\rm sig}/\sqrt{N_{\rm sig} + N_{\rm bkg}}$ of fitted $m_{\rm inv}$ distribution on 20 bins in $\cos\theta_x$ in $x_F \in (-0.05, 0)$, $p_T \in (0.4, 0.8)$ GeV/c bin (*left*) and $x_F \in (-0.05, 0)$, $p_T \in (0.8, 1.2)$ GeV/c bin (*right*) for EPOS and FTFP models. See text for details.

Impact point

To more effectively reduce the background, it is necessary to select only those Λ candidates that originate from the primary vertex. For this reason, the trajectories of all Λ candidates are extrapolated backward to the plane at the z position of the primary vertex (z_{PV}), and the distances from the primary vertex in x and y directions are calculated. This method yields the calculated values of the impact point along the x (b_x) and y (b_y) axes, as shown in Fig. 5.8. All selected Λ

Figure 5.8: The filled circle is the primary vertex (PV), the open circle is the point of intersection of the xy plane spanned at z_{PV} and Λ momentum, a gray ellipse with semi-axes 2 cm and 1 cm is spanned in the xy plane at z = z_{PV}. The vector from PV to extrapolated trajectory of Λ at z_{PV} (*open point*) has components $(b_x, b_y, 0)$.
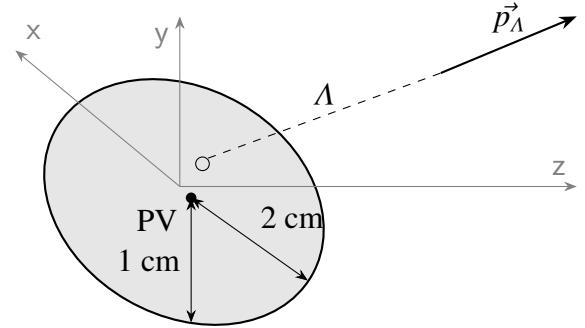
candidates with (b_x, b_y) lie in the ellipse with semi-axes 2 cm in the (bending) x plane and 1 cm in the (drift) y plane, *i.e.*, those that satisfy the condition:

$$(0.5 \cdot b_x)^2 + (b_y)^2 < 1\ {\rm cm}^2\,, \tag{5.1}$$

are classified as primary candidates and undergo further analysis. All tracks that do not meet this condition are discarded. It is assumed that their trajectories do not originate from the primary vertex.

Figure 5.9 shows the 2D distribution of the extrapolated tracks of all Λ candidates in the target plane for data and EPOS MC.
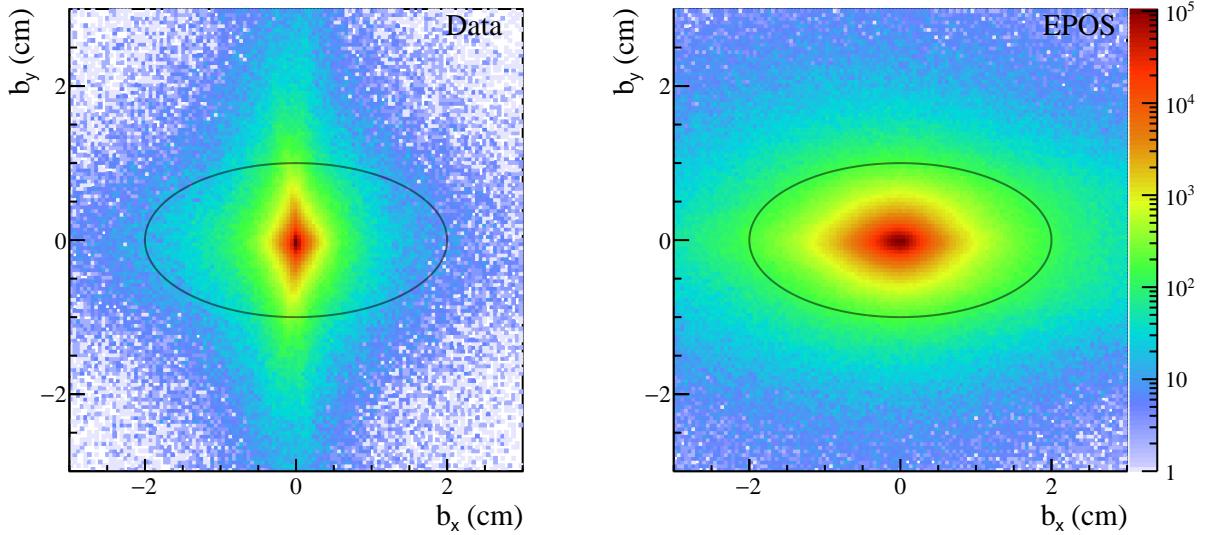
Figure 5.9: Comparison of the impact point (b_x, b_y) distributions in $x_F \in (-0.1, -0.05)$, $p_T \in (0.8, 1.2)$ GeV/c bin for data (*left*) and EPOS MC dataset(*right*). The black ellipse with semi-axes $b_x = 2$ cm and $b_y = 1$ cm represents the cut imposed on Λ candidates.

$\cos\theta_z$ parameter

An additional selection criterion applied to Λ candidates involves the $\cos\theta_z$ value, with θ_z defined in Sec. 2.3 as the angle between the momentum vector of the Λ candidate and the momentum vector of the proton in the center-of-mass frame (Λ rest frame).

As explained in Sec. 2.3, the angular distributions of protons produced in Λ decays in its rest frame $\cos\theta_{y,z}$ should be uniform in $p+p$ interactions of unpolarized protons. However, due to V^0 reconstruction, an excess of V^0 candidates is observed near the boundaries of the distribution ($|\cos\theta_z| \approx 1$), as illustrated in Fig. 5.10. It represents the case where the proton and pion momenta are nearly collinear at the decay vertex. A selection cut is imposed to suppress these misidentified candidates, retaining only those Λs whose decay products satisfy $|\cos\theta_z| \leq 0.95$. Due to the irregular shape of $\cos\theta_z$ distributions even after the cut, the analysis of the P_z polarization component value is dismissed.

The statistics of Λ candidates after each cut are summarized in Table 5.2.

The Armenteros-Podolanski plot is another powerful tool used in particle physics to identify different types of V^0 decays by plotting the transverse momentum of the decay particles against their longitudinal momentum asymmetry (see Appendix A.1). In Fig. 5.11, Armenteros-Podolanski plots for the experimental data before and after the track cuts, as well as EPOS MC
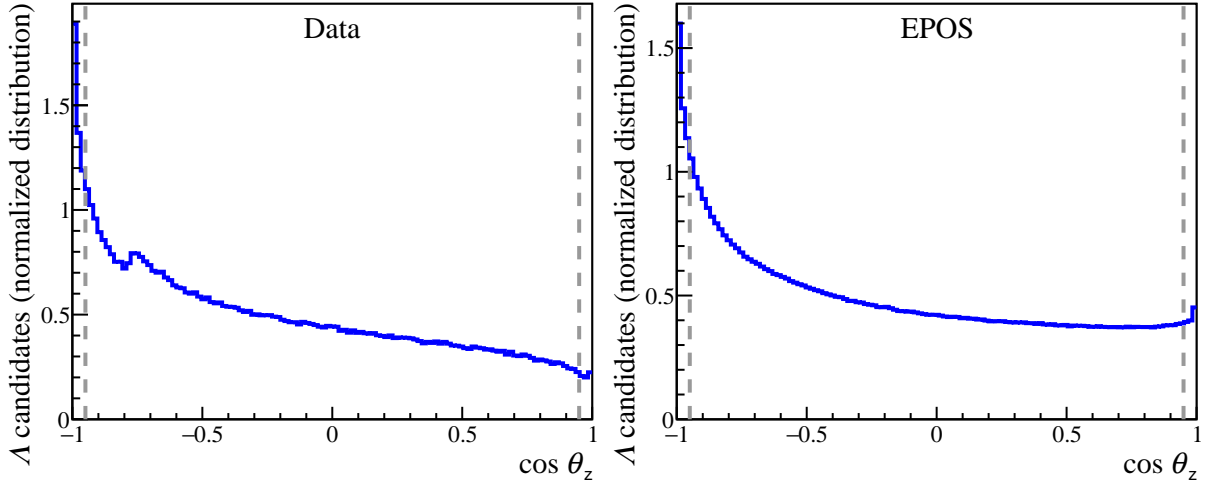
Figure 5.10: Comparison of the normalized $\cos \theta_z$ distributions in $x_F \in (-0.3, 0.2)$, $p_T \in (0.2, 1.2)$ GeV/c in $p+p$ interactions at 158 GeV/c for data (*left*) and EPOS (*right*) MC dataset.

Selection step	Λ candidates (mln)		
	Data	EPOS	FTFP
Λ candidates	443	301	233
VTPC clusters cut	125	284	218
dE/dx cut	2.4	37.5	32.5
Δz cut	1.5	7.5	6
impact point cut	1.2	6.5	5.3
$\cos \theta_z$ cut	1.1	5.9	4.8

Table 5.2: Summary of the track and V^0 selection recorded in data and MC datasets. The first row named "Λ candidates" contains the number of track pairs considered in the range $x_F \in [-0.3, 0.2]$, $p_T \in [0.2, 1.2]$ GeV/c from the V^0 reconstruction algorithm (see Sec. 4.2.2), and invariant mass (see Sec. 5.3.1) $(m_{inv} - m_\Lambda) \in [-35, 125]$ MeV before the aforementioned cuts. See text for details.

data after the track cuts and Λ matching procedure, are shown. Significant non-Λ background reduction is observed.
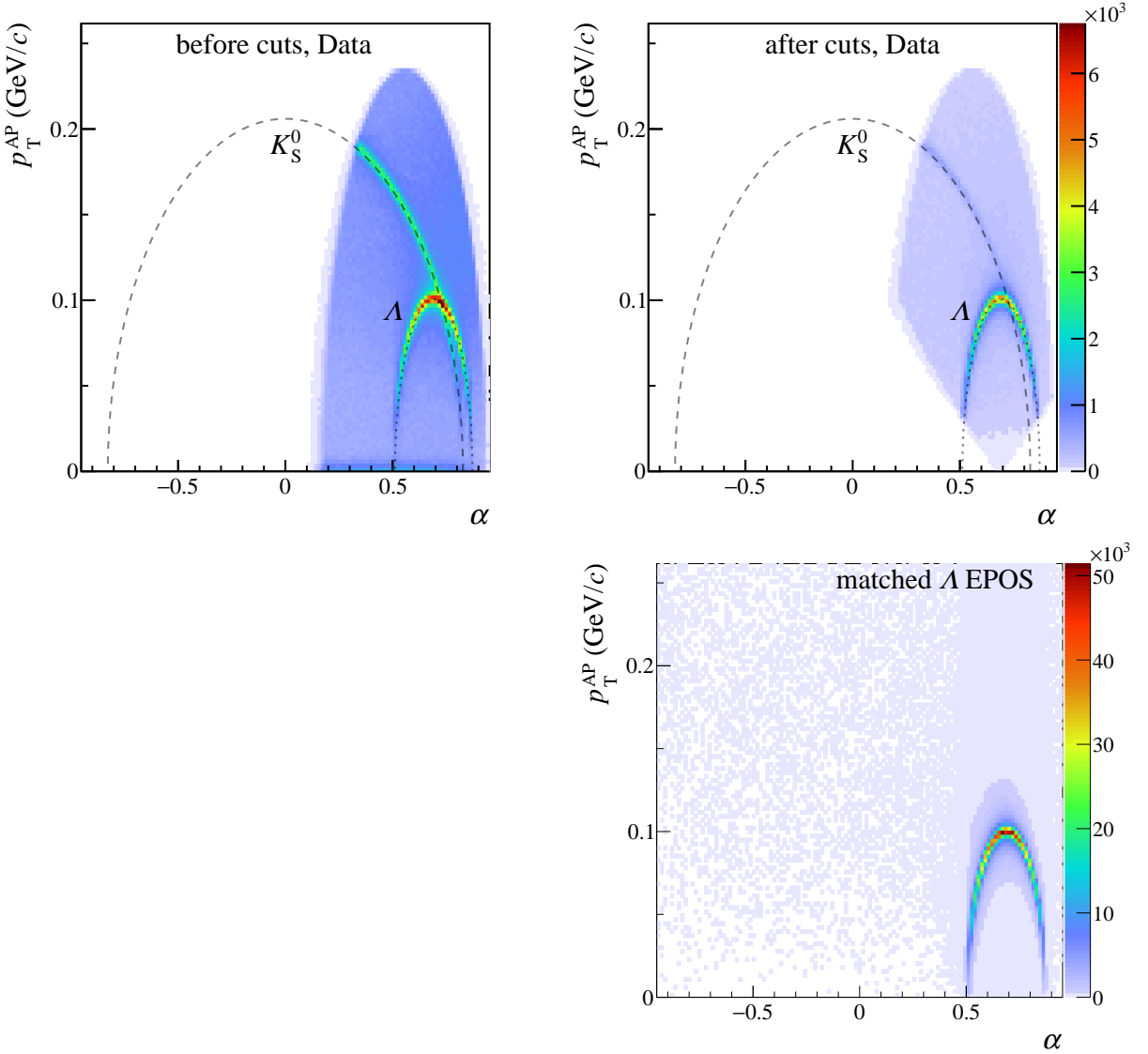
Figure 5.11: The Armenteros-Podolanski plot: the distribution of the Λ candidates in the $\alpha - p_{\mathrm{T}}^{\mathrm{AP}}$ plane in the experimental data before (*top left*) and after (*top right*) track cuts, and in the EPOS MC data after track cuts and the matching procedure (*bottom*). The black curves are the expectations for the K_S^0 and Λ. See Appendix A.1 for the definition.

5.3 Signal extraction

5.3.1 Invariant mass spectrum

The conservation of energy and momentum in decay processes implies that the total four-momentum of the decay products observed is equivalent to the four-momentum of the unobserved

parent particle. For example, in the decay $\Lambda \to p\pi^-$, this can be expressed as:

$$p^\mu_\Lambda = p^\mu_p + p^\mu_\pi.$$ (5.2)

To compute the four-momentum of a particle, an assumption about the particle's mass must be made, which gives:

$$p^\mu_p = (E_p = \sqrt{p^2_p + m^2_p}, \vec{p}_p),$$ (5.3)

$$p^\mu_\pi = (E_\pi = \sqrt{p^2_\pi + m^2_\pi}, \vec{p}_\pi),$$ (5.4)

where PDG values of proton $m_p = 0.9383$ GeV and charged pion $m_\pi = 0.1396$ GeV masses are used [12].

The magnitude of a particle's four-momentum, which is invariant under Lorentz transformations, is its rest mass (or invariant mass). Using the equations above, the rest mass of Λ can be calculated from the measured momenta and assumed masses:

$$\begin{aligned} m_{\text{inv}} = \sqrt{p^\mu_\Lambda p_{\Lambda\mu}} &= \sqrt{(p^\mu_p + p^\mu_\pi)(p_{p\mu} + p_{\pi\mu})} \\ &= \sqrt{m^2_p + m^2_\pi + 2E_p E_\pi - 2\vec{p}_p \cdot \vec{p}_\pi}. \end{aligned}$$ (5.5)

Subsequently, the symbol m_{inv} represents an invariant mass linked with a pair of tracks with opposite charges, computed under the assumption of pion and proton masses. In every event, for each pair, the invariant mass m_{inv} is computed using Eq. (5.5) and is then populated into a histogram (also known as the invariant mass spectrum). According to quantum mechanics, decaying particles do not exhibit a constant m_{inv} like stable particles, but instead display a range of m_{inv} values that follow a specific probability distribution with a resonant shape. The invariant mass method works by counting the number of particle pairs in the spectrum that match the expected signal distribution, rather than the background distribution. The invariant mass method determines the signal yield by fitting the overall spectrum with a composite model. This model consists of a function describing the expected signal shape (the "peak") superimposed on a function that parametrizes the underlying combinatorial background. The number of signal pairs is then the resulting yield from this fit.

Binning

To study the dependence of polarization on (x_F, p_T), hence to obtain the yields of Λ particles in bins of Feynman variable x_F and transverse momentum p_T, invariant mass spectrum is fitted in particular (x_F, p_T) bins[1]: the range $x_F \in (-0.3, 0.2)$ is binned at values $0, \pm 0.05, \pm 0.1, \pm 0.2, 0.3$, and range $p_T \in (0, 1.2)$ GeV/c is binned at values $0.2, 0.4, 0.8, 1.2$ GeV/c. This binning strategy achieves an optimal compromise between two competing demands: statistical requirements,

---

[1]Kinematic region up to $x_F \in (-0.4, 0.4)$ and $p_T \in (0, 1.2)$ GeV/c will appear in intermediate plots for comparison purposes.

which necessitate sufficient statistics per bin, and resolution needs, which require keeping bins small enough to capture kinematic details. The mean Λ multiplicity (*i.e.*, the number of produced Λ particles per inelastic collision) spectra are presented in Fig. 5.12 to visually illustrate the relative number of Λ candidates within the defined kinematic bins. From a statistical perspective, the production rate, or yield, of Λ hyperons decreases significantly with increasing $|x_F|$. It necessitates the analysis of massive datasets to obtain sufficient statistics at high $|x_F|$. Conversely, the magnitude of the transverse polarization signal is expected to be larger at higher values of $|x_F|$ and for transverse momentum p_T values around 1 GeV/c, making these kinematic regions the most desirable for the measurement itself. These competing factors create a trade-off that must be carefully balanced. Furthermore, experiments are constrained by their physical limitations; for instance, the acceptance of the NA61/SHINE detector restricts measurements to a kinematic range of approximately $|x_F| \lesssim 0.4$.
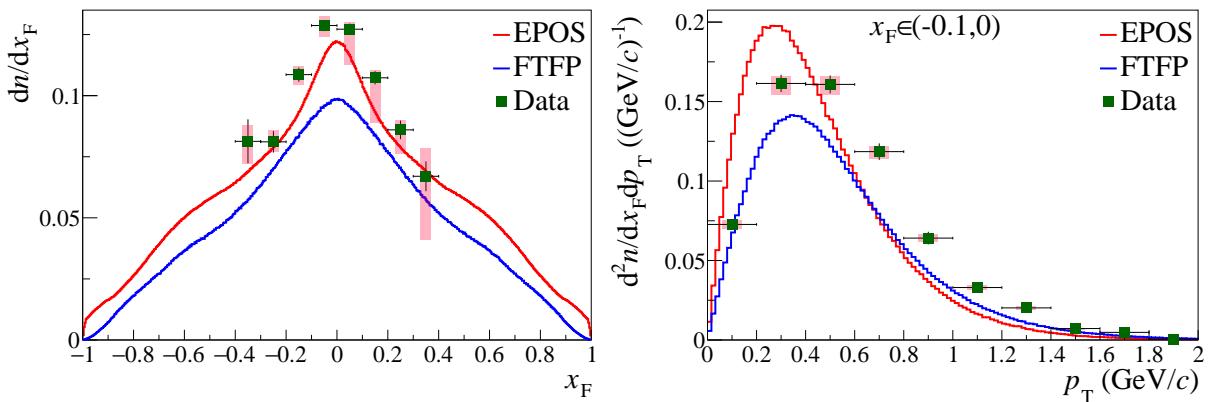
Figure 5.12: Comparison of Λ multiplicity spectra $\mathrm{d}n/\mathrm{d}x_F$ (*left*) and $\mathrm{d}^2n/\mathrm{d}x_F\mathrm{d}p_T$ ((GeV/c)$^{-1}$) around midrapidity (at $x_F \in (-0.1, 0)$, *right*) for $p+p$ collisions at 158 GeV/c measured in 2009 data [145] with MC models. Statistical uncertainties are shown as bars, and systematic ones as shaded bands.

The invariant mass spectra under fit are ranging from 1080.683 MeV to 1240.683 MeV (-35 MeV $< (m_{inv} - m_\Lambda) < 125$ MeV). Values of $\cos \theta_x \in [-1, 1]$ are spread into 20 bins, leading to a bin width of 0.1.

Additional binning in the azimuthal angle in the $(\cos \theta_y, \cos \theta_z)$ plane was implemented to study detector acceptance more differentially. However, no improvement in the final transverse polarization value was observed. At the same time, the additional azimuthal binning only increased the complexity of the analysis and statistical fluctuations.

Signal parametrization

The signal contribution to the invariant mass spectrum consists of two parts: the natural shape of the resonance and the broadening because of detector resolution.

The primary characteristic of resonance is its pole position, denoted as s_{res}, in the complex $\sqrt{s}$ plane, which remains independent of the reaction under investigation. The more conventional

parameters, mass M_{res} and total width Γ_{res}, can be introduced using the pole parameters as follows [12, Ch. 50]:

$$\sqrt{s_{\mathrm{res}}} = M_{\mathrm{res}} - i\Gamma_{\mathrm{res}}/2\,. \tag{5.6}$$

It is important to note that the standard Breit-Wigner parameters, M_{BW}, and Γ_{BW}, usually introduced for particles, often deviate from the pole parameters due to factors such as finite-width effects and the influence of minimum energy thresholds.

As Λ decay is a weak decay with a mean lifetime $\tau = 2.632 \times 10^{-10}$ s and a branching ratio $\mathscr{BR}(\Lambda \to p\pi^-) = 0.639$, it leads to the natural width of the studied $p\pi^-$ decay channel equal to

$$\Gamma = \frac{\hbar}{\tau} \cdot \mathscr{BR} = 1.6 \cdot 10^{-6}\ \mathrm{eV}\,, \tag{5.7}$$

which is 12 orders less than the detector resolution broadening of approximately 3 MeV.

The signal in the analysis is parametrized by the asymmetric q-Gaussian function:

$$S(m) = \mathcal{N}_{\mathrm{S}} \left[1 + (q-1)\frac{(m-m_\Lambda)^2}{\Gamma^2/4} \right]^{-\frac{1}{q-1}}\,, \tag{5.8}$$

where Γ is Γ_{L} if $m < m_\Lambda$ and Γ_{R} otherwise, and the normalization constant $\mathcal{N}_{\mathrm{S}}$ is defined as in Appendix B.2.

The q-Gaussian distribution approaches a Gaussian distribution as $q \to 1$, and it becomes equivalent to a Lorentzian distribution when $q = 2$. The upper limit is $q = 3$, when the distribution takes the form $f(x) = 1/\sqrt{1+x^2}$ and normalization constant $\mathcal{N}$ for $x \in (-\infty, \infty)$ becomes infinite. The q parameter is not adjusted to fit the data but rather is determined using Monte Carlo simulations (see Sec. 5.3.2).

Background description

As the shape of the background depends strongly on the region of the phase space, and the data are analyzed over a wide range of x_{F} and p_{T}, the background must be described by a function that is flexible enough to fit the changing shape. The background in the analysis is parametrized by the function

$$B(m) = \mathcal{N}_{\mathrm{B}} \max(1 + p_1 T_1(m) + p_2 T_2(m), 0)\,, \tag{5.9}$$

where $T_1(m) = m$, $T_2(m) = 2m^2 - 1$ are Chebyshev polynomials of the first kind, p_1, p_2 are real coefficients and $\mathcal{N}_{\mathrm{B}}$ is the normalization constant. The Chebyshev polynomials, compared to other sets of polynomials, have the advantage of yielding the lowest correlation between coefficients p_1 and p_2 during the fit.

The fitting function

Having modeled both the signal and the background, the probability density function used to fit the invariant mass spectrum can be defined as:

$$\text{PDF}(m) = \frac{N_{\text{sig}}S(m) + N_{\text{bkg}}B(m)}{N_{\text{sig}} + N_{\text{bkg}}}, \tag{5.10}$$

where N_{sig} and N_{bkg} are the number of signal and background pairs in the spectrum, respectively.

5.3.2 Fitting strategy

All fits are unbinned extended log-likelihood fits (see, *e.g.*, Ref. [146]). The implementation utilizes the RooFit library [147], which is shipped with the ROOT framework [132]. The fit is the minimization of the likelihood function defined as

$$\mathcal{L} = \text{Poisson}\left(N|N_{\text{sig}} + N_{\text{bkg}}\right) \cdot \prod_{m_{\text{inv}}} \frac{N_{\text{sig}}S(m_{\text{inv}}) + N_{\text{bkg}}B(m_{\text{inv}})}{N_{\text{sig}} + N_{\text{bkg}}}, \tag{5.11}$$

where $\text{Poisson}(N|\lambda)$ is the Poisson distribution probability function with mean λ, and the product is conducted over N Λ candidates in a single $(x_{\text{F}}, p_{\text{T}}, \cos\theta_{\text{x}})$ bin. As a result, fitting involves up to 7 parameters: $\Gamma_{\text{L}}, \Gamma_{\text{R}}, q, p_1, p_2, N_{\text{sig}}, N_{\text{bkg}}$.

All minimization procedures are executed using the MINUIT2 library [148], which is also bundled with ROOT. The MINIMIZE algorithm [149] from MINUIT2 has demonstrated satisfactory performance and stability. Within MINUIT2, two algorithms are available for estimating statistical uncertainties of fitted parameters: HESSE and MINOS [149, 150]. HESSE yields symmetric parabolic errors, while MINOS provides asymmetric uncertainties. For ease of interpretation, the decision is made to utilize the uncertainties provided by the HESSE algorithm. The criteria of **converged** fit are discussed in Appendix B.1.

In the first step, for the MC samples, the distributions of **matched** Λ are fitted without background ($N_{\text{bkg}} \equiv 0$). The obtained values of $q, \Gamma_{\text{L}}, \Gamma_{\text{R}}$ are used in the next step as initial parameters. In the second step, an extended fit is performed with a fixed q value. For data, the q value is taken as the weighted average of the values from the EPOS and FTFP fits.

The fitted m_{inv} distribution example is shown in Fig. 5.13.

5.3.3 Quality of fits

Values of the fitted q parameter for two selected $(x_{\text{F}}, p_{\text{T}})$ bins are presented in Fig. 5.14. For the midrapidity bin (*left*), the typical value of q is approximately 2. For a more forward bin (*right*), the value of q is between 2 and 3. The observed variation in the fitted q values across different $\cos\theta_{\text{x}}$ bins supports the use of the q-Gaussian function, as opposed to a Lorentzian distribution with a fixed q value of 2.

The fitted $\Gamma_{\text{L,R}}$ values are displayed in Fig. 5.15. The width typically lies in the range from
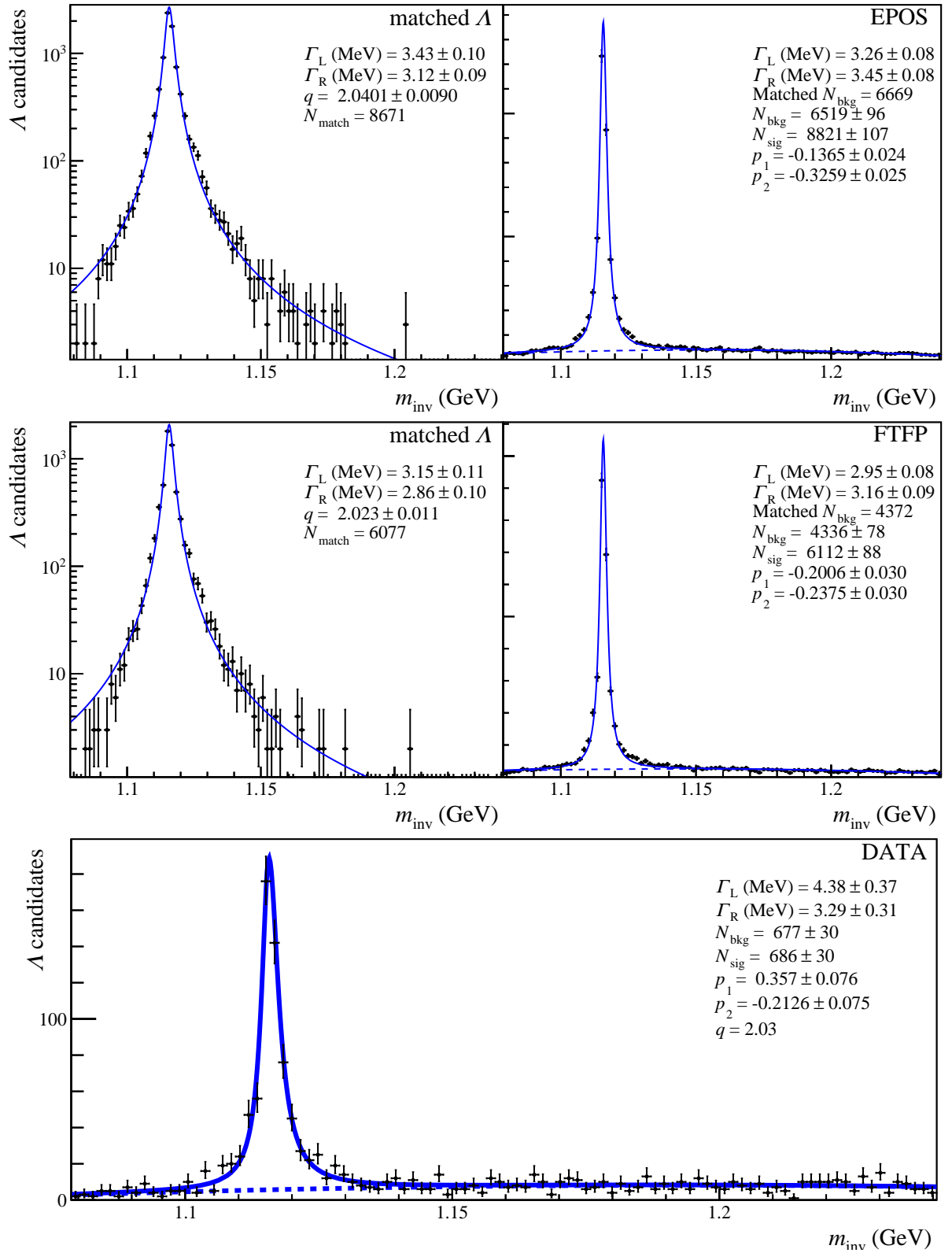
Figure 5.13: Invariant mass fit for kinematic bin $x_F \in (-0.05, 0)$, $p_T \in (0.2, 0.4)$ GeV/c, $\cos\theta_x \in [0, 0.1]$ for EPOS (*top*) and FTFP MC (*middle*) datasets, and data (*bottom*). For MC, *left* shows the first step of fit to the distribution of matched Λ particles without background (see Sec. 5.3.2), *right* shows the fit with matched p and π^- tracks.
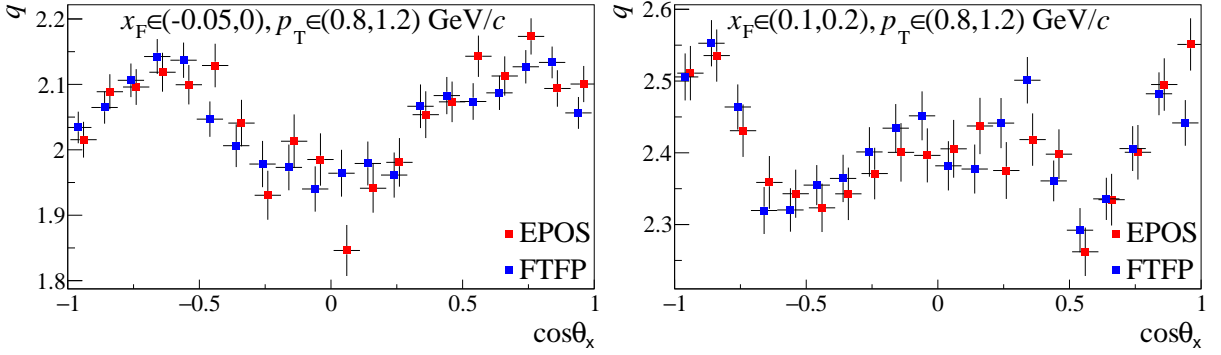
Figure 5.14: Values of fitted q value dependency on $\cos\theta_x$ in different (x_F, p_T) bins (*left*: $x_F \in (-0.05, 0)$, $p_T \in (0.8, 1.2)$ GeV/c, *right*: $x_F \in (0.1, 0.2)$, $p_T \in (0.8, 1.2)$ GeV/c) for EPOS and FTFP models.

2 to 8 MeV, with Γ_R larger than Γ_L, increasing with x_F and with a decrease of variation, and comparable across both MC datasets. For data, it is typically higher than in the MC dataset. To
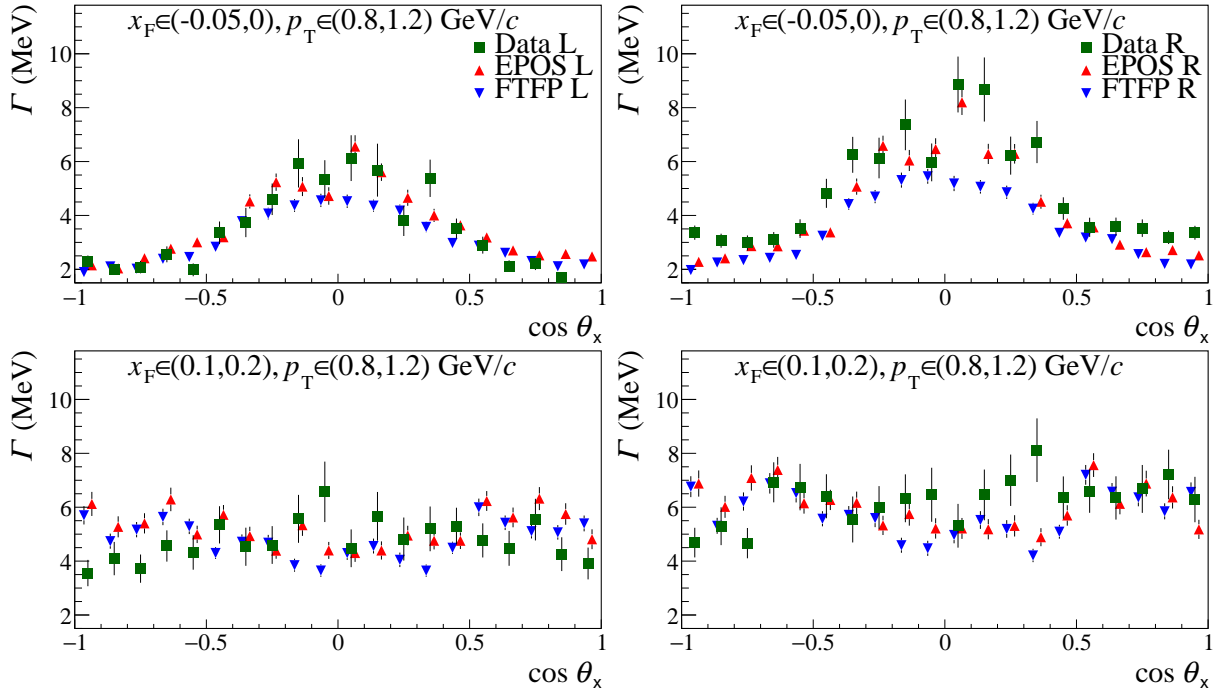
Figure 5.15: Values of fitted $\Gamma_{L,R}$ dependency on $\cos\theta_x$ in different (x_F, p_T) bins (*top*: $x_F \in (-0.05, 0)$, $p_T \in (0.8, 1.2)$ GeV/c, *bottom*: $x_F \in (0.1, 0.2)$, $p_T \in (0.8, 1.2)$ GeV/c) for EPOS and FTFP models.

compare the resulting yield N_{sig} with the number of matched Λ hyperons (N_{match}) in the same m_{inv} distribution, pulls defined as $(N_{sig} - N_{match})/\sqrt{N_{match}}$ are shown in Fig. 5.16 for EPOS and FTFP models. For $x_F < 0$, most of the pulls are distributed within ± 2, and the distribution of pulls in a specific (x_F, p_T) bin widens as x_F increases. The means of the distributions (open circles in the figures) are within ± 2, with significant outliers for high x_F. To compare the fitted uncertainties with statistical expectations, we define the *normalized uncertainty* as the ratio $\Delta N_{sig}/\sqrt{N_{sig}}$,

where ΔN_{sig} is the uncertainty of the N_{sig} obtained from the fit, displayed in Fig. 5.17. A value of this ratio close to unity indicates that the uncertainty is consistent with Poisson's statistical fluctuations: $\Delta N_{sig} \approx \sqrt{N_{sig}}$. In the forward kinematic region, defined by $x_F > 0.2$, a significant
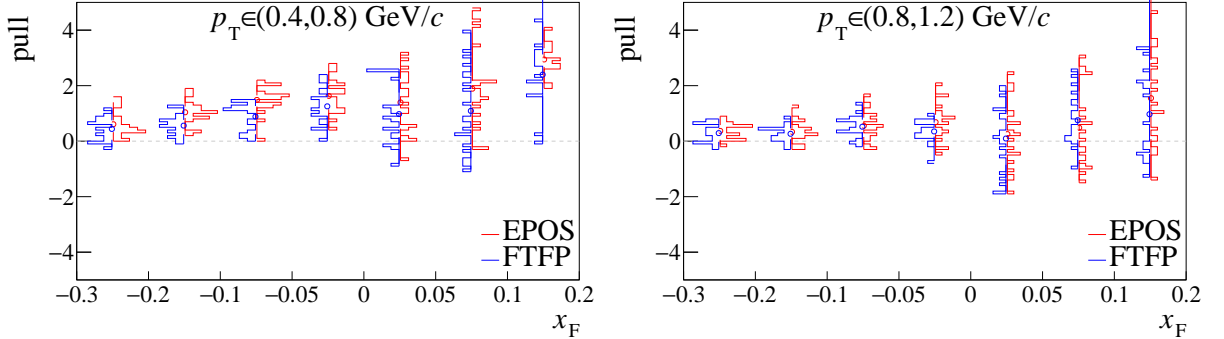
Figure 5.16: Pulls of fitted m_{inv} distribution defined as $(N_{sig} - N_{match})/\sqrt{N_{match}}$ in 20 bins in $\cos\theta_x$ in each (x_F, p_T) bin (*left*: $p_T \in (0.4, 0.8)$ GeV/c, *right*: $p_T \in (0.8, 1.2)$ GeV/c) for EPOS and FTFP models.
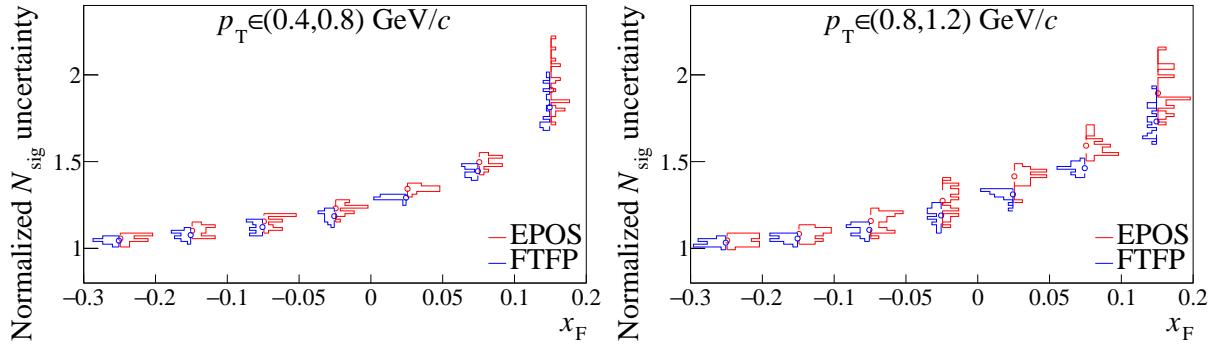
Figure 5.17: The normalized uncertainty defined as the ratio $\Delta N_{sig}/\sqrt{N_{sig}}$ of fitted m_{inv} distribution on 20 bins in $\cos\theta_x$ in each (x_F, p_T) bin (*left*: $p_T \in (0.4, 0.8)$ GeV/c, *right*: $p_T \in (0.8, 1.2)$ GeV/c) for EPOS and FTFP models.

degradation was observed in the quality and stability of the invariant mass fits. This degradation manifested in several ways, which collectively undermine the reliability of the results in this domain. Specifically, the following issues were identified:

(i) The fitted width parameters of the signal function, $\Gamma_{L,R}$, were poorly constrained by the given m_{inv} distribution, leading to significant statistical uncertainties.

(ii) The shape parameter q of the q-Gaussian signal parametrization is frequently saturated at or near its critical value of 3. It indicates an unstable fit where the signal shape becomes too broad and ill-defined, compromising the separation from the background.

(iii) The pull distributions for the signal yield, N_{sig}, showed systematic deviations from zero, indicating a significant bias in the fitting procedure in this kinematic region.

54

(iv) The normalized uncertainty of the signal yield, defined above as $\Delta N_{\text{sig}}/\sqrt{N_{\text{sig}}}$, consistently exceeded a value of three. It indicates a poorly constrained minimization and unreliable error estimation by the fitting algorithm.

Given these indicators of poor fit quality and instability, the kinematic region $x_{\text{F}} > 0.2$ was excluded from the final analysis.

Figure 5.18 shows the resulting $\cos\theta_x$ distributions for both the data and the reconstructed Monte Carlo samples. The observed shape is not flat; rather, it is an effect imposed by the experimental conditions. Specifically, the detector's geometrical acceptance and the various selection cuts applied during the analysis introduce a significant bias, distorting the true decay kinematics. These distortions necessitate the application of the MC correction procedure, described in the following section, to recover the underlying physical distribution.
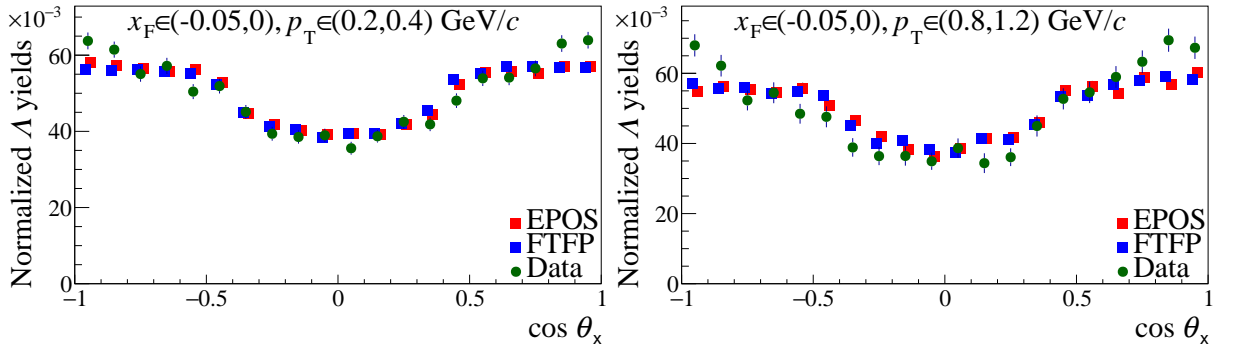
Figure 5.18: The Λ yields $\cos\theta_x$ distribution (normalized so that sum across $\cos\theta_x$ bins is 1) from m_{inv} fit (*left*: $p_{\text{T}} \in (0.4, 0.8)$ GeV/c, *right*: $p_{\text{T}} \in (0.8, 1.2)$ GeV/c) for data, EPOS and FTFP models.

5.4 MC corrections

5.4.1 Overview

In the absence of experimental biases, the theoretical angular distribution is expected to be a linear function of $\cos\theta_x$, where the slope is directly proportional to the transverse polarization, P_x (see Eq. (2.3)). As in Monte Carlo models EPOS and FTFP $P \equiv P_x \equiv 0$, the $\cos\theta_x$ distribution generated from these MC models is uniform. However, it is inherently influenced by the detector's acceptance and reconstruction capabilities. The detector acceptance and the application of selection criteria significantly reduce the number of candidates observed near $\cos\theta_x \approx 0$, as illustrated in Fig. 5.18.

In this region, the decay daughters tend to align with the momentum direction of the Λ. Generally, the momentum of a pion is lower than that of a proton. Thus, when the pion is emitted opposite to the Λ momentum $\vec{p}_\Lambda$ (*i.e.*, the proton is aligned with $\vec{p}_\Lambda$), its likelihood of detection

is reduced compared to that of the proton. Consequently, decays occurring in this kinematic configuration are more likely to be undetected.

Due to this effect and other experimental biases, the $\cos\theta_x$ distribution must be corrected to account for acceptance, selection, and reconstruction efficiency. It was done by using the unfolding method presented below.

Appendix C describes an alternative method to account for experimental biases – the method of moments. The transverse polarization obtained by this method serves as a cross-check of the unfolded result.

5.4.2 Unfolding

Due to detector acceptance and inefficiencies, the number of Λ recorded by the detector is less than the number of Λ hyperons produced in collisions. Additionally, due to the limited spatial and momentum resolution of the detector, as well as the imprecision of the reconstruction, the Λ particle produced in $\cos\theta_x$ bin j might be reconstructed in bin i. These effects are addressed using a migration matrix along with efficiency and acceptance corrections, collectively known as unfolding corrections.

The measured distribution $\mathbf{m} = \{m_i, i = 1..n_m\}$ is a disturbed truth distribution $\mathbf{t} = \{t_i, i = 1..n_t\}$ by some response matrix $\mathbf{R}$ by $m_i = \sum_{j=1}^{n_t} R_{ij} t_j$ (for this analysis in particular, the number of bins in the measured and truth distributions is identical: $n_m = n_t$). The *unfolding* problem is to find an estimator for $\mathbf{t}$, $\hat{\mathbf{t}}$ from known $\mathbf{m}$ and $\mathbf{R}$. The response matrix element R_{ij} is the conditional probability that a Λ particle is found with a measured value in bin i given that the true value was in bin j. The simulated events are used first to determine the transfer matrix N_{ij}, defined as the number of Λ hyperons measured in bin i that are expected to be found in bin j. The response matrix is then

$$R_{ij} = \frac{N_{ij}}{N_j}, \tag{5.12}$$

where $N_j \geq \sum_{k=1}^{n_m} N_{kj}$ is the total number of simulated particles in bin j (inequality means reconstruction losses) and N_{ij} is the yield of matched Λ hyperons in bin i that was simulated in bin j. The examples of transfer matrix for three (x_F, p_T) bins are shown in Fig. 5.19 for the EPOS MC dataset, where polarization is zero ($P_x \equiv 0$). The transfer matrix looks similar in the FTFP MC case. The $x_F < 0$ region is characterized by small off-diagonal elements, while smearing becomes more pronounced as x_F increases. In the bin $x_F \in (0.2, 0.3)$, the smearing in $\cos\theta_x$ becomes so severe that the unfolded $\cos\theta_x$ distribution acquires a significant uncertainty, resulting in a polarization uncertainty greater than 0.1. This provides additional confirmation that excluding the region $xF > 0.2$ from the analysis was necessary.

Several techniques are employed to perform unfolding, each with trade-offs in terms of complexity, stability, and interpretability; these methods are thoroughly discussed in Refs.[146, 151, 152], including uncertainty propagation. In this thesis, RooUnfold software [151] is used.

The first one is referred to here as **inverse matrix unfolding**. Consider the case where the number of bins in the truth and observed histograms is equal, and the inverse matrix $\mathbf{R}$ exists, the

$x_\text{F} \in (-0.05, 0)$, $p_\text{T} \in (0.2, 0.4)$ GeV/c

$x_\text{F} \in (-0.3, -0.2)$, $p_\text{T} \in (0.8, 1.2)$ GeV/c

$x_\text{F} \in (0.2, 0.3)$, $p_\text{T} \in (0.8, 1.2)$ GeV/c
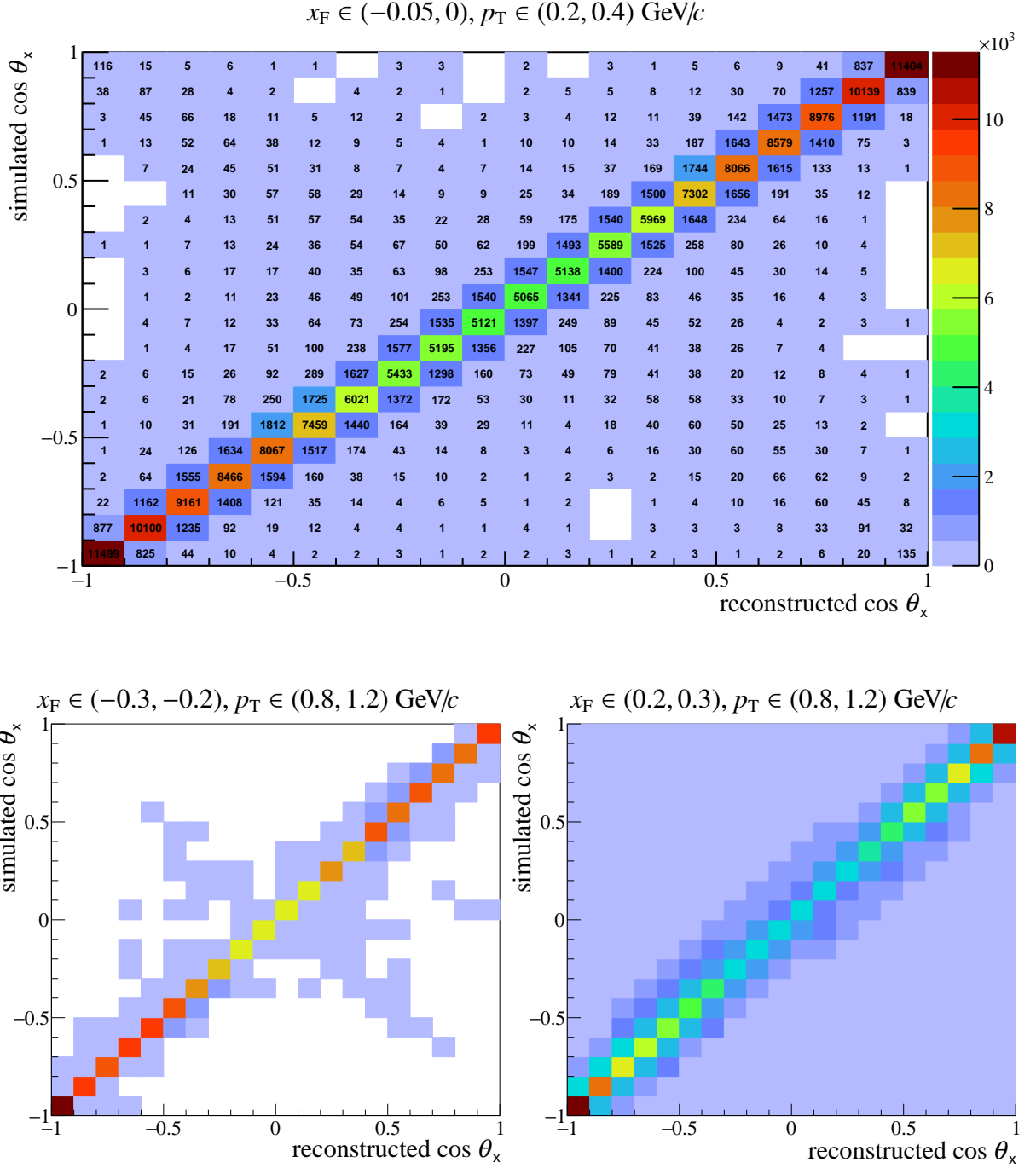
Figure 5.19: The transfer matrix N_{ij} of matched Λ hyperons on 20 bins in $\cos\theta_\text{x}$ in different (x_F, p_T) bins for EPOS model: midrapidity (*top*), backward (*bottom left*) and forward (*bottom right*) hemispheres. See text for details.

truth distribution may be directly estimated as

$$\hat{\mathbf{t}} = \mathbf{R}^{-1}\mathbf{m} \,. \tag{5.13}$$

For the covariance matrix, we find

$$cov(t_i, t_j) = \mathbf{V}_t = \mathbf{R}^{-1}\mathbf{V}_m(\mathbf{R}^{-1})^T \,, \tag{5.14}$$

where $(\mathbf{V}_m)_{ij} = cov(m_i, m_j)$ is the covariance matrix of the measured distribution, and $\mathbf{V}_t$ is the covariance matrix for the estimators of the truth distribution. In this thesis, the covariance of the measured distribution is a diagonal matrix with entries that are squared uncertainties Δm_i:

$$(\mathbf{V}_m)_{ij} = \text{diag}\left\{(\Delta m_i)^2\right\} \,. \tag{5.15}$$

Formally, Eq. (5.13) is the solution to the least-square minimization problem[2]:

$$\mathcal{L}(\mathbf{t}) = (\mathbf{m} - \mathbf{Rt})^{\mathrm{T}}\mathbf{V}_m^{-1}(\mathbf{m} - \mathbf{Rt}) \,, \tag{5.16}$$

and the solution is

$$\hat{\mathbf{t}} = (\mathbf{R}^{\mathrm{T}}\mathbf{V}_m\mathbf{R})^{-1}\mathbf{R}^{\mathrm{T}}\mathbf{m} \,, \tag{5.17}$$

that simplifies to (5.13) if the number of bins in $\mathbf{m}$ and $\mathbf{t}$ is equal.

This method gives zero bias, *i.e.*, if the sample size grows infinitely large, its expected value converges to the true parameter value. However, this method may amplify statistical fluctuations in the unfolding spectra and is sensitive to statistical fluctuations in the response matrix. To mitigate this issue, various methods were developed based on the idea of *regularization*. A typical example is the iterative regularization used in this thesis, called Richardson-Lucy (also Iterative, or Bayesian) unfolding [153]: the initial guess for truth distribution $\hat{t}_i$ is uniform, then updated using Bayes' theorem:

$$\hat{t}_i^{(new)} = \sum_j \left(\frac{R_{ji}t_i}{\sum_k R_{jk}t_k}\right)m_j \,. \tag{5.18}$$

The regularization parameter here is the number of iterations. The criterion to choose this number is that the introduced change of update from $\hat{t}^{(k-1)^{\mathrm{th}}}$ to $\hat{t}^{k^{\mathrm{th}}}$ per degree of freedom is less than one, *i.e.*, $\chi^2/\text{ndf} < 1$. For the covariance matrix formula and uncertainty propagation, see Ref. [153].

The resulting truth estimate $\hat{\mathbf{t}}$ distribution is then fitted to the function $f(P, \cos\theta_x) = (1 + \alpha P\cos\theta_x)/2$ (Eq. (2.3)) via non-linear least squares minimization with two parameters: polarization P and normalization parameter N:

$$\chi^2(N, P) = \sum_{ij}(t_i - Nf(P, x_i))^{\mathrm{T}}(\mathbf{V}_t^{-1})_{ij}(t_j - Nf(P, x_j)) \,, \tag{5.19}$$

---

[2]This may be modeled as a log-likelihood function of Gaussian-distributed m_i values.

where x_i is the center of the corresponding i^{th} $\cos\theta_{\mathsf{x}}$ bin.

For the final result in Chapter 6, the inverse matrix unfolding is used because it yields a lower χ^2 value. The iterative method was used in the systematic uncertainty estimation, detailed in Sec. 5.7.

5.5 MC correction tests

The tests with Monte Carlo simulated events are an essential validation procedure in this analysis, designed to verify the correctness and robustness of the unfolding technique used to correct detector effects and recover the true underlying distribution. In this test, one Monte Carlo (MC) sample is processed through the complete analysis chain and subsequently unfolded using the response matrix derived from a statistically independent MC sample. The unfolded distribution is then compared to the known truth-level spectrum of the corresponding MC sample, and the polarization value is compared with the expected value.

5.5.1 MC with zero polarization

EPOS by EPOS

The EPOS MC dataset was divided into two statistically independent samples in a 5:1 ratio, which approximately reproduces the ratio between data and EPOS MC statistics. The $\cos\theta_{\mathsf{x}}$ distribution from the smaller sample, denoted as the *EPOS-2 dataset*, was unfolded by the larger one, denoted as the *EPOS-1 dataset*. Corresponding distributions are displayed in Fig. 5.20. Uncertainties in the truth distributions, e.g. *EPOS-2 gen*, are defined as the square root of the Λ yields. Uncertainties in the unfolded distributions are defined as the square roots of the diagonal elements of the covariance matrix given in Eq. 5.14, i.e. $\Delta t_i = \sqrt{(\mathbf{V}_t)_{ii}}$. The unfolded $\cos\theta_{\mathsf{x}}$ distributions were then fitted to the function (Eq. (2.3)), as discussed in Sec. 5.4.2. The polarization values for the analyzed $(x_{\text{F}}, p_{\text{T}})$ bins (treated as polarization bias) are depicted in Fig. 5.21. The resulting polarization values are consistent with zero, and there is no visible dependence on x_{F} and p_{T}, with deviations up to 0.035 in one bin $x_{\text{F}} \in (-0.3, -0.2)$, $p_{\text{T}} \in (0.8, 1.2)$ GeV/c.

FTFP by EPOS

A similar outcome is observed for the $\cos\theta_{\mathsf{x}}$ distributions of Λ yields from FTFP MC dataset unfolded by EPOS MC. Corresponding distributions are displayed in Fig. 5.22. As shown in the figure for two particular $(x_{\text{F}}, p_{\text{T}})$ bins, the unfolded FTFP Monte Carlo distribution by EPOS MC (light blue) closely reproduces the truth, generated particle distribution (orange); it is consistent across the measured phase space. Two examples of fits are shown in Fig. 5.23. The polarization bias values for the analyzed $(x_{\text{F}}, p_{\text{T}})$ bins are depicted in Fig. 5.24. The results are consistent with zero, with deviations up to 0.05. As described in Sec. 5.7, these deviations are considered as systematic uncertainty in the measurement.
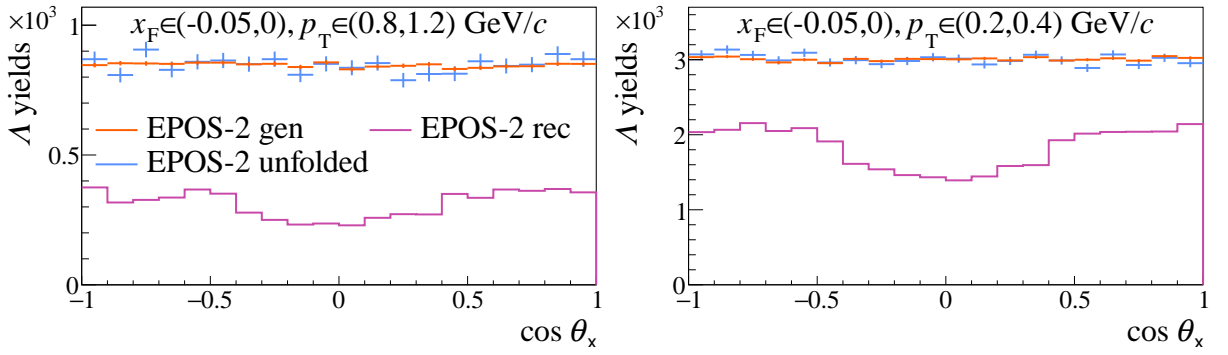
Figure 5.20: The distributions of $\cos\theta_x$ for Λ hyperons in ($x_F \in (-0.05, 0)$ *left*: ($p_T \in (0.8, 1.2)$ GeV/c, *right*: $p_T \in (0.2, 0.4)$ GeV/c): EPOS-2 generated (truth distribution) (*EPOS-2 gen*, orange), EPOS-2 reconstructed (*EPOS-2 rec*, pink), and EPOS-2 MC dataset corrected (unfolded) by EPOS1 MC dataset (*EPOS-2 unfolded*, light blue). Only statistical uncertainties are shown.
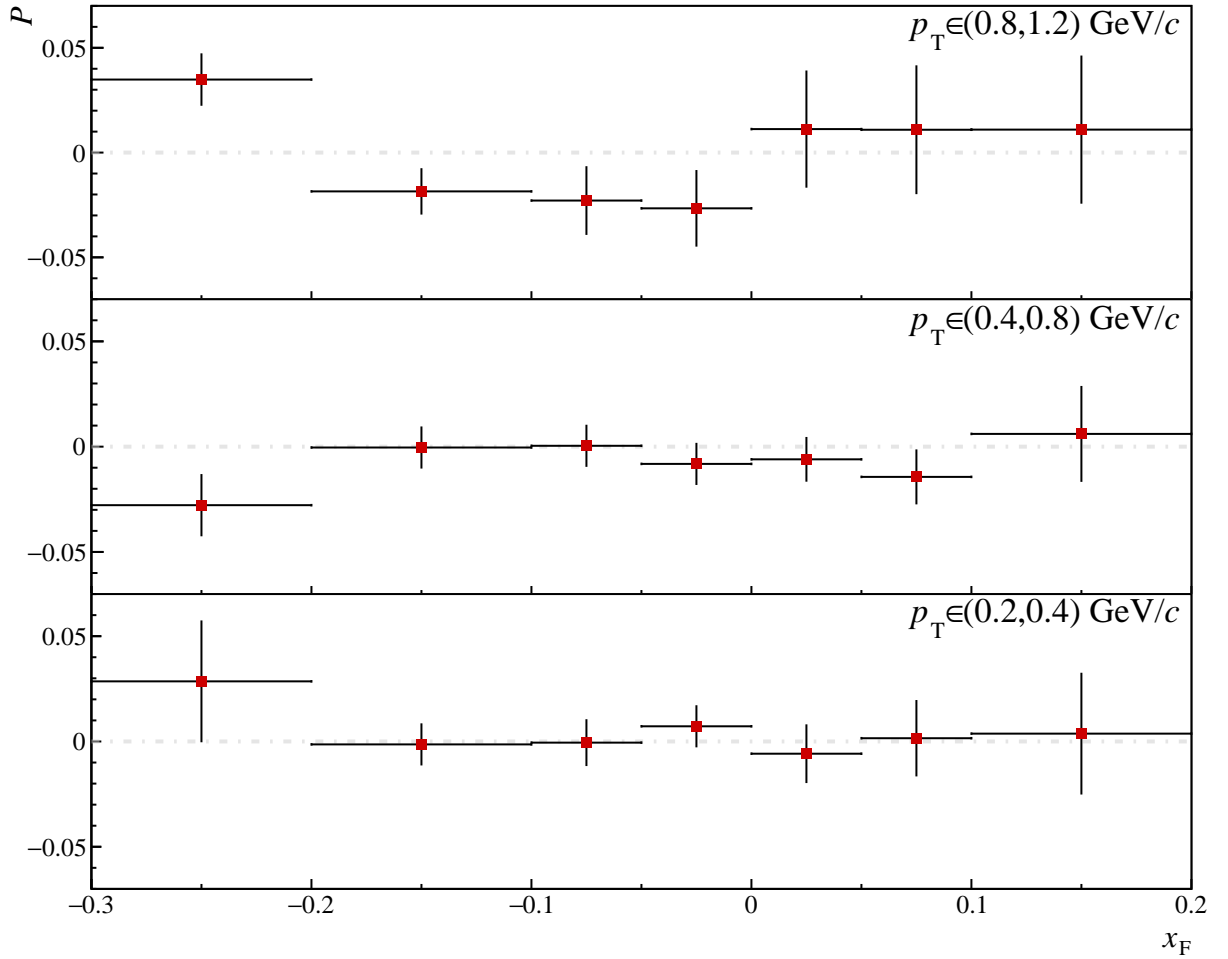
Figure 5.21: Measured Λ transverse polarization bias in the closure test for different (x_F, p_T) bins. The results are obtained by unfolding the smaller *EPOS2* Monte Carlo sample using the response matrix derived from the larger, statistically independent *EPOS1* sample via matrix inversion.
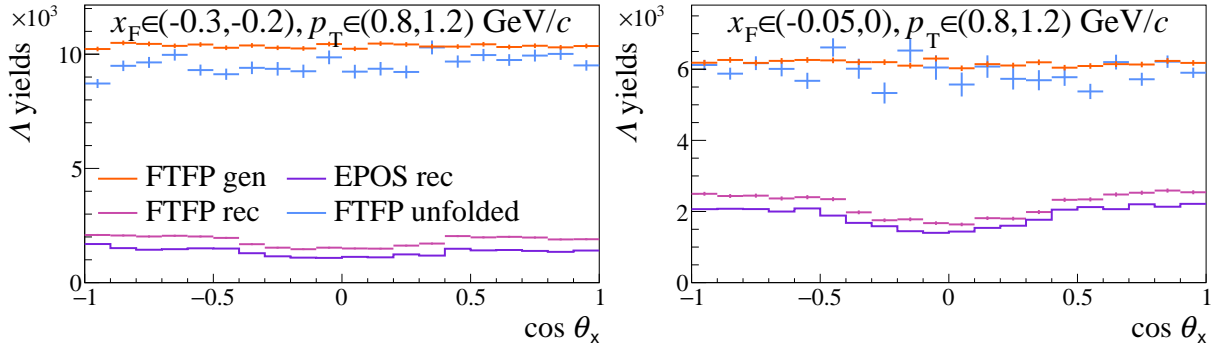
Figure 5.22: The distributions of $\cos\theta_x$ for Λ hyperons in different (x_F, p_T) bins ($p_T \in (0.8, 1.2)$ GeV/c, *left*: $x_F \in (-0.3, -0.2)$, *right*: $x_F \in (-0.05, 0)$) for FTFP MC dataset corrected (unfolded) by EPOS MC model: FTFP generated (truth distribution) (*FTFP gen*, orange), FTFP reconstructed (*FTFP rec*, pink), EPOS reconstructed (*EPOS rec*, violet), FTFP unfolded data (light blue). Only statistical uncertainties are shown.
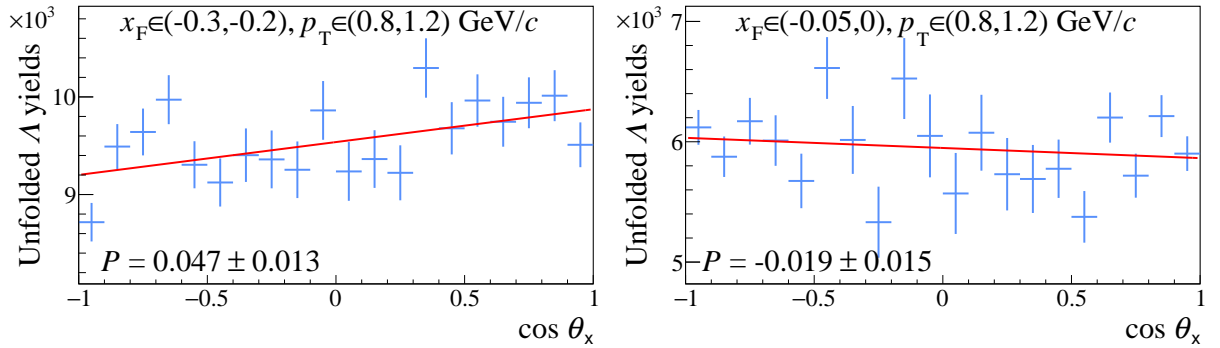
Figure 5.23: The unfolded Λ hyperon $\cos\theta_x$ distributions in different (x_F, p_T) bins ($p_T \in (0.8, 1.2)$ GeV/c, *left*: $x_F \in (-0.3, -0.2)$, *right*: $x_F \in (0, 0.05)$) for FTFP MC using EPOS MC dataset for the unfolding, and red line is the fitted function (See Eq. 2.3 and Sec. 5.4.2). Polarization uncertainties shown here are propagated from statistical uncertainties of Λ yields in $\cos\theta_x$ bins.
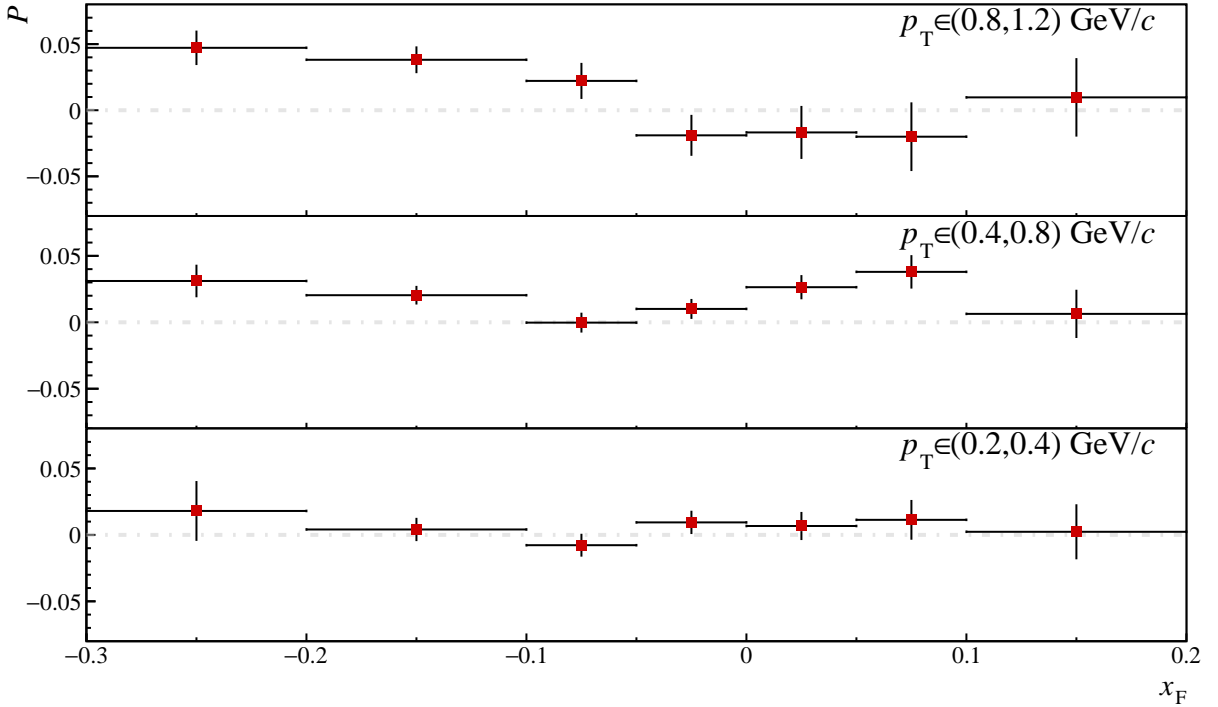
Figure 5.24: Measured Λ transverse polarization bias in the test for different (x_F, p_T) bins, with FTFP MC dataset unfolded via matrix inversion by EPOS MC dataset.

5.5.2 MC with polarization

The polarization reweighting technique serves as a crucial systematic check for this analysis, validating whether an unpolarized Monte Carlo (MC) simulation can reliably unfold data containing polarization effects.

This test is implemented by applying the polarization-dependent weight factor

$$w(\cos\theta_x) = 1 + \alpha_\Lambda P \cos\theta_x \qquad (5.20)$$

which is applied to each $p\pi^-$ pair to incorporate polarization effects in the invariant mass fit (see Ref. [154] for the formalism of weighted unbinned maximum likelihood fit). The values $P = 0.2$ for $x_F < 0$ and $P = -0.2$ for $x_F > 0$ are selected as approximate maximum values of transverse polarization expected in the considered kinematic region.

The polarization bias value for the analyzed (x_F, p_T) bin is depicted in Fig. 5.25. It shows a consistent, correct polarization value, $P_{\text{expected}} = \pm 0.2$, with deviations from the expected values and statistical uncertainties slightly larger than those in the closure test in the previous section.
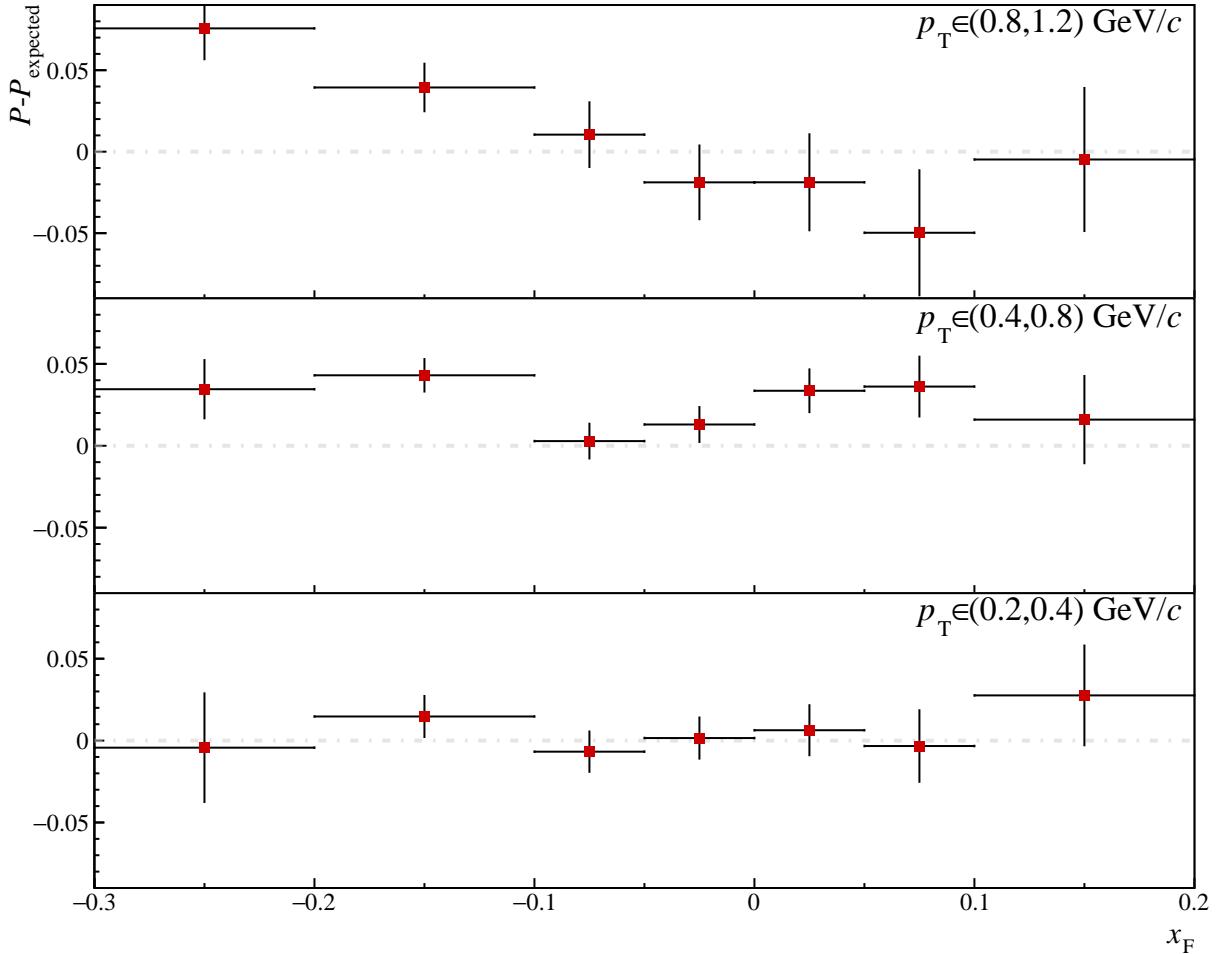
Figure 5.25: The variation of measured Λ transverse polarization bias from the expected value $P_{\text{expected}} = \pm 0.2$ in the MC test for different (x_F, p_T) bins, with reweighted FTFP MC dataset unfolded via matrix inversion by the EPOS MC dataset.

5.6 Statistical uncertainty

In summary of the methodology described above, the statistical uncertainty propagation from the experimental data to the polarization values is briefly reminded below.

The statistical uncertainty ΔN_{sig} of the Λ yield N_{sig} from m_{inv} fit in $(x_F, p_T, \cos\theta_x)$ bins is defined from the likelihood fit, as described in Sec. 5.3.2. Then, the N_{sig} and ΔN_{sig} values were used for unfolding, with uncertainty propagation described in detail in Sec. 5.4.2. Finally, the covariance matrix from unfolded $\cos\theta_x$ spectra was used for least-squares fit (Eq. (5.19)). The statistical uncertainty of the resulting polarization value ΔP is determined using the MINUIT2 minimization library [148, 149].

5.7 Systematic uncertainties

For systematic uncertainties, the variation of parameters of the event and track cuts, fitting, and unfolding procedures is considered and checked. Most variations are more **tight** (*i.e.*, more

restrictive than the standard cut) or **loose** (less restrictive) cuts, with values described below.

For event and track cuts, their variations are the following:

(i) The window in which off-time beam particles are excluded (*WFA cut*) is $1.5 \pm 0.5 \, \mu s$.

(ii) The primary vertex position z-coordinate is within target, but the target is shifted by ± 2 cm along z-axis (*Primary Vertex z cut*), *i.e.* $z \in [-593.2, -572.9]$ cm and $z \in [-589.2, -568.9]$ cm.

(iii) The energy loss cut (*dE/dx cut*) is changed from the standard value of 3σ to $\pm 2.5\sigma$ and $\pm 3.5\sigma$ of the nominal Bethe-Bloch value.

(iv) Minimal number of clusters in VTPCs (*VTPC clusters cut*) is 15 ± 3.

(v) The difference between the z-coordinate positions of the primary vertex and decay vertex (Δz *cut*) is $\Delta z = 10 \pm 3$ cm.

(vi) Cut on $|\cos\theta_z|$ ($\cos\theta_z$ *cut*) is varied as 0.95 ± 0.03.

(vii) Impact point ($b_{x,y}$) ($b_{x,y}$ *cut*): $(0.5 \cdot b_x)^2 + (b_y)^2 < (1 \pm 0.25)$ cm^2.

These variations describe the uncertainty regarding the efficiency of the event selection and reconstruction bias, as well as the identification of Λ particles.

The systematic uncertainties originating from the m_{inv} signal parametrization and MC correction are estimated from the following modifications:

(i) Variation of m_{inv} range fit (*m_{inv} range variation*): tight/loose ± 5 MeV from the upper and lower limits of m_{inv} range.

(ii) Variation of parameters for the m_{inv} distribution fit (*m_{inv} fit parameters*): m_Λ is a free parameter with limits of ± 5 MeV, the initial values of $\Gamma_{\mathrm{L,R}}$ for the fit are varied by $\pm 20\%$.

(iii) The q value in the q-Gaussian function is taken from only the EPOS or FTFP MC dataset fits instead of the weighted average (*q value variation*).

(iv) The MC simulation is performed according to a particular physics model. A possible uncertainty arising from the simulation model is estimated as the difference between unfolding using the EPOS and FTFP models (*MC model*).

(v) Instead of inverse matrix unfolding, iterative unfolding is used (*Unfolding method*). While the primary assessment for this uncertainty involves comparing the results obtained using the inverse matrix method and the iterative unfolding method, other unfolding algorithms were also tested. These additional tests indicate that results obtained using alternative methods are comparable to those yielded by the inverse and iterative approaches within their respective uncertainties.

The short names of the contributions are given in *italic*. The values of variations are selected in a way that the analysis procedure remains stable under these variations, and they correspond to uncertainties of these parameters and/or differences in data and MC. For example, the reconstructed tracks in the MC contain a few percent more clusters than tracks from data, likely because the simulation does not account for faulty front-end electronics channels in the detector or periodic detector noise. The typical resolution of the primary vertex and V^0 fitting is several centimeters in the z direction and a few millimeters in the x, y directions, and the resolution of $\cos\theta$ is on the order of 0.03 to 0.1.

For each bias listed above, a larger variation from the resulting value is taken as a contribution to systematic uncertainty. Uncertainties originating from different sources are assumed to be uncorrelated. The total uncertainty is considered symmetric and is calculated as the sum in quadrature of all uncertainties.

The sources of systematic uncertainties that are not considered in this analysis are the following:

(i) The parity-violating decay asymmetry value for Λ $\alpha = 0.747 \pm 0.009$ has a relative uncertainty 0.1%, therefore is considered fixed.

(ii) The target-out contribution of proton beam interaction, studied in Ref. [145], has 10 times less size statistics and is not present here. The standard procedure for correcting off-target interactions involves performing identical analyses on two datasets: one with the target inserted (full LHT) and the other with the target removed (empty LHT). To eliminate the contribution from interactions occurring outside the target material, the results obtained from the empty target data are subtracted from those of the full target data after applying an appropriate normalization factor. However, in the context of this analysis, this approach is not feasible as the statistical precision of the analysis of target-removed events is insufficient. Consequently, a tight cut is applied to the longitudinal coordinate of the primary interaction vertex (*Primary Vertex z cut*) to suppress the off-target contribution instead.

(iii) The function used for background contribution in m_{inv} fit, only a Chebyshev polynomial of 2nd order, is considered. Applying a 1st order polynomial leads to a bad description of the background spectrum, whilst a 3rd order polynomial results in unstable fits.

(iv) Residual K_S^0 contamination of the signal in the kinematic regions where both (i) mean energy loss dE/dx value coincides for proton and pion, and (ii) invariant mass m_{inv} for Λ candidates coincides with K_S^0 candidates, leading to indistinguishability of Λ and K_S^0 candidates.

Because it is experimentally infeasible to separate direct production of Λ in $p+p$ ($p+N$) process from indirect production channels $\Sigma^0 \rightarrow \Lambda\gamma$ and $\Xi \rightarrow \Lambda\pi$, the measured polarization is usually reported as the average over both processes. A theoretical calculation of the polarization of Λ hyperons arising from decay $\Sigma^0 \rightarrow \Lambda\gamma$ yields the relation $P_\Lambda = -\frac{1}{3}P_{\Sigma^0}$. One can infer that the

absolute polarization of directly produced Λ hyperons exceeds the inclusive measurement by approximately 25% [16], depending on the estimation of Σ^0 polarization and multiplicity. Hence, throughout the thesis, the Λ **yield** has to be understood as that of $\Lambda + \Sigma^0$.

5.8 Λ precession in a magnetic field (classical treatment)

As the Λ hyperon has a nonzero magnetic moment, it interacts with the magnetic field inside the Time Projection Chambers. Consequently, one has to investigate and quantitatively estimate whether a magnetic field can influence the polarization measurements (in addition to the cuts studied earlier). In this section, the EPOS MC dataset is analyzed.

The classical covariant equation describing the spin motion, known as the Bargmann-Michel-Telegdi (BMT) equation, has the following form [155]:

$$\frac{dS^\alpha}{d\tau} = \frac{ge}{2m} \left[F^{\alpha\beta} S_\beta + u^\alpha \left(S_\beta F^{\beta\mu} u_\mu \right) \right] - u^\alpha \left(S_\beta \frac{du^\beta}{d\tau} \right), \tag{5.21}$$

where S^α is the Pauli-Lubański spin four-vector, u^α is the four-velocity of a particle, $F^{\alpha\beta}$ is the electromagnetic field tensor, and τ is the proper time. The Einstein summation convention over $\beta, \mu = 0, 1, 2, 3$ is implied. Here $\frac{ge}{2m} = \mu_\Lambda \mu_N$, where μ_N is the nuclear magneton and $\mu_\Lambda = -0.613$ is the magnetic moment of Λ in μ_N units [12]. For Λ particle in the rest frame, the spin four-vector has the form $S^\alpha = (0, \vec{S})$, where $\vec{S}$ is the particle's spin vector, $\left| \vec{S} \right| = 1$. As gradient force terms like $\nabla(\vec{m} \cdot \vec{B})$ are negligible (see Appendix B.3), and there are no other forces because Λ is a neutral particle, so $u^\alpha = $ const, and the last term in Eq. (5.21) can be ignored. Hence, in the Λ rest frame, the spin evolution is described by the formula:

$$\frac{d\vec{S}}{d\tau} = \mu_\Lambda \mu_N \left[\vec{S} \times \vec{B}' \right], \tag{5.22}$$

where $\vec{B}'$ is the magnetic field in rest frame in terms of NA61/SHINE magnetic field $\vec{B}$ (electric field in TPC has been neglected)

$$\vec{B}' = \gamma \vec{B} - (\gamma - 1)(\vec{B} \cdot \vec{p}_\Lambda) \vec{p}_\Lambda / \left| \vec{p}_\Lambda \right|^2. \tag{5.23}$$

To compute the angle of precession, Eq. (5.22) is numerically integrated. The spatial dependence of the magnetic field strength $\vec{B}(\vec{r})$ is taken from the NA61/SHINE software package. For further convenience, we consider the change of variables to $d\text{z} = \frac{p_z}{m} c d\tau$ and rewrite Eq. (5.22) as

$$\frac{d\vec{S}}{d\text{z}} = \frac{\mu_\Lambda \mu_N}{(p_z/m)} \left[\vec{S} \times \vec{B}'(\vec{r}) \right]. \tag{5.24}$$

Finally, the integration over the z-coordinate with a step size of $\Delta z = 1$ cm is performed.

An example of the space evolution of the three spin vector components of Λ in the NA61/SHINE

spectrometer magnetic field for the momentum $\vec{p}_\Lambda = (0, 0, 40)$ GeV/c is shown in Fig. 5.26 (*left*). In this case, the distance traveled by the Λ is quite substantial due to the time dilation effect caused by the large Λ momentum. Magnetic field magnitude along the beamline is shown in Fig. 5.26 (*right*).
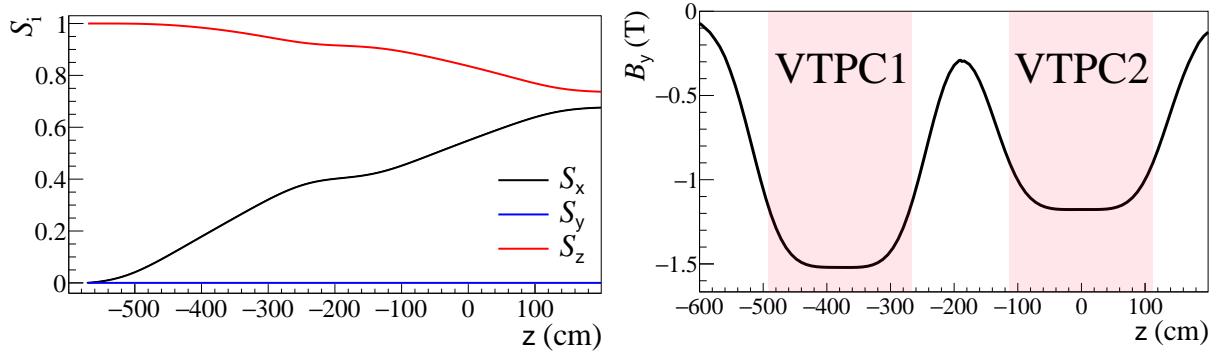
Figure 5.26: *Left*: An extreme example showing the evolution of the spin vector components of the Λ hyperon in the NA61/SHINE spectrometer magnetic field for the momentum $\vec{p}_\Lambda = (0, 0, 40)$ GeV/c. *Right*: Magnetic field along the beamline (z) direction in the NA61/SHINE reference frame. Here x = y = 0 and the B_y field has only the (negative) y-component.

The large value of z $\approx$ 200 cm is possible only for the most energetic Λ hyperons, however, taking into account the exponential law of decay, the majority of particles simulated with EPOS decay with z < -400 cm, which is shown in Fig. 5.27 (*left*). Dependence of the corresponding precession angle ϕ_{max} on the position of decay z is shown in Fig. 5.27 (*right*). It may reach 0.35 rad; however, for most of the particles, it remains below 0.1 rad.
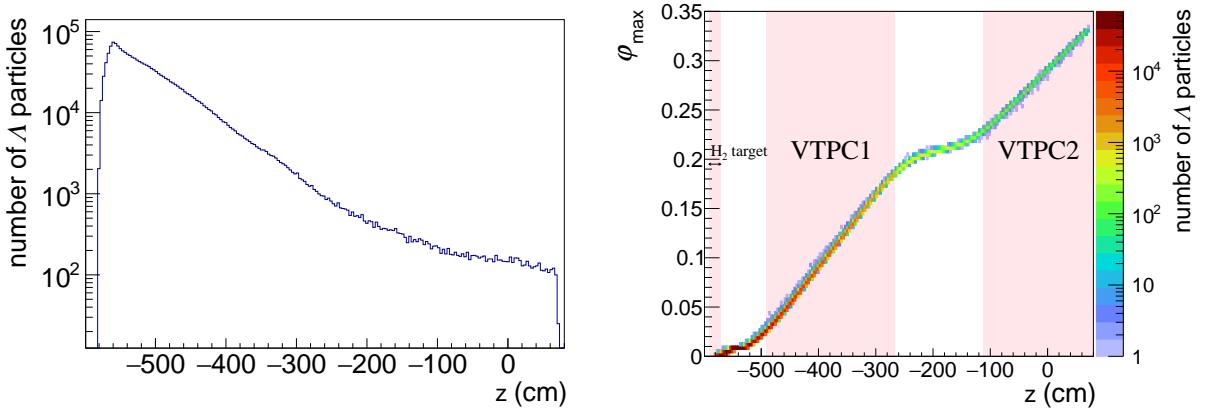
Figure 5.27: *Left*: The distribution of the z coordinate of the Λ decay point (after cuts). *Right*: The dependence of the maximum precession angle ϕ_{max} on the z-coordinate point of Λ decay z. The target is located at z $\in [-591, -571]$ cm.

The same numerical simulations can be used to determine the influence of the magnetic field on the polarization measurement bias. To include the NA61/SHINE geometry in this analysis, the following selection Λ track cuts are imposed:

(i) number of hits in VTPCs ≥ 15 for both proton and pion tracks[3],

(ii) for the difference between the z-coordinate of Λ vertex (decay point) and the primary vertex, $\Delta z = z - z_{PV}$, the cut $\Delta z \geq 10$ cm is applied.

The initial Λ spin vector $\vec{S}$ is generated uniformly distributed on a unit sphere and propagated in the magnetic field until the particle's decay, according to Eq. (5.24). Next, the vector $\vec{S}$ is projected along the directions $\hat{n}_x$, $\hat{n}_y$, and $\hat{n}_z$. The distributions of the spin vector components after the evolution in kinematic range $x_F \in (-0.3, 0.2)$, $p_T \in (0.2, 1.2)$ GeV/c are presented in Fig. 5.28, with polarization values defined as mean $P_i = \langle S_i \rangle$ and uncertainty computed using the bootstrap method [156]. The polarization bias components for different (x_F, p_T) bins are shown
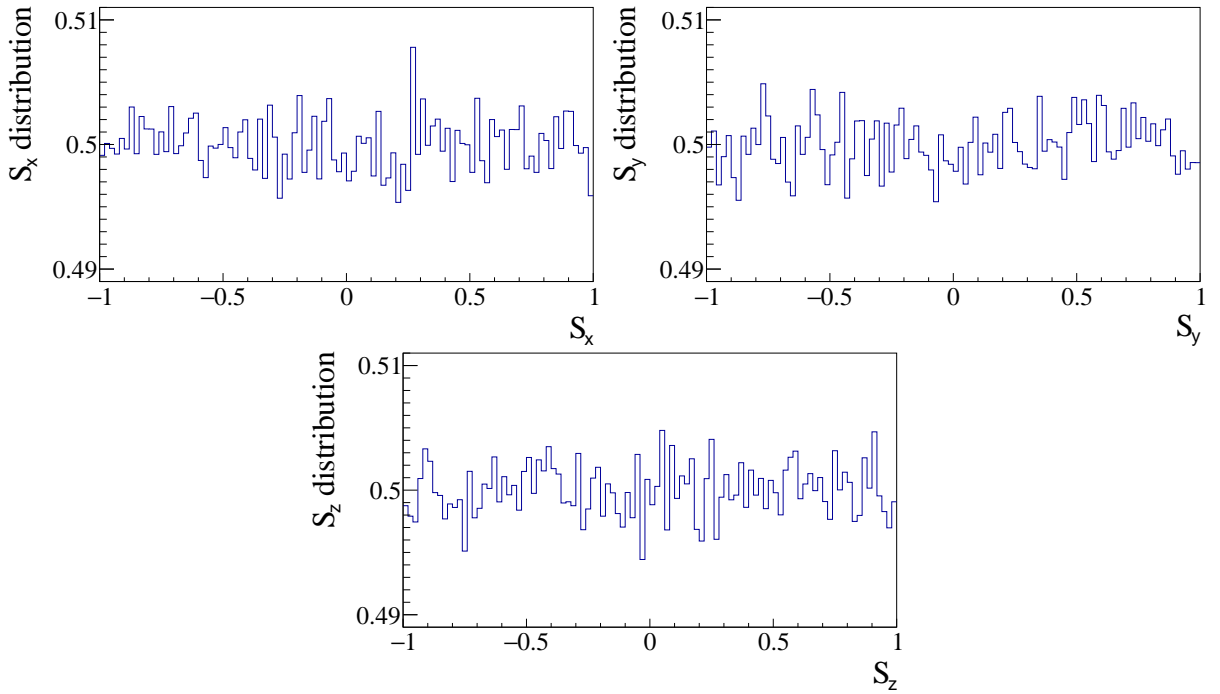
Figure 5.28: Polarization vector $\vec{S}$ distribution. Polarization values are $P_x = -0.00011 \pm 0.00025$, $P_y = -0.00030 \pm 0.00024$, and $P_z = 0.00015 \pm 0.00024$.

in Fig. 5.29. Numerical values are presented in Table D.2 in Appendix D. The observed effect is smaller than 0.01, consistent with zero for many of the (x_F, p_T) bins.

As a result, the magnetic field bias is much smaller than systematic uncertainties from other sources and is not included in the total systematic uncertainty (see Sec. 5.7).

---

[3]The *hits* in TPCs result from a simulation of particles' passage through the detector before the reconstruction procedure.
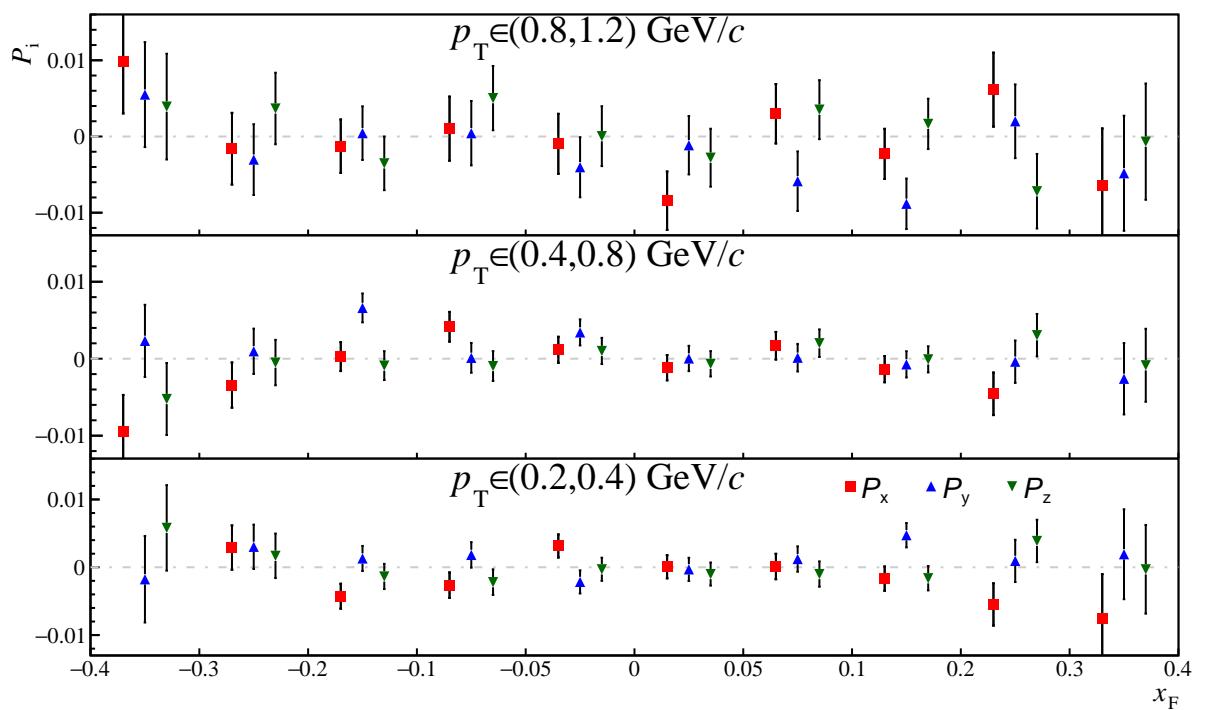
Figure 5.29: Polarization vector bias (P_x, P_y, P_z) resulting from precession in a magnetic field is shown for different (x_F, p_T) binning.

Chapter 6

Results

The measured $\cos\theta_x$ distributions from the experimental data for two (x_F, p_T) bins are shown in Fig. 6.1 together with the unfolded distributions. The uncertainties shown here were propagated from statistical uncertainties from Λ yields in $\cos\theta_x$ bins, as defined in Sec. 5.4.2. The unfolded
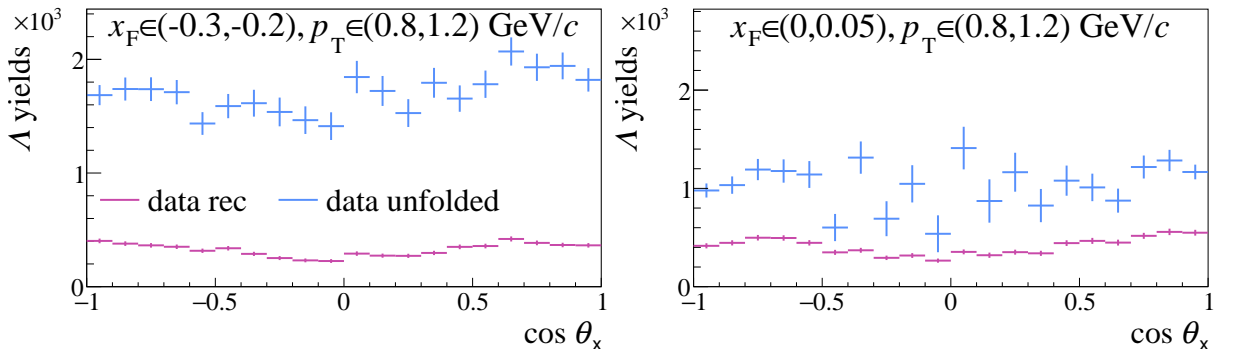
Figure 6.1: The $\cos\theta_x$ distributions of Λ particles in two selected bins $x_F \in (-0.3, -0.2)$, $p_T \in (0.8, 1.2)$ GeV/c (*left*) and $x_F \in (0, 0.05)$, $p_T \in (0.8, 1.2)$ GeV/c (*right*). The plots show the spectra of reconstructed NA61/SHINE data (red) and unfolded data (light blue).

$\cos\theta_x$ distributions of Λ hyperons using the EPOS MC dataset via the inverse response matrix unfolding method, along with the fitted function (Eq. 2.3) for selected (x_F, p_T) bins, are displayed in Fig. 6.2.

The Λ transverse polarization obtained using unfolding as a function of x_F in three p_T bins is presented in Fig. 6.3 with statistical and systematic uncertainties. The polarization component P_y, which is expected to be zero due to parity conservation in strong interactions as discussed in Sec. 2.3.1, was analogously measured as a control for potential systematic biases and is presented in Fig. 6.4 as a function of x_F in three p_T bins with statistical and systematic uncertainties. The obtained values for P_y across all kinematic bins were found to be consistent with zero, confirming the absence of significant detector-induced false polarization signals. Furthermore, the statistical and systematic uncertainties on the P_y component were observed to be of a similar magnitude to those of the primary transverse component, $P \equiv P_x$.

Additionally, Fig. 6.5 shows a comparison of the statistical and systematic uncertainties across all (x_F, p_T) bins in the current analysis. An examination of these uncertainties reveals that the statistical uncertainties are generally comparable in magnitude to the total systematic uncertainties across the analyzed kinematic range. Overall, both uncertainties are found to be lowest around midrapidity ($x_F \approx 0$). The systematic uncertainty dominates for backward ($x_F < 0$) and forward ($x_F > 0$) hemispheres at $p_T \in (0.2, 0.4)$ GeV/c, across the all x_F bins at
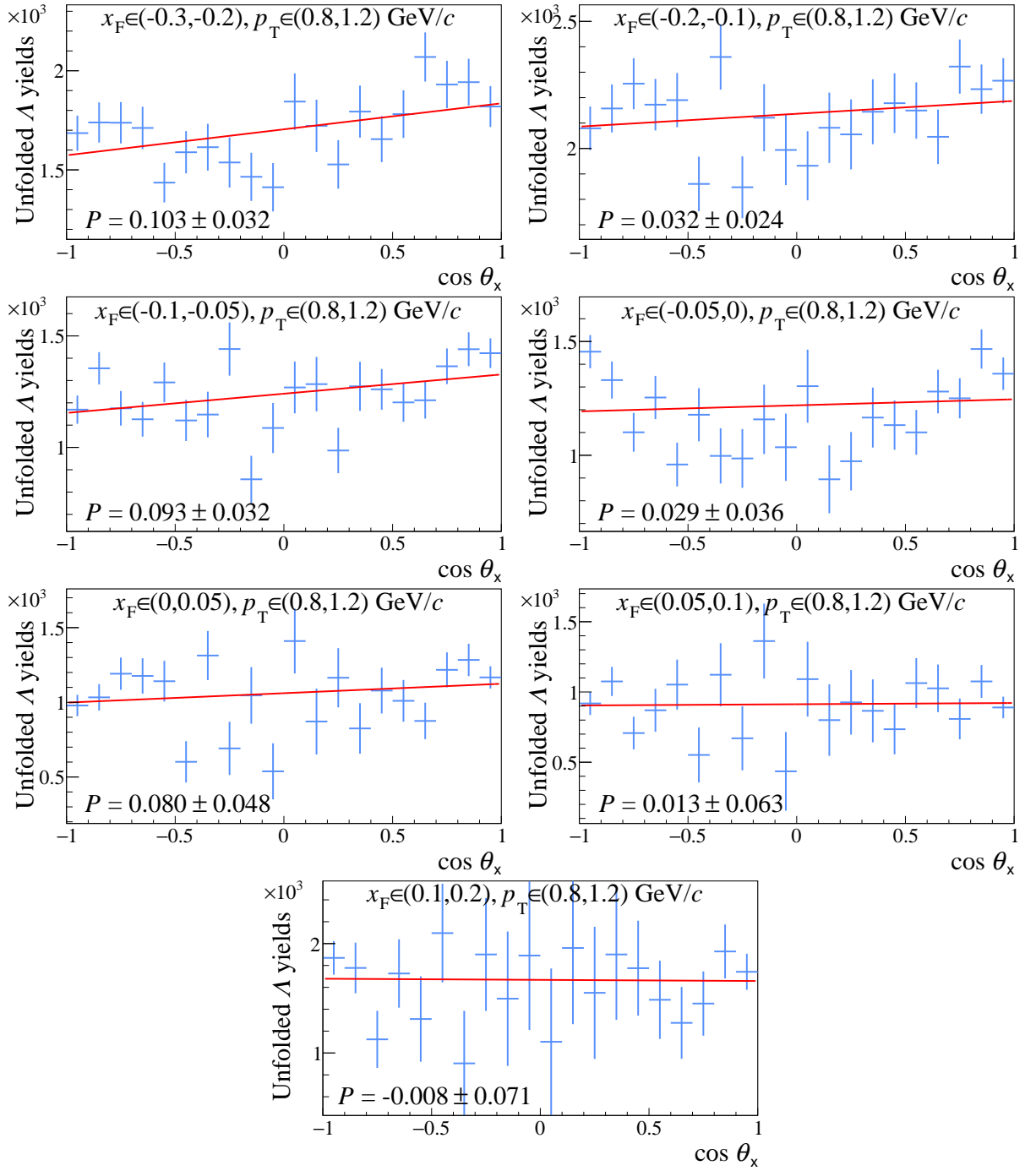
Figure 6.2: The $\cos\theta_x$ distributions of Λ hyperons unfolded yields in different x_F bins at $p_T \in (0.8, 1.2)$ GeV/c for data using EPOS MC dataset. The uncertainties shown here are propagated from statistical uncertainties in Λ yields within $\cos\theta_x$ bins (See Sec. 5.6).
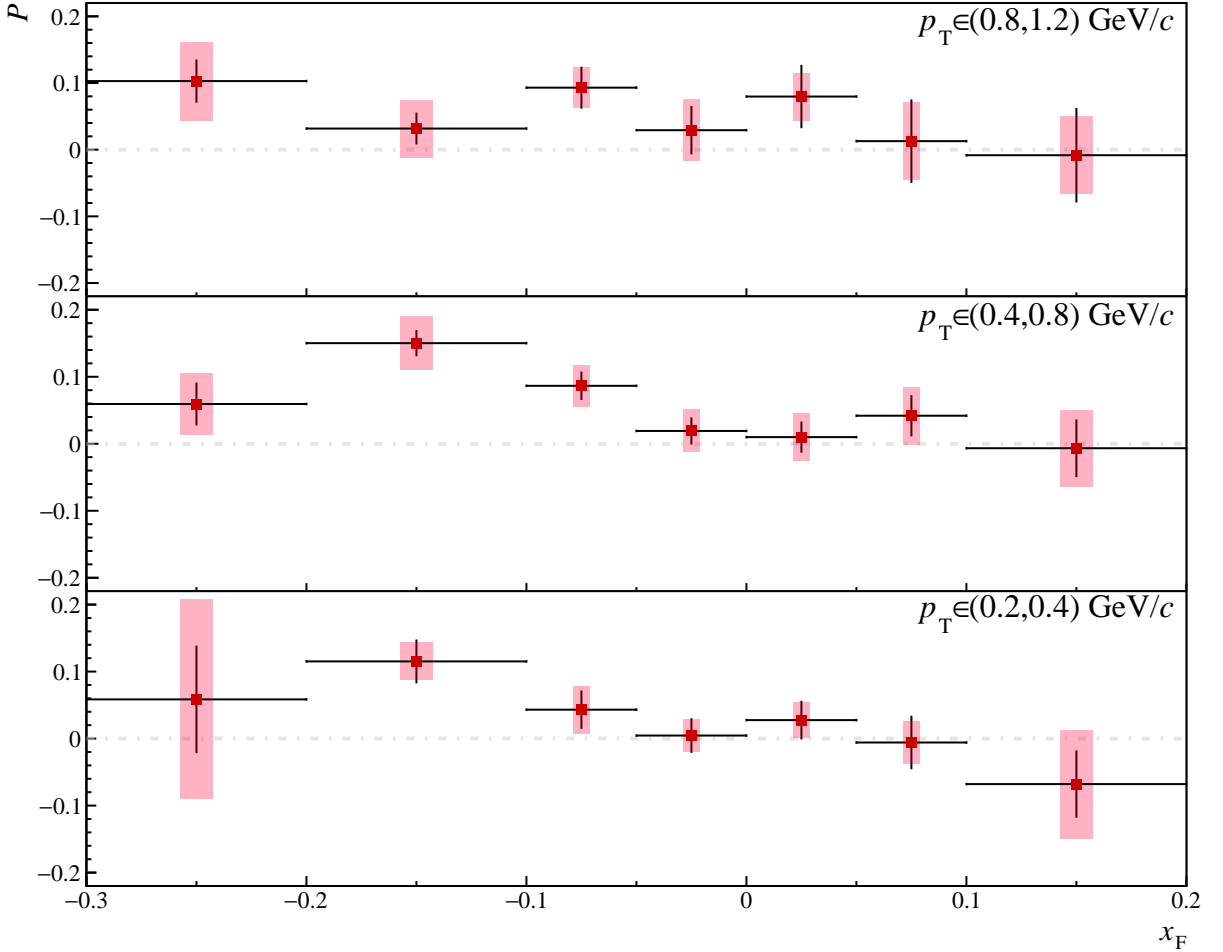
Figure 6.3: Measured Λ transverse polarization for different (x_F, p_T) bins; shaded bands represent systematic, and bars represent statistical uncertainties.

$p_T \in (0.4, 0.8)$ GeV/c, and in backward hemisphere at $p_T \in (0.8, 1.2)$ GeV/c.

The contributions to systematic uncertainty are calculated as defined in Sec. 5.7 and are shown in Fig. 6.6. The numerical values are presented in Table D.1 in Appendix D. The analysis of systematic uncertainties, detailed in Sec. 5.7, identified specific contributions to the total uncertainty. The VTPC clusters cut was found to be a crucial factor, representing a significant contribution away from midrapidity for Λ hyperons with low transverse momentum. In some specific bins (e.g., $x_F \in (-0.3, -0.2)$, $p_T \in (0.2, 0.4)$ GeV/c), it is the most significant single contribution to the systematic uncertainty. This highlights the sensitivity of the results in this region to the track reconstruction efficiency in the Vertex Time Projection Chambers. For the backward hemisphere ($x_F < 0$), the choice of the specific Monte Carlo model used (EPOS or FTFP) for the response matrix and efficiency corrections is the primary contributor to the systematic uncertainty. For the forward hemisphere ($x_F > 0$), the choice of the unfolding method is a significant contributor to the systematic uncertainty, often being the largest component. The systematic uncertainties originating from the event and track cuts, and m_{inv} fitting are mainly below 0.01–0.02 (with a few exceptions), following a trend of being lower around midrapidity and rising away from midrapidity. The contributions from the event cuts (*WFA cut* and *Primary*
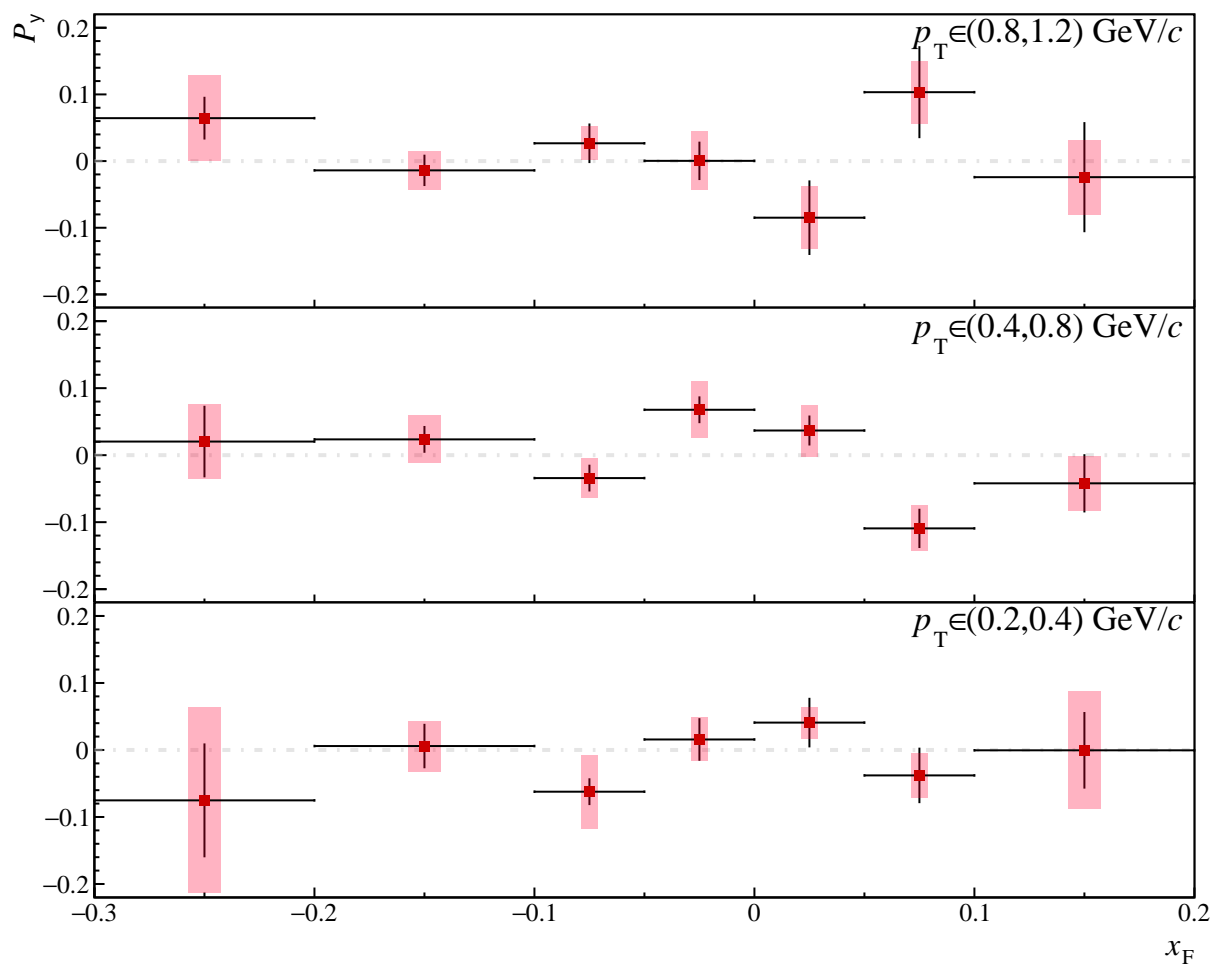
Figure 6.4: Measured P_y component of Λ transverse polarization for different (x_F, p_T) bins, shaded bands are systematic, and bars are statistical uncertainties.
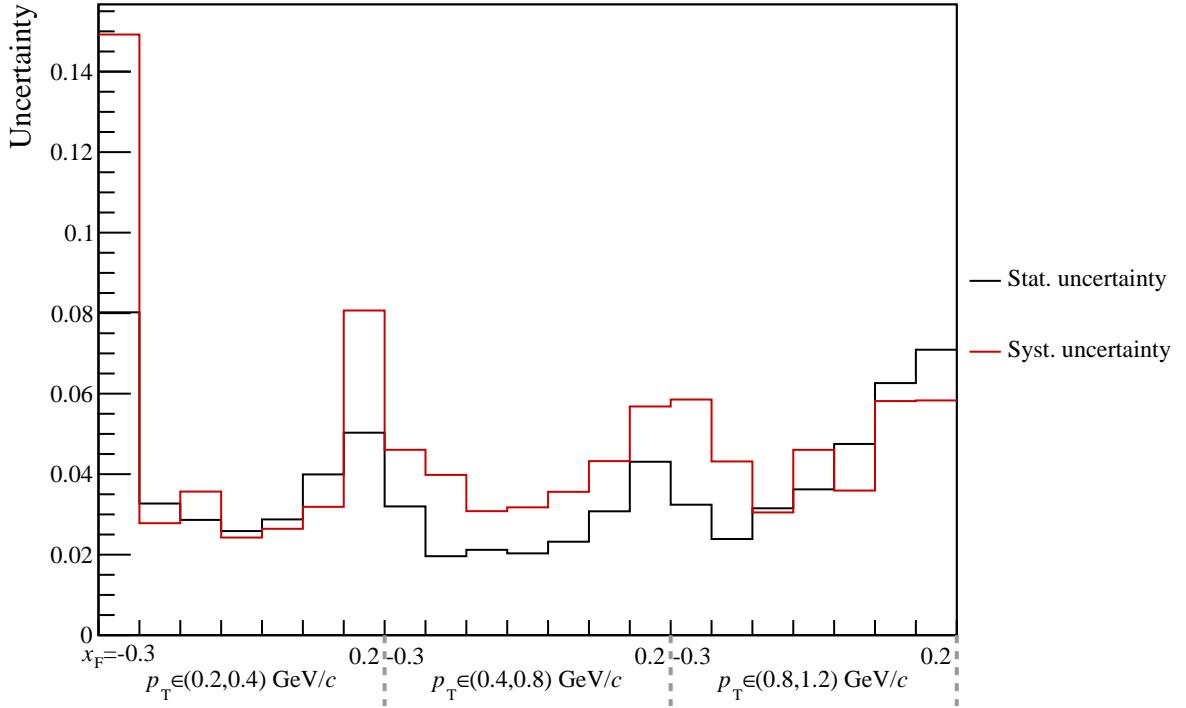
Figure 6.5: The statistical and systematic uncertainties of the measured Λ transverse polarization, as defined in Sec. 5.7.

Vertex z cut) are among the lowest ones.

The systematic uncertainties associated with the *MC model* and the specific *unfolding method* are both evaluated using Monte Carlo simulations. Consequently, the precision of these systematic estimates is inherently limited by the statistical uncertainty of the MC samples. While these two sources of systematic uncertainty are treated as distinct contributions to the total uncertainty, their evaluation can be made more precise by increasing the size of the corresponding MC datasets, thereby reducing the propagated statistical component. We assume that differences of distributions from two models fairly represent or overestimate the differences between EPOS MC (used for unfolding) and experimental data.

In summary, the unfolding method provided the primary polarization for this analysis. While the statistical and systematic uncertainties are comparable, limiting the precision, the results in the forward x_F region show deviations from the negative polarization trend known from the world data parametrization (see Sec. 2.3.3, Fig. 2.6 (*left*)). The systematic uncertainties vary across the kinematic plane, with specific detector effects dominating in the backward hemisphere and the details of the analysis technique (unfolding and MC model dependence) being more critical in the forward hemisphere.
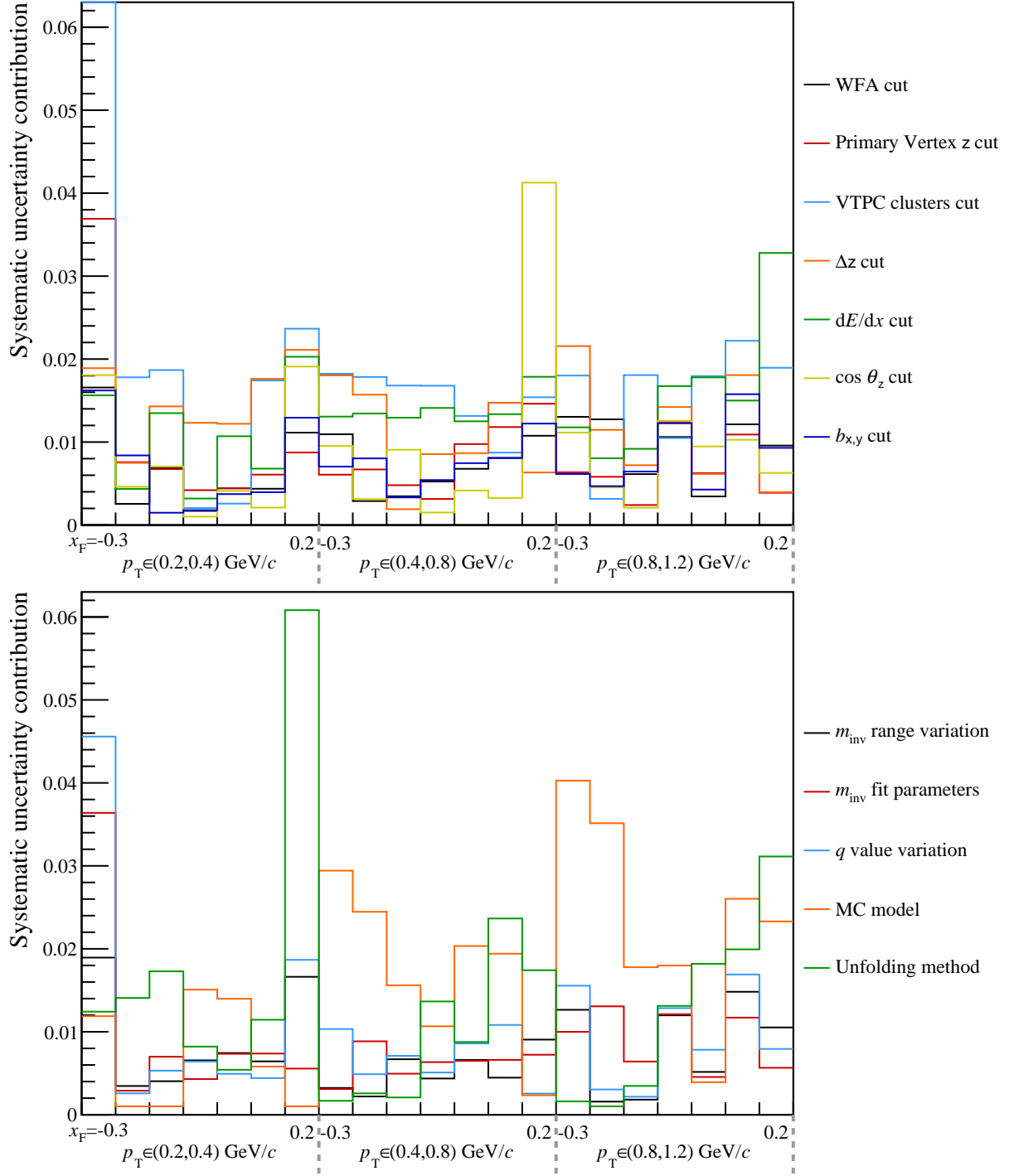
Figure 6.6: Contributions from each cut variation to the systematic uncertainty of the measured Λ transverse polarization (*top*: from event and track cuts, *bottom*: from m_{inv} fitting and MC correction procedures), as defined in Sec. 5.7. The bin $x_F \in (-0.3, -0.2)$, $p_T \in (0.2, 0.4)$ GeV/c has large contribution from *VTPC clusters cut* value 0.124 and is not shown.

6.1 Comparison with world data and model

The measured polarization results from NA61/SHINE are compared with the DeGrand-Miettinen model [52] and the world data parametrization [46][1] in Fig. 6.7, and reveal minor discrepancies in specific kinematic regions. Notably, the measured polarization exceeds model predictions, however the deviation remains within two standard deviations, in the four (x_F, p_T) bins ($x_F \in (0, 0.05)$ $p_T \in (0.8, 1.2)$ GeV, $x_F \in (-0.2, -0.1)$ $p_T \in (0.4, 0.8)$ GeV, $x_F \in (-0.1, -0.05)$ $p_T \in (0.4, 0.8)$ GeV, $x_F \in (-0.2, -0.1)$ $p_T \in (0.2, 0.4)$ GeV). The measured Λ transverse polarization is shown in the figure with total uncertainty as a sum of statistical and systematic uncertainties in quadrature.
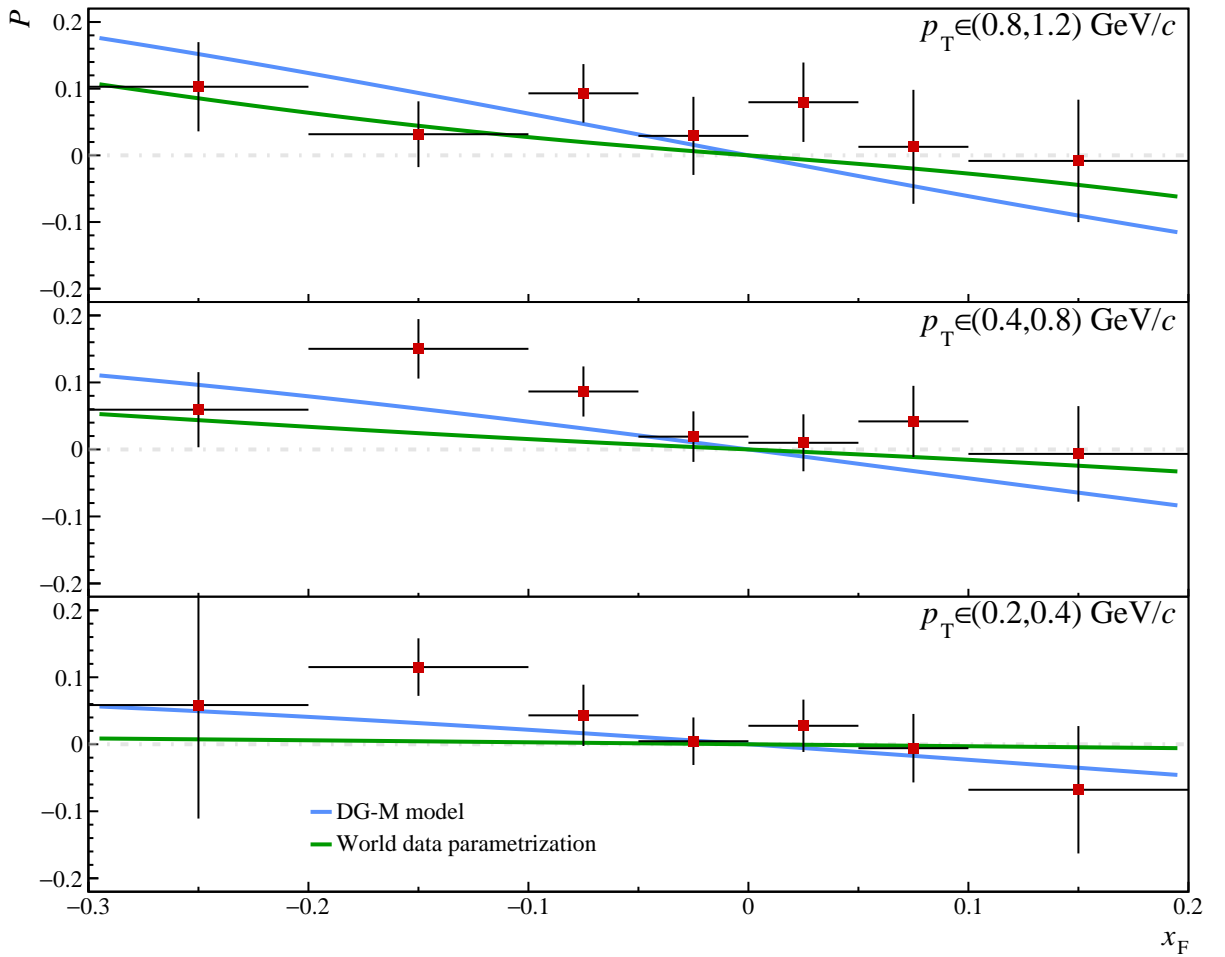
Figure 6.7: Measured Λ transverse polarization for different (x_F, p_T) bins, with error bars representing total uncertainties. The results are compared with the DeGrand-Miettinen model [52] (*blue line*) and world data parametrization [46] (*green line*) at $p_T = 1$ GeV/c (*top*), $p_T = 0.6$ GeV/c (*middle*), and $p_T = 0.3$ GeV/c (*bottom*) (see Sec. 2.3.3). See text for details.

The measured polarization results from NA61/SHINE at $p_T \in (0.8, 1.2)$ GeV/c are compared with the world experimental data, the DeGrand-Miettinen model, and the world data parametriza-

---

[1]It is important to note that the world data parametrization is based on a phenomenological fit published in 2001; therefore, it does not incorporate experimental results that became available after that date.
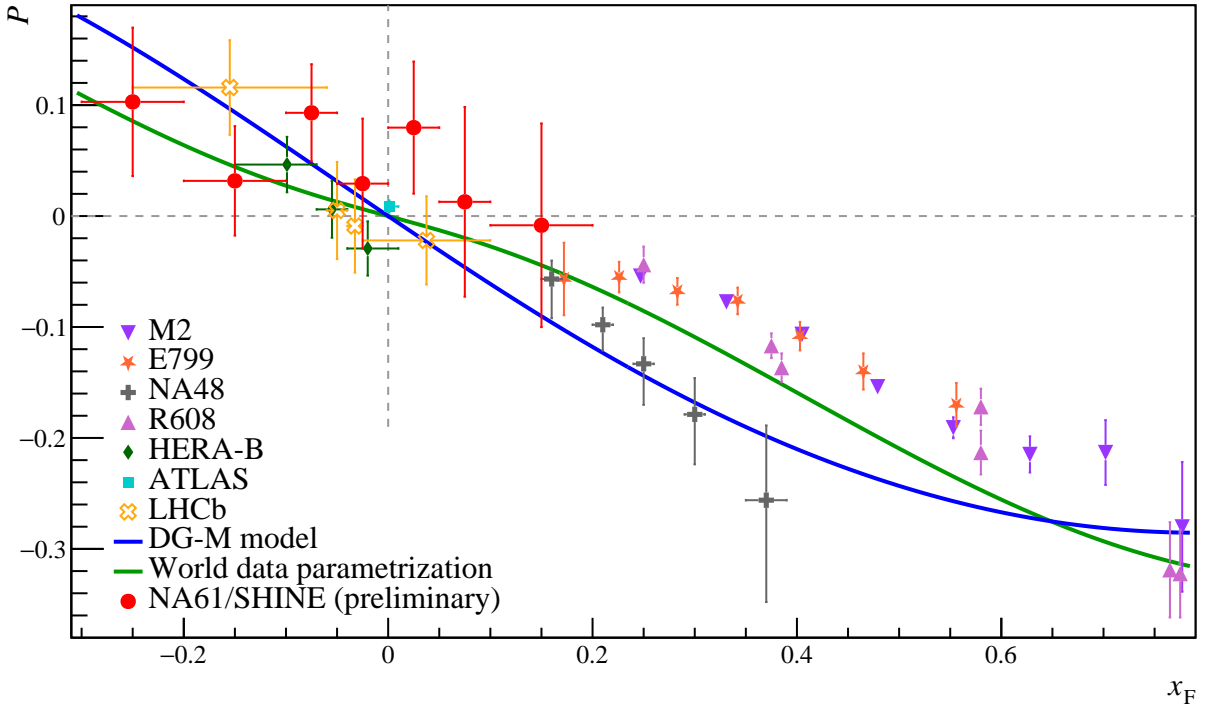
Figure 6.8: Comparison of the NA61/SHINE results on Λ hyperon transverse polarization at $p_{\mathrm{T}} \in (0.8, 1.2)$ GeV/c with the DeGrand-Miettinen model [52] (*blue line*) and the world data parametrization [46] (*green line*) at $p_{\mathrm{T}} = 1$ GeV/c. The shown uncertainties are the sum of statistical and systematic uncertainties added in quadrature. Several data points from R608 experiments were shifted horizontally for better visibility.

tion in Fig. 6.8. The comparison spans a wide range of experimental conditions: p+p collisions at $\sqrt{s} = 7$ TeV from ATLAS [14], proton-Neon collisions at $\sqrt{s} = 68$ GeV from LHCb [23], HERA-B fixed-target carbon (C) and tungsten (W) at $\sqrt{s_{NN}} = 41.6$ GeV, Fermilab fixed-target experiments (M2 [18], E799 [17]) along with CERN's NA48 [16] using proton-Beryllium collisions at $\sqrt{s_{NN}} = 27-39$ GeV and R608 [157]. A direct comparison requires careful consideration of differing experimental conditions and kinematic coverage. The polarization of Λ hyperons has been shown to depend weakly on the atomic mass of the target nucleus (see also Sec. 2.3.2), which allows for a direct comparison between experiments using different light targets, such as the liquid hydrogen target in NA61/SHINE and the beryllium (^{9}Be) or carbon (C) targets used in other fixed-target experiments. For a meaningful comparison, the Feynman-x (x_{F}) values from the E799 and NA48 experiments [16, 17] are adjusted to the center-of-mass frame definition used in this analysis, although the numerical difference is negligible. All data points (except LHCb) were multiplied by $\alpha^{\mathrm{old}}/\alpha^{\mathrm{current}} = 0.642/0.747$ to account for the old (known up to 2018) value of the Λ hyperon parity-violating weak decay asymmetry $\alpha^{\mathrm{old}} = 0.642$ [158][2].

The fixed-target experiments at Fermilab (M2, E799) and CERN (NA48) established the fundamental kinematic dependencies of Λ polarization. The M2 experiment, using a 400 GeV/c proton beam on a Be target, provided a detailed map over the ranges $0.2 < x_{\mathrm{F}} < 0.8$ and $0.6 < p_{\mathrm{T}} < 3.8$ GeV/c using a total of 7×10^6 $\Lambda \rightarrow p\pi^-$ reconstructed. It demonstrated that the

---

[2]Resulting in $P = (\alpha^{\mathrm{old}}P^{\mathrm{old}})/\alpha^{\mathrm{current}}$ polarization value shown.

polarization magnitude monotonically increases with p_T up to a plateau around $p_T \approx 1$ GeV/c, and that the magnitude of this plateau increases with x_F [2, 18]. Total uncertainty was reported without separating statistical and systematic contributions, with Monte Carlo acceptance correction identified as the primary contributor to the systematic bias. The NA48 experiment, with a 450 GeV/c proton beam on Be, measured polarization from $P(x_F = 0.16) = -0.046 \pm 0.029$ to $P(x_F = 0.37) = -0.256 \pm 0.064$ for a transverse momentum range of $0.3 < p_T < 1$ GeV/c. Notably, the NA48 results exhibit a higher magnitude of polarization value at lower x_F, despite probing a lower mean p_T range $(0.36 - 0.86$ GeV) compared to the higher-momentum regions of the E799 $(0.67 - 2.15$ GeV) and M2 $(0.62 - 1.69$ GeV) experiments.

The HERA-B and LHCb experiments extended these measurements into the negative x_F region. Using the 920 GeV/c proton beam on C and W targets $(\sqrt{s} = 41.6$ GeV), HERA-B found a polarization of $P = 0.046 \pm 0.016(\text{stat}) \pm 0.019(\text{syst})$ in the bin $-0.15 < x_F < -0.07$. Similarly, the LHCb measurement was done in p+Ne collisions at $\sqrt{s_{NN}} = 68.4$ GeV (2.5 TeV proton beam) with an integrated luminosity of 24.9 nb^{-1} (order of 10^9 inelastic collision events recorded). They found a polarization of $P = 0.116 \pm 0.040(\text{stat}) \pm 0.015(\text{syst})$ in the bin $-0.25 < x_F < -0.06$, $0.3 < p_T < 3$ GeV/c. The systematic contributions were found to be small, and statistical uncertainties dominated the measurement.

The NA61/SHINE polarization values in the backward hemisphere are lower, namely $P = 0.032 \pm 0.024 \pm 0.043$ at negative $x_F \in (-0.2, -0.1)$, and $P = -0.008 \pm 0.071 \pm 0.058$ at positive $x_F \in (0.1, 0.2)$. However, within large uncertainties, they agree with results from other experiments. The NA61/SHINE results at $\sqrt{s_{NN}} = 17.3$ GeV are consistent with this established trend of weak energy dependence and follow the general increase in the magnitude of the polarization with x_F.

At much higher energies, the ATLAS experiment measured Λ polarization in proton-proton collisions at $\sqrt{s} = 7$ TeV. In the kinematic range accessible to ATLAS, characterized by a very low $|x_F| < 0.01$, the measured polarization was found to be consistent with zero, specifically $P = -0.009 \pm 0.004(\text{stat}) \pm 0.003(\text{syst})$ integrated over $p_T = 0.8 - 15$ GeV. This result is consistent with NA61/SHINE data and the extrapolation from lower-energy data, which predicts that the polarization should vanish as $x_F \to 0$.

This comprehensive comparison bridges measurements across energy regimes from fixed-target to LHC energies while accounting for definitional and systematic differences between experiments. The tabulated data from these experiments as shown in Fig. 6.8 can be found in Tables D.4–D.8.

Chapter 7

Summary and Outlook

This thesis presents pioneering investigations of Λ hyperon transverse polarization in proton-proton interactions at the beam momentum of 158 GeV/c ($\sqrt{s_{NN}}$ = 17.3 GeV), recorded by the NA61/SHINE experiment at the CERN SPS as part of its main physics program – the two-dimensional scan in the beam momentum and the system size.

In the analysis, Λ hyperons are identified through their dominant weak decay channel $\Lambda \rightarrow p\pi^-$ in selected inelastic $p+p$ events. The reconstruction of Λ candidates is performed by analyzing the invariant mass distribution of selected proton-pion pairs, where the signal peak is described by a q-Gaussian profile that accounts for detector resolution effects. The combinatorial background is parameterized using a second-order Chebyshev polynomial.

The unfolding method was employed as the primary technique for correcting the measured angular distributions of the Λ decay products in the three-dimensional space of ($x_{\mathrm{F}}, p_{\mathrm{T}}, \cos\theta_{\mathrm{x}}$). It corrects the measured $\cos\theta_{\mathrm{x}}$ distributions for the effects of detector acceptance and reconstruction efficiency, yielding distributions that more closely reflect the actual kinematics of the produced particles. This correction was determined using detailed Monte Carlo simulations based on GEANT4 and the EPOS-1.99 model.

The unfolded $\cos\theta_{\mathrm{x}}$ distributions were then fitted to extract the polarization values and their statistical uncertainties. The systematic uncertainties associated with this measurement were calculated by varying event and track selection cuts, as well as aspects of the fitting and unfolding procedure. They were added in quadrature to obtain the total systematic uncertainty. The effect of Λ precession in the magnetic field was studied in Sec. 5.8. It was found to be negligible and, therefore, is not included in the total systematic uncertainty.

The key results of this thesis are transverse polarization values in the kinematical region of the Λ $x_{\mathrm{F}} \in (-0.3, 0.2)$ and $p_{\mathrm{T}} \in (0.2, 1.2)$ GeV/c presented in Chapter 6. The measured polarization values are consistent with zero within experimental uncertainties at midrapidity ($x_{\mathrm{F}} \approx 0$) as expected from the forward-backward symmetry of $p+p$ collisions. These results are considered preliminary by the NA61/SHINE collaboration. The polarization measurements obtained in this work, along with their systematic comparison to existing experimental data, are presented in Sec. 6.1. Measured transverse polarization is consistent with other experiments and models. However, the accuracy of the current measurement does not resolve the tensions between the results of previous experiments. Given this limitation, extending such measurements to nucleus-nucleus collisions recorded by the NA61/SHINE experiment may not provide substantial additional insights.

Following the installation of the Vertex Detector close to the target during Long Shutdown 2 in 2020 [159], the invariant mass resolution at midrapidity has improved markedly: the Λ

peak width has been reduced to approximately 0.7 MeV, compared to 3 MeV as obtained in this analysis. Such improvement is expected to substantially lower systematic uncertainties in the measurement of Λ transverse polarization.

Furthermore, NA61/SHINE plans to record $p+p$ interactions at 300 GeV/c in 2025 [160], collecting about 600M events – approximately ten times more than the current dataset. This increase in statistics can reduce the statistical uncertainty of Λ polarization analysis by a factor of $\sqrt{10} \approx 3$. Both the method and software[1] developed for this thesis will be used for the analysis of the new data.

The discussed results, along with projected uncertainties for future measurements in 2025, are shown in Fig. 7.1. Compared to the results discussed in Chapter 6, the statistical uncertainties
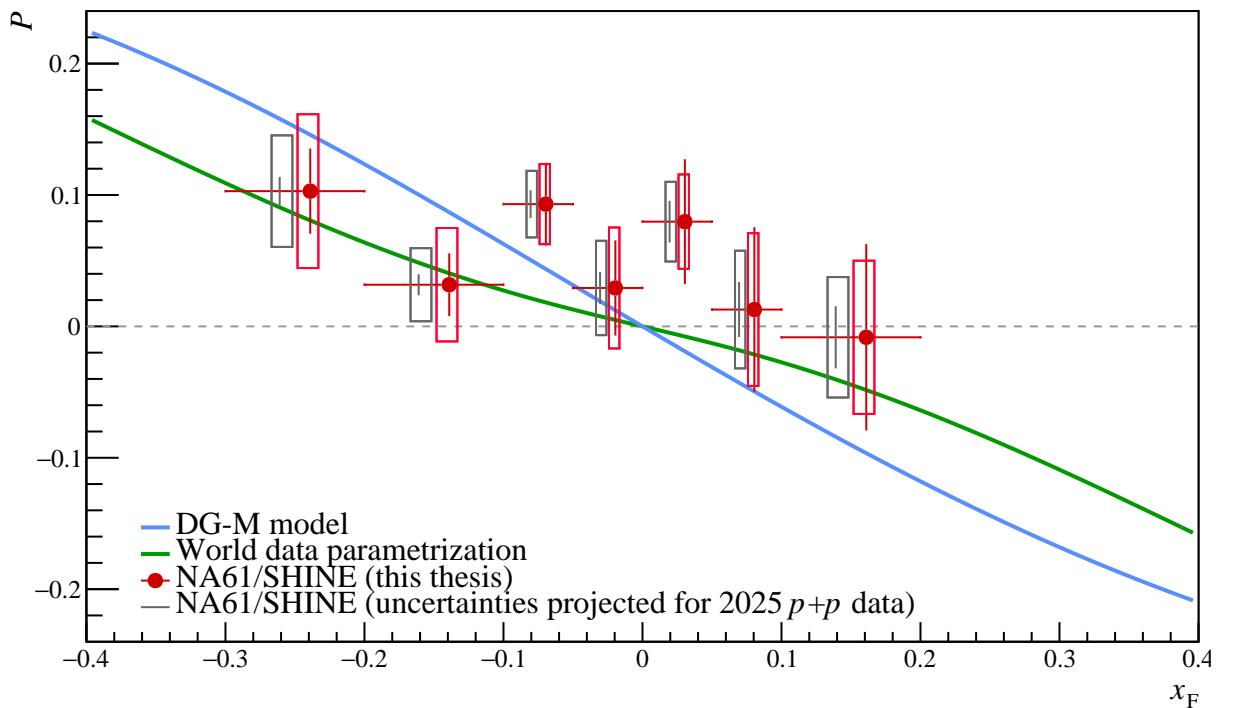
Figure 7.1: Comparison the NA61/SHINE results on Λ hyperon transverse polarization at $p_T \in (0.8, 1.2)$ GeV/c measured in this thesis (*red circle*) with projected statistical (error bars) and systematic (boxes) uncertainties (*grey*) with the DeGrand-Miettinen model [52] (*blue line*) and world data parametrization [46] (*green line*) at $p_T = 1$ GeV/c.

are reduced threefold. The selected contributions to the systematic uncertainties were reduced twofold by the following considerations:

- *Target position cut* due to improved precision in primary vertex reconstruction,
- *m_{inv} range variation*, *m_{inv} fit parameters*, *q value variation* due to improved background rejection,
- *MC model* and *Unfolding* due to the expected larger ratio of the MC dataset size to data size.

---

[1]Available at `https://gitlab.cern.ch/na61-software/analysis/lambdapolarization.pp158` and `https://gitlab.cern.ch/yebondar/lambdapolarization.pp158`.

The resulting expected statistical uncertainty is around 0.01–0.02, and the systematic uncertainty is around 0.02–0.04. The expected results, shown in Fig. 7.1, will significantly increase the impact of the NA61/SHINE results on the understanding of Λ polarization in $p+p$ interactions.

Appendix A

Theoretical Background: Kinematics, Standard Model, and QCD

A.1 Kinematic variables

Four-vectors

In special relativity, the notion of a four-vector provides a natural and consistent framework for describing physical quantities that are invariant under Lorentz transformations. A four-vector is an object with four components that transforms linearly under Lorentz transformations, preserving the Minkowski metric.

A typical example of a four-vector is the *four-position*, defined as

$$x^\mu = (ct, \vec{r}) = (ct, \mathsf{x}, \mathsf{y}, \mathsf{z}), \tag{A.1}$$

where c is the speed of light, t is the time coordinate, and $\vec{r}$ represents the spatial coordinates. Another important example is the *four-momentum*,

$$p^\mu = (E/c, \vec{p}), \tag{A.2}$$

where E is the total energy and $\vec{p}$ is the three-momentum of a particle. A four-velocity vector is defined as $u^\mu = p^\mu/m$.

The scalar product of two four-vectors a^μ and b^μ is defined using the Minkowski metric tensor $\eta_{\mu\nu}$ as

$$a \cdot b = \eta_{\mu\nu} a^\mu b^\nu = a^0 b^0 - \vec{a} \cdot \vec{b}, \tag{A.3}$$

where the sign convention $(+, -, -, -)$ is used. This scalar product is invariant under Lorentz transformations. Here and throughout the thesis, we adopt the **Einstein summation convention**, whereby repeated indices (once as an upper index and once as a lower index) represented by Greek letters imply an implicit sum over all values of that index. For example, in the expression above, a summation over $\mu, \nu = 0, 1, 2, 3$ is implied.

Lorentz transformations relate the coordinates of an event in one inertial frame to those in another frame moving at a constant velocity relative to the first. For a boost along the z-axis with

velocity v, the Lorentz transformation is given by

$$\begin{pmatrix} ct' \\ z' \end{pmatrix} = \begin{pmatrix} \gamma & -\beta\gamma \\ -\beta\gamma & \gamma \end{pmatrix} \begin{pmatrix} ct \\ z \end{pmatrix}, \tag{A.4}$$

where $\beta = v/c$ and $\gamma = 1/\sqrt{1 - \beta^2}$ is the Lorentz factor.

Four-vectors transform according to

$$a'^\mu = \Lambda^\mu{}_\nu a^\nu, \tag{A.5}$$

where $\Lambda^\mu{}_\nu$ is the Lorentz transformation matrix. Due to the linearity of Lorentz transformations, the scalar product and thus physical quantities such as the invariant mass m of a particle, given by

$$m^2 c^2 = p^\mu p_\mu = \left(\frac{E}{c}\right)^2 - \vec{p}^2, \tag{A.6}$$

remain the same in all inertial frames.

Center-of-mass energy and transverse momentum

In the analysis of particle collisions, two key kinematic variables are the center-of-mass energy and the transverse momentum.

The center-of-mass energy, denoted by $\sqrt{s}$, represents the total energy available in the center-of-mass frame of the colliding particles. For a two-particle collision involving particles with four-momenta p_1 and p_2, it is defined as the invariant mass of the system:

$$\sqrt{s} = \sqrt{(p_1 + p_2)^2} = \sqrt{(E_1 + E_2)^2 - (\vec{p}_1 + \vec{p}_2)^2 c^2}. \tag{A.7}$$

This quantity is Lorentz invariant and determines the maximum possible mass of particles that can be created in the collision. For collisions involving nuclei, the energy is often expressed per nucleon pair, denoted as $\sqrt{s_{NN}}$.

The momentum of a produced particle, $\vec{p}$, can be decomposed into a component parallel to the beam axis (p_z) and a component perpendicular to it. The transverse momentum, denoted by p_T, is the magnitude of this perpendicular component:

$$p_T = \sqrt{p_x^2 + p_y^2}, \tag{A.8}$$

where the beam is assumed to travel along the z-axis. The transverse momentum is a crucial variable as it is invariant under Lorentz boosts along the beam direction.

Rapidity and Feynman variable

Rapidity (y) is a dimensionless variable used to describe the longitudinal motion of particles along the beam axis. It is defined as:

$$y = \frac{1}{2} \ln \left(\frac{E + p_z}{E - p_z} \right), \tag{A.9}$$

where E is the energy of the particle and p_z is its momentum along the selected direction (usually beam direction). Rapidity is particularly useful because it transforms additively under Lorentz boosts along the beam axis, making it a convenient variable for analyzing relativistic collisions.

Feynman variable x_F is defined originally in [161] as a dimensionless variable to study scaling behavior in particle production:

$$x_F = \frac{p_z^*}{p_{max}^*}, \tag{A.10}$$

where p_z^* is the longitudinal momentum of a produced particle in the center of mass system (CMS) and p_{max}^* is the maximum possible longitudinal momentum. It is usually selected as beam momenta in CMS $p_{max}^* = p_{beam}^* \approx \sqrt{s_{NN}}/2$ in the ultra-relativistic approximation.

In this thesis, $p_{beam} = 158$ GeV/c in lab frame and $\sqrt{s_{NN}} = 17.27$ GeV/c, and in the center of mass frame $p_{beam}^* = 8.5839$ GeV/c differs by 0.6% from $\sqrt{s_{NN}}/2 = 8.635$ GeV/c.

The *midrapidity* is the kinematic region where the rapidity of the particle in the center of mass of the collision is close to zero, *i.e.*, $y \approx x_F \approx 0$. Regions with positive ($x_F > 0$) and negative ($x_F < 0$) Feynman-x variable (or rapidity) are referred to as *forward* and *backward* regions, respectively.

Armenteros-Podolanski variables

The Armenteros-Podolanski variables [134] are used to analyze the kinematics of decays involving neutral particles that decay into two charged particles, such as $K_S^0 \rightarrow \pi^+ \pi^-$ or $\Lambda \rightarrow p \pi^-$. These variables are particularly useful for separating the signal from the background and for studying the properties of the decaying particle. The two key variables are:

- α variable describes the asymmetry in the longitudinal momentum of the two decay products. It is defined as:

$$\alpha = \frac{p_L^+ - p_L^-}{p_L^+ + p_L^-}, \tag{A.11}$$

where $p_L^\pm$ are the longitudinal momenta of the two charged decay products with respect to the direction of the reconstructed V^0 momentum (see Fig. A.1). The variable α ranges from -1 to $+1$ and is sensitive to the difference between positive and negative track kinematics.

- p_T^{AP} variable describes the transverse momentum of the decay products relative to the direction of the parent particle. It is defined as:

$$p_T^{AP} = p_T^+ = p_T^-, \tag{A.12}$$
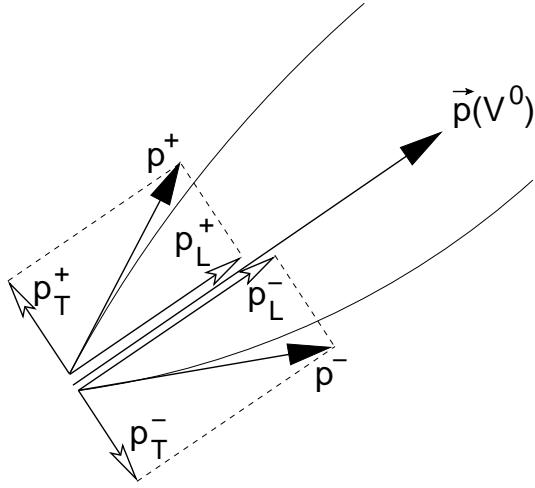
Figure A.1: Transverse $p_T^\pm$ and longitudinal $p_L^\pm$ momentum components of the positively and negatively-charged track, with respect to the direction of the reconstructed V^0 momentum $\vec{p}(V^0)$. Figure from [49].

where $p_T^\pm$ are the transverse momenta of the two charged decay products.

In the ultra-relativistic approximation, these two variables lie on an ellipse:

$$\frac{(\alpha - \alpha_0)^2}{r_\alpha^2} + \frac{(p_T^{AP})^2}{p^{*2}} = 1 \,, \tag{A.13}$$

where parameters of this ellipsis are functions only of the masses of decayed particle M and daughter particles $m^\pm$:

$$\alpha_0 = \frac{(m^+)^2 - (m^-)^2}{M^2} \,, \quad r_\alpha = \frac{2p^*}{M} \,, \quad p^{*2} = \frac{\left(M^2 - (m^+ + m^-)^2\right)\left(M^2 - (m^+ - m^-)^2\right)}{4M^2} \,. \tag{A.14}$$

For $K_S^0 \to \pi^+\pi^-$ and $\Lambda \to p\pi^-$ decays in particular,

$$K_S^0 \to \pi^+\pi^- : \alpha_0 = 0 \,, \quad p^* = 0.21 \text{ GeV}/c \,, \quad r_\alpha = 0.83 \,. \tag{A.15}$$

$$\Lambda \to p\pi^- : \alpha_0 = 0.69 \,, \quad p^* = 0.1 \text{ GeV}/c \,, \quad r_\alpha = 0.18 \,. \tag{A.16}$$

A.2 The Standard Model of particle physics

The Standard Model (SM) is a quantum field theory that encapsulates our current understanding of the fundamental constituents of matter and the interactions among them [12, Ch. 9-13].

The SM describes three of the four known fundamental forces in nature: the electromagnetic force, the weak nuclear force, and the strong nuclear force. The fourth force, gravity, is described by General Relativity and remains outside the scope of the Standard Model. The SM is a gauge theory built upon the local symmetry group

$$SU(3) \otimes SU(2) \otimes U(1) \,,$$

where $SU(3)$ corresponds to the strong interaction (Quantum Chromodynamics), and $SU(2) \otimes U(1)$ describes the unified electroweak interaction.

The symmetries present in the SM Lagrangian give rise to conserved quantities, as dictated by Noether's theorem. These symmetries remain invariant under space-time translations, rotations, and Lorentz boosts. The Standard Model includes three types of fundamental fields: spin-1 gauge bosons, spin-1/2 fermions (which constitute matter), and a scalar spin-0 field – the Higgs boson. The Higgs field is responsible for mass generation via spontaneous symmetry breaking, where its coupling to other particles is proportional to their masses.

The gauge bosons mediating the fundamental forces include the photon (γ), $W^{\pm}$ and Z^0 bosons, and gluons (g). Quantum Electrodynamics (QED), based on the $U(1)$ gauge group, governs the electromagnetic interactions between charged fermions via photon exchange. The electroweak theory, unifying electromagnetic and weak interactions, arises from the $SU(2) \otimes U(1)$ symmetry and is mediated by the $W^{\pm}$ and Z^0 bosons. The strong interaction, responsible for binding quarks within nucleons and nucleons within nuclei, is described by Quantum Chromodynamics, which is based on the $SU(3)$ symmetry. QCD introduces a color charge and involves eight gluons due to the theory's eightfold symmetry. A more detailed discussion of QCD is provided below.

Each interaction has an associated coupling constant characterizing its relative strength:

$$\alpha_s \sim 1\,, \quad \alpha_{\text{em}} \sim \frac{1}{137}\,, \quad \alpha_w \sim 10^{-7}\,, \tag{A.17}$$

where α_s, α_{em}, and α_w represent the coupling constants for the strong, electromagnetic, and weak interactions, respectively.

The spin-1/2 fermions in the SM are divided into two categories: leptons and quarks. Leptons carry electroweak charges but no color charge and thus do not participate in strong interactions. The charged leptons include the electron (e), muon (μ), and tau (τ), each with electric charge -1, along with their corresponding neutral neutrinos (ν_e, ν_μ, ν_τ).

Quarks, in contrast, carry both electroweak and color charges and, therefore, interact via all three fundamental forces described by the SM. There are six quark flavors: up (u), down (d), charm (c), strange (s), top (t), and bottom (or beauty, b). The u, c, and t quarks carry a fractional electric charge of $+\frac{2}{3}$, while the d, s, and b quarks have a charge of $-\frac{1}{3}$. Each fermion has a corresponding anti-fermion with opposite quantum numbers.

A.2.1 Quantum chromodynamics

Quantum chromodynamics (QCD) is the quantum field theory that describes the strong nuclear force, which is responsible for binding quarks and gluons into protons, neutrons, and ultimately the visible matter in the universe. Particles that interact via QCD carry a property known as *color charge*, analogous to electric charge in Quantum Electrodynamics (QED). There are three color charges – red, green, and blue – each with a corresponding anticolor. Color-neutral (or "white") bound states are formed either by combining all three colors or a color with its anticolor.

The QCD Lagrangian is given by:

$$\mathcal{L}_{\text{QCD}} = \sum_{q=1}^{n_f} \bar{\psi}_q(x)(i\slashed{D} - m_q)\psi_q(x) - \frac{1}{4}F_{\mu\nu}^a(x)F^{a\mu\nu}(x),\qquad\text{(A.18)}$$

where ψ_q are the quark fields for $n_f = 6$ quark flavors with mass m_q, and $\slashed{D} = \gamma^\mu D_\mu$ is the Feynman slash notation for the covariant derivative. The covariant derivative is defined as $D_\mu = \partial_\mu - ig\sum_a A_\mu^a T^a$, where g is the QCD coupling constant, A_μ^a represents the gluon field with $a = 1,\dots,N_c^2 - 1$ ($N_c = 3$ is the number of colors), and T^a are the generators of the SU(3) color group (*i.e.*, Gell-Mann matrices).

The gluon field strength tensor is given by:

$$F_{\mu\nu}^a = \partial_\mu A_\nu^a - \partial_\nu A_\mu^a + gf^{abc}A_\mu^b A_\nu^c,\qquad\text{(A.19)}$$

where f^{abc} are the SU(3) structure constants. The last term in $F_{\mu\nu}^a$ signifies the non-Abelian nature of QCD: gluons carry color charge and can, therefore, interact with one another, leading to both three-gluon and four-gluon vertices. This contrasts with QED, where photons are electrically neutral and do not self-interact.

An essential consequence of gluon self-interaction is the energy dependence of the strong coupling constant $\alpha_s = g^2/4\pi$. This coupling is not constant but varies with the energy scale Q of the interaction, a phenomenon known as the *running of the coupling constant*, governed by the renormalization group equations. Two notable features of QCD arise from this behavior:

- **Asymptotic Freedom**: At high energies (short distances), α_s becomes small, and quarks behave nearly as free particles [12, Ch. 9], a discovery awarded the Nobel Prize in 2004.
- **Confinement**: At low energies (large distances), α_s grows rapidly, causing quarks to be bound into color-neutral states (hadrons).

To resolve the internal partonic structure of the proton, high-energy probes with small wavelengths are required, where the resolution scale $Q \sim 1/\lambda$. In scattering processes beyond simple quark-quark interactions, higher-order corrections must be considered, influencing the behavior of α_s.

For momentum transfers $Q \gg \Lambda_{\text{QCD}}$, where $\Lambda_{\text{QCD}} \sim 200$ MeV, the coupling is sufficiently small for perturbative QCD (pQCD) to be applicable. In contrast, at low Q, the coupling becomes strong, and non-perturbative effects dominate. In this regime, color-charged particles are confined to hadrons, which are color-neutral bound states.

Hadrons are classified as:

- **Baryons**: States composed of three valence quarks (*e.g.*, qqq), with half-integer spin. Common examples include the proton (*uud*) and neutron (*udd*). The lightest strange baryon is the Λ baryon (*uds*).
- **Mesons**: States formed by a quark and an antiquark pair ($q\bar{q}$), with integer spin (*e.g.*, $J = 0$).

In addition to valence quarks, all hadrons contain sea quark-antiquark pairs and gluons. Understanding their internal dynamics, along with the quark-gluon interactions, is a complex problem that requires sophisticated techniques from both perturbative and non-perturbative QCD.

In high-energy collider experiments, such as those involving proton-proton or heavy-ion collisions, outgoing quarks or gluons rapidly hadronize into color-neutral particles. This process can result in collimated sprays of hadrons, known as *jets*. Accurately describing these phenomena requires a deep understanding of QCD across all energy scales.

Appendix B

Supplementary Material

B.1   Convergence criteria in MINUIT MIGRAD

The MINUIT MIGRAD algorithm [149], a quasi-Newton gradient-based minimizer, determines convergence to a local minimum by satisfying several conditions.

The Estimated Distance to Minimum (EDM) criterion ensures proximity to the minimum by requiring the predicted change in the objective function to be sufficiently small.

Mathematically, the EDM is defined as:

$$\text{EDM} = \mathbf{g}^{\mathrm{T}} \mathbf{V} \mathbf{g}, \tag{B.1}$$

where $\mathbf{g}$ is the gradient vector and $\mathbf{V}$ is the inverse Hessian (covariance) matrix of the objective function f. This would be exactly twice the vertical distance ($f - f_{\min}$) if the function were exactly quadratic with the covariance matrix $\mathbf{V}$. Since this estimate is only as good as the estimate of $\mathbf{V}$, an additional criterion is applied, namely that the successive estimates of $\mathbf{V}$ are not significantly different. The measure of difference used is (VTEST = the average fractional change in the diagonal elements of the $\mathbf{V}$). Convergence is achieved when:

$$\text{both} : \begin{cases} \text{EDM} < 10^{-1} \cdot \texttt{tol}, \\ \text{VTEST} < 0.01, \end{cases} \tag{B.2}$$
$$\text{or alone: EDM} < 10^{-6} * \texttt{tol},$$

where `tol` is a user-defined tolerance (default `tol = 1`).

These criteria guarantee that the solution is stable, the gradient is negligible, and further iterations would not significantly improve the fit. A valid positive-definite covariance matrix $\mathbf{V}$ is required for reliable convergence. If any criterion fails, MINUIT reports a non-convergence status.

B.2   Normalization of signal parametrization

For the asymmetric q-Gaussian function

$$S(m) = \mathcal{N} \left[1 + (q-1)\frac{(m-m_0)^2}{\Gamma^2/4} \right]^{-\frac{1}{q-1}}, \tag{B.3}$$

where Γ is Γ_L if $m < m_0$ and Γ_R otherwise for $1 < q \leq 3$, the normalization constant $\mathcal{N}$ in the range $m^{\text{low}} < m_0 < m^{\text{high}}$ computed with introducing auxiliary parameters

$$z^{\text{high}} = (q-1)\frac{(m^{\text{high}} - m_0)^2}{\Gamma_R^2/4}, \ z^{\text{low}} = (q-1)\frac{(m_0 - m^{\text{low}})^2}{\Gamma_L^2/4}, \tag{B.4}$$

as

$$\begin{aligned}
\mathcal{N}^{-1} &= \int_{m^{\text{low}}}^{m_0} \left[1 + (q-1)\frac{(m-m_0)^2}{\Gamma_L^2/4}\right]^{-\frac{1}{q-1}} dm + \\
&+ \int_{m_0}^{m^{\text{high}}} \left[1 + (q-1)\frac{(m-m_0)^2}{\Gamma_R^2/4}\right]^{-\frac{1}{q-1}} dm = \\
&= \frac{(m_0 - m^{\text{low}})}{\sqrt{1 + z^{\text{low}}}} \cdot {}_2F_1\left(\frac{1}{2}, \frac{3}{2} - \frac{1}{q-1}, \frac{3}{2}; \frac{z^{\text{low}}}{z^{\text{low}} + 1}\right) - \\
&- \frac{(m^{\text{high}} - m_0)}{\sqrt{1 + z^{\text{high}}}} \cdot {}_2F_1\left(\frac{1}{2}, \frac{3}{2} - \frac{1}{q-1}, \frac{3}{2}; \frac{z^{\text{high}}}{z^{\text{high}} + 1}\right),
\end{aligned} \tag{B.5}$$

where ${}_2F_1(a, b, c; z)$ is the hypergeometric function [162].

B.3   Gradient force

Here we make an estimate of the impact of the force $\vec{F} = \vec{\nabla}(\vec{m} \cdot \vec{B}) = \sum_k m_k \vec{\nabla} B_k$ (for $k = x, y, z$), where $\vec{m}$ is the particle's magnetic moment on the polarization evolution. In the laboratory frame, the magnetic field changes by $\Delta B_y \simeq 1.5$ T over the distance $L \simeq 1.5$ m along z axis. Due to time dilation, the particle flight path is $L = \gamma c \tau$, where τ is the Λ mean lifetime and $c\tau = 7.89$ cm. Hence, $\gamma \simeq 19$ and the hyperon momentum $p_\Lambda \simeq 21$ GeV/c, which is a typical Λ momentum for proton-proton collisions at 158 GeV/c beam momentum. Numerical value of nuclear magneton is $\mu_N = 3 \cdot 10^{-8}$ eV/T, and the Λ magnetic moment $|\vec{m}| \approx 0.6\mu_N$. In the Λ rest frame, the momentum change is $\Delta \vec{p} = \vec{F} \cdot \tau = m_y \vec{\nabla} B_y \tau$. Even if $\vec{m}$ is aligned with y axis, we find

$$\Delta p_z = 0.6\mu_N \frac{\gamma \Delta B_y}{L/\gamma} \tau \approx 5 \cdot 10^{-7} \text{ eV}/c. \tag{B.6}$$

Therefore, $v/c = p_z/(mc) \approx 5 \cdot 10^{-16}$ and this ratio is negligible. From the BMT equation (5.21), the spin vector change is quadratic in the speed of the particle: $\left|\Delta \vec{S}\right| \sim (v/c)^2 \sim 10^{-31}$, hence, the impact of the gradient force can be neglected.

Appendix C

Method of Moments

In statistics, the method of moments is a classical technique for estimating the parameters of a probability distribution using the moments (*i.e.*, expectations of powers) of the random variable. If acceptance of the detector $A(\cos\theta)$ is an even function in $\cos\theta$, to estimate the polarization value, acceptance bias can be taken into account using the formula [163]

$$\alpha P \pm \Delta(\alpha P) = \frac{\langle \cos\theta \rangle}{\langle \cos^2\theta \rangle} \pm \frac{1}{\sqrt{N}} \frac{\left[\langle \cos^2\theta \, (1 - \alpha P \cos\theta)^2 \rangle \right]^{1/2}}{\langle \cos^2\theta \rangle} \,, \tag{C.1}$$

where $\langle \dots \rangle$ is the mean value and N is the total number of Λ, and $\cos\theta$ is used as a shorthand for $\cos\theta_x$.

As for the P value, this formula is easy to prove, using the relation $A(\cos\theta_x) = A(-\cos\theta_x)$:

$$E[\cos\theta] = \int_{-1}^{1} A(\cos\theta) \cos\theta \frac{1}{2}(1 + \alpha P \cos\theta) d(\cos\theta) = \frac{1}{2} \int A(c) c^2 dc \,, \tag{C.2}$$

$$E[\cos^2\theta] = \frac{P}{2} \int A(c) c^2 dc \,, \tag{C.3}$$

where $E[\dots]$ is the expected value, c is a shorthand for $\cos\theta$, using the property for even functions $\int_{-1}^{1} A(c) c^{2n+1} dc = 0$. Hence, the estimator of polarization is

$$P = \frac{\langle \cos\theta_x \rangle}{\alpha \langle \cos^2\theta_x \rangle} \,. \tag{C.4}$$

As shown in Fig. 5.18, the $\cos\theta_x$ distribution is nearly even. Therefore, this method is employed in the following section to compare the results with those obtained using the unfolding method in Chapter 6. Figure C.1 shows the first ($\langle \cos\theta \rangle$, *top*) and second ($\langle \cos^2\theta \rangle$, *bottom*) moments calculated as:

$$\langle \cos^k\theta_x \rangle = \frac{\sum_{\cos\theta \text{ bins}} N_{\text{sig}}(\cos\theta_x) \times c^k}{\sum_{\cos\theta \text{ bins}} N_{\text{sig}}(\cos\theta_x)} \,, \tag{C.5}$$

where $N_{\text{sig}}(\cos\theta_x)$ is the Λ yield in particular $(x_F, p_T, \cos\theta)$ bin, and c is the center of corresponding $\cos\theta_x$ bin. The uncertainties shown in the figure are propagated from statistical uncertainties of the Λ yields. For zero polarization, it is expected that $\langle \cos\theta_x \rangle = 0$, which does not hold for both MC datasets and for many (x_F, p_T) bins around midrapidity for data, where zero polarization is expected. Figure C.2 shows the polarization estimate using this method. A significant bias is observed for MC datasets. The bias for the data is higher than the MC one for the backward hemisphere ($x_F < 0$), suggesting a non-zero polarization signal in this region.
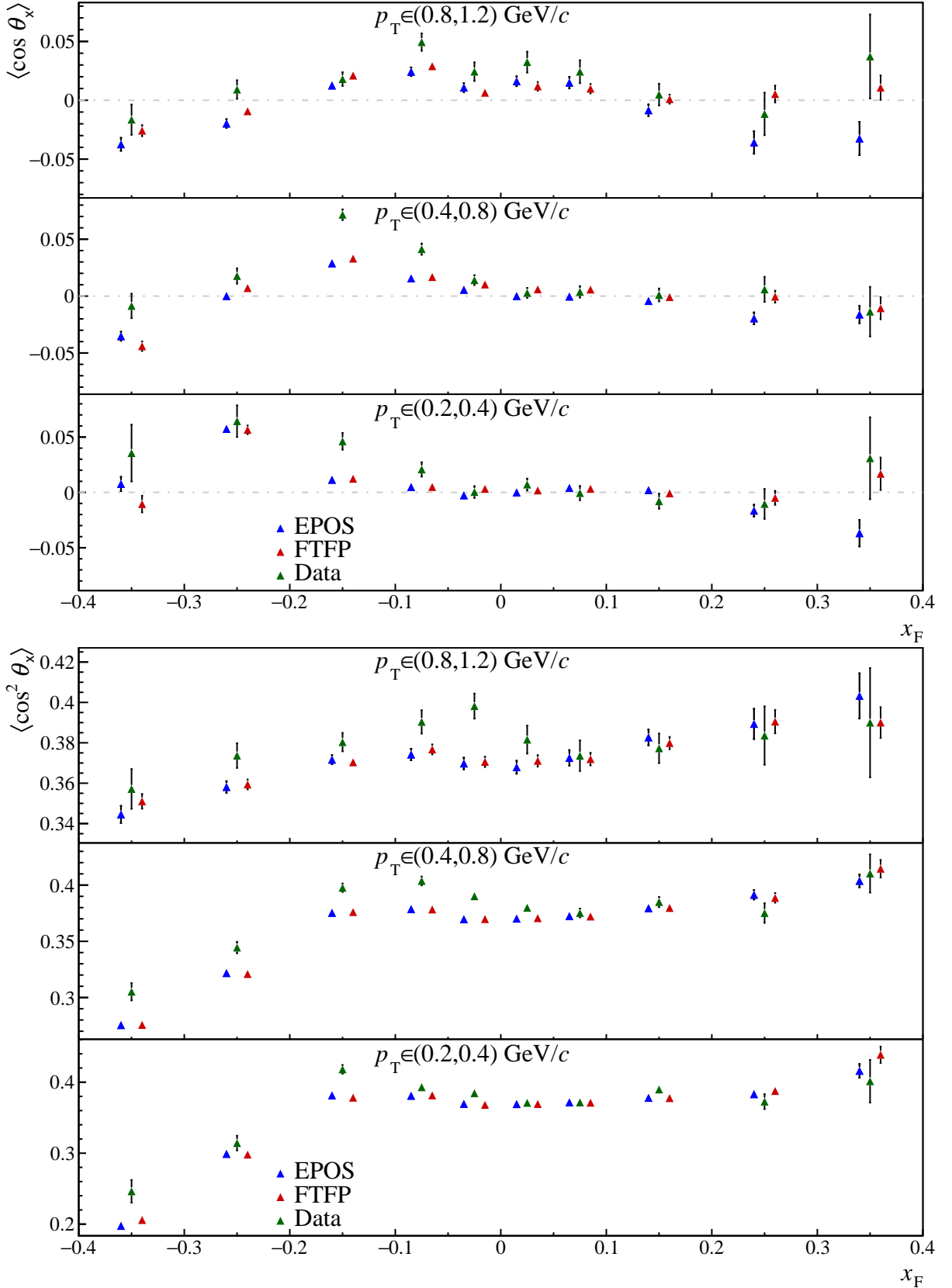
Figure C.1: The first ($\langle \cos\theta \rangle$, *top*) and second moments ($\langle \cos^2\theta \rangle$, *bottom*) in different (x_F, p_T) bins for data, EPOS and FTFP MC datasets. The uncertainties shown here are propagated from statistical uncertainties from Λ yields in $\cos\theta$ bins.
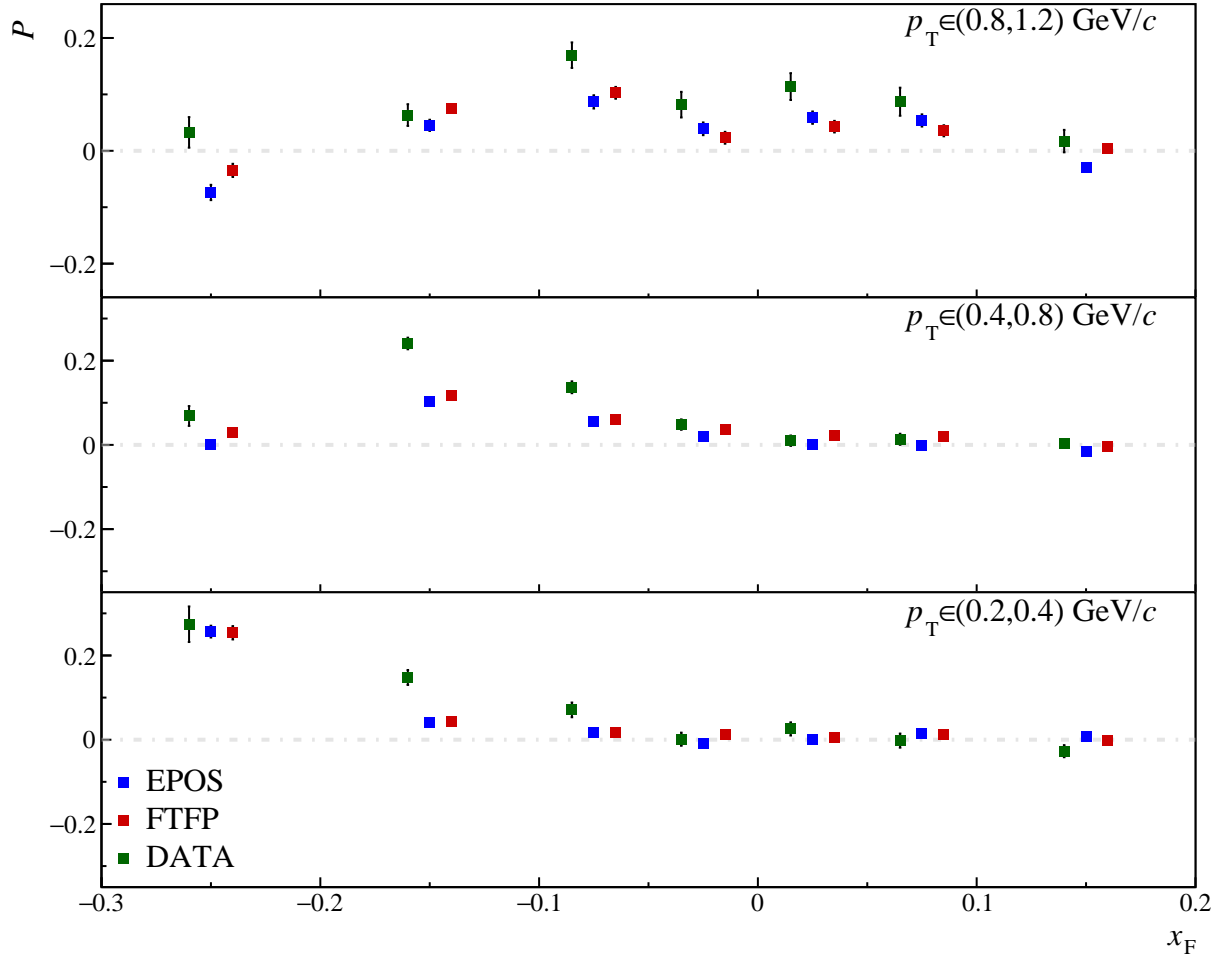
Figure C.2: Measured Λ transverse polarization using the method of moments (see Eq. (C.1)) for different (x_F, p_T) bins for data and MC datasets. Statistical uncertainties shown as error bars are calculated using Eq. (C.1).

C.1 Correction to method of moments

To address these significant biases, two ad hoc correction methods are implemented based on the Monte Carlo simulations. The first method, the subtractive MC correction, involves a direct subtraction of the polarization value obtained from the MC simulation from the result obtained from the experimental data, *i.e.*:

$$P = P_{\text{Data}} - P_{\text{MC}} \, . \tag{C.6}$$

The resulting Λ transverse polarization as a function of x_{F} in three p_{T} bins is presented in Fig. C.3. The uncertainties of the shown values are the sum in quadrature of the corresponding uncertainties in the data and MC values.
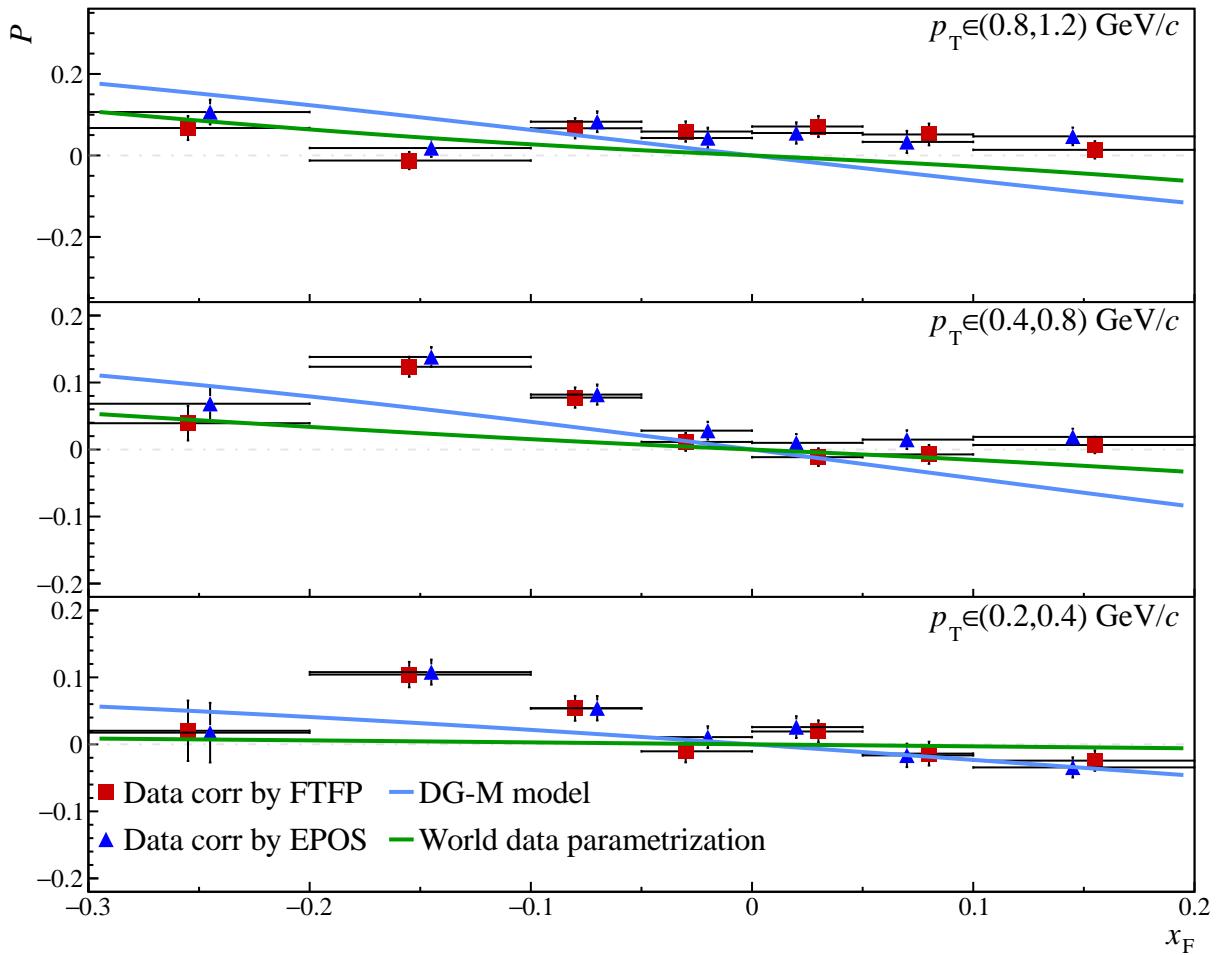
Figure C.3: Measured Λ transverse polarization using the method of moments (see Eq. (C.1)) with MC bias subtraction for different $(x_{\text{F}}, p_{\text{T}})$ bins using EPOS MC dataset (*red squares*) and FTFP dataset (*blue triangles*). The results are compared with the DeGrand-Miettinen model [52] (*blue line*) and world data parametrization [46] (*green line*) at $p_{\text{T}} = 1$ GeV/c (*top*), $p_{\text{T}} = 0.6$ GeV/c (*middle*), and $p_{\text{T}} = 0.3$ GeV/c (*bottom*). Statistical uncertainties shown as error bars are uncertainties of P_{Data} and P_{MC} added in quadrature.

C.2 Differential MC correction to method of moments

The second method, a differential MC correction, aims to correct the measured moments $\langle \cos^k \theta \rangle$ directly by using the ratio of signal asymmetry in bins of positive and negative $\cos \theta_x$ derived from the MC simulations. It leads to a modified form of Eq. (C.5):

$$\langle \cos^k \theta \rangle = \frac{\sum_{\cos \theta < 0 \text{ bins}} \left(\frac{N_{\text{sig}}(-\cos \theta_x)}{N_{\text{sig}}(\cos \theta_x)} \right)_{\text{MC}} \times N_{\text{sig}}(\cos \theta_x) c^k + \sum_{\cos \theta \geq 0 \text{ bins}} N_{\text{sig}}(\cos \theta_x) c^k}{\sum_{\cos \theta < 0 \text{ bins}} \left(\frac{N_{\text{sig}}(-\cos \theta_x)}{N_{\text{sig}}(\cos \theta_x)} \right)_{\text{MC}} \times N_{\text{sig}}(\cos \theta_x) + \sum_{\cos \theta \geq 0 \text{ bins}} N_{\text{sig}}(\cos \theta_x)} , \quad \text{(C.7)}$$

and then polarization is calculated using Eq. (C.1). The polarization estimates after this correction are presented in Fig. C.4.
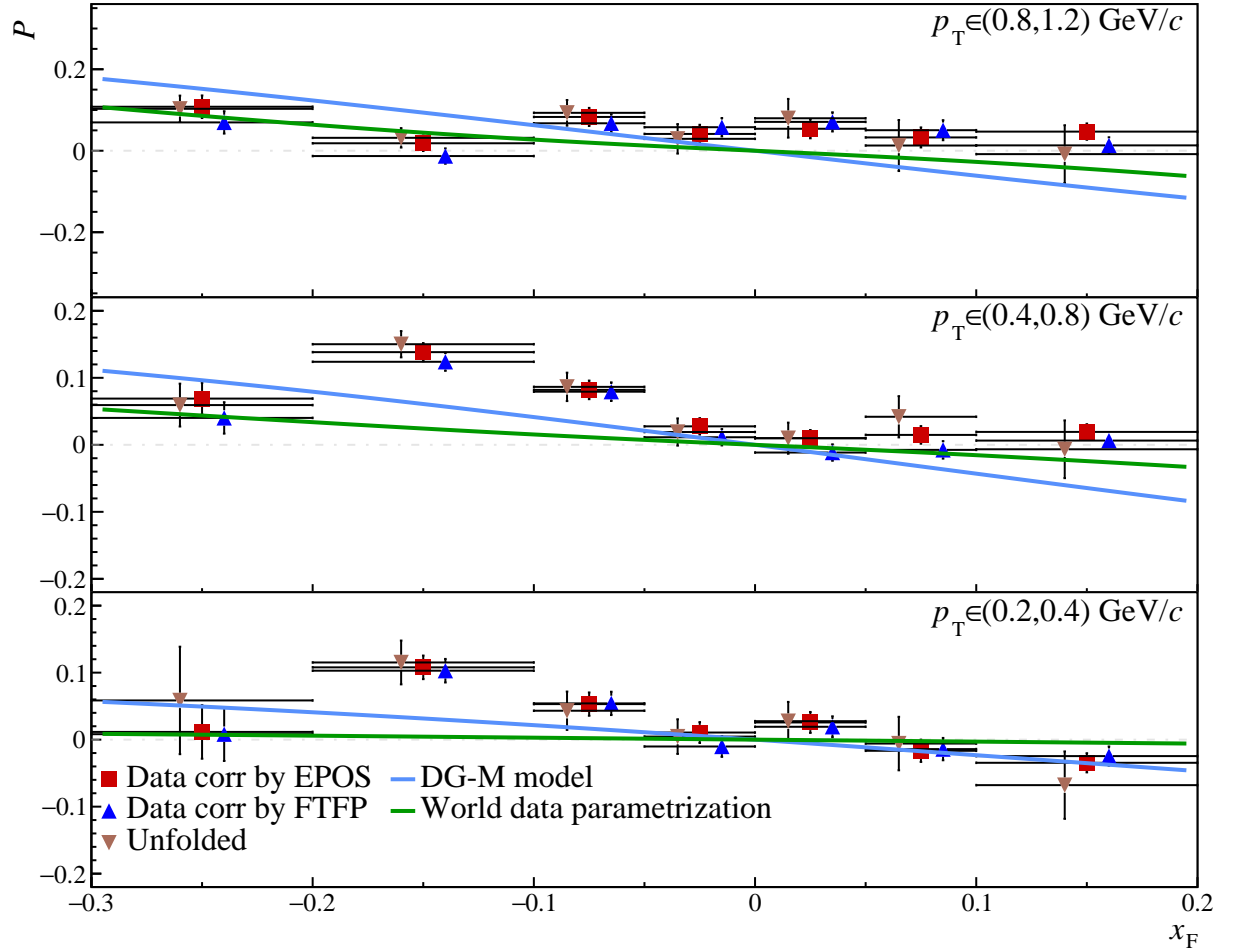
Figure C.4: Measured Λ transverse polarization using the method of moments (see Eq. (C.1)) with differential MC bias correction for different (x_F, p_T) bins using EPOS MC dataset (*red squares*) and FTFP dataset (*blue triangles*) with results using unfolding method shown in Chapter 6 (*brown triangles*). The results are compared with the DeGrand-Miettinen model [52] (*blue line*) and world data parametrization [46] (*green line*) at $p_T = 1$ GeV/c (*top*), $p_T = 0.6$ GeV/c (*middle*), and $p_T = 0.3$ GeV/c (*bottom*). Only statistical uncertainties are shown.

C.3   Conclusion on the Method of Moments

The Method of Moments (MM) was employed as an alternative technique to extract the Λ hyperon transverse polarization, complementary to the primary unfolding method. This method relies on estimating polarization parameters from the moments of the decay angular distribution, specifically the cosine of the decay angle, $\cos\theta_x$. The applicability of a simplified formula, Eq. (C.1), which accounts for acceptance bias if the detector acceptance is an even function of $\cos\theta_x$, was considered, and $\cos\theta_x$ was shown to be approximately even.

Ideally, for an unpolarized sample (such as the simulated Monte Carlo datasets generated with zero polarization), the first moment $\langle\cos\theta_x\rangle$ is expected to be zero. However, the application of the MM to both Monte Carlo simulations (EPOS and FTFP) and experimental data revealed significant deviations from this expectation, with $\langle\cos\theta_x\rangle$ being non-zero for MC datasets and in many (x_F, p_T) bins for data, particularly where zero polarization was anticipated. This indicates the presence of substantial biases inherent in the method when applied to these datasets, likely due to detector acceptance and event selection effects that influence the angular distribution moments. Specifically, a visible bias for MC was observed in the polarization estimates using this method, as illustrated in Fig. C.2. The bias encountered in the experimental data was found to be even higher than that for the MC in the backward hemisphere ($x_F < 0$).

To address these large biases, two *ad hoc* correction methods were implemented based on the Monte Carlo simulations: a subtractive correction and a differential correction. It was observed that both correction schemes yielded quantitatively similar results, producing polarization values that were in close agreement with one another within their respective uncertainties. However, when compared to the results from the primary unfolding analysis, both corrected Method of Moments estimates consistently yielded polarization values of a smaller magnitude. In contrast, the MM method resulted in lower statistical uncertainties compared to the unfolding method, an effect that is particularly pronounced in kinematic regions away from midrapidity.

The unfolding procedure was chosen as the principal technique for this thesis as it provides a more systematic and self-contained framework for bias correction. Although the MM served its purpose as a secondary analysis tool for a qualitative cross-check, its reliance on custom corrections limits its utility beyond that role.

Appendix D

Tables with numerical results

In this Appendix, tabulated results are presented for the shown Figures.

(x_F, p_T) bins	$(0, 0.2)$ GeV/c	$(0.2, 0.4)$ GeV/c	$(0.4, 0.8)$ GeV/c	$(0.8, 1.2)$ GeV/c
$(-0.4, -0.3)$	0.43 ± 0.48	0.00 ± 0.39	0.28 ± 0.29	-0.90 ± 0.43
	0.39 ± 0.49	-0.27 ± 0.38	-0.38 ± 0.29	0.14 ± 0.43
	0.49 ± 0.48	0.09 ± 0.38	0.15 ± 0.29	-0.43 ± 0.43
$(-0.3, -0.2)$	-0.08 ± 0.26	0.21 ± 0.21	0.25 ± 0.18	-0.23 ± 0.29
	-0.44 ± 0.26	0.04 ± 0.21	-0.05 ± 0.18	-0.25 ± 0.29
	0.52 ± 0.26	0.06 ± 0.21	0.30 ± 0.18	-0.07 ± 0.29
$(-0.2, -0.1)$	-0.09 ± 0.15	-0.03 ± 0.12	0.14 ± 0.12	0.13 ± 0.23
	0.13 ± 0.15	0.19 ± 0.12	0.11 ± 0.12	-0.01 ± 0.22
	-0.16 ± 0.15	-0.03 ± 0.12	0.08 ± 0.12	-0.08 ± 0.22
$(-0.1, -0.05)$	0.05 ± 0.15	0.03 ± 0.12	-0.15 ± 0.12	0.08 ± 0.27
	0.12 ± 0.15	-0.23 ± 0.12	-0.02 ± 0.12	-0.14 ± 0.27
	-0.25 ± 0.15	0.30 ± 0.12	-0.14 ± 0.12	0.13 ± 0.27
$(-0.05, 0)$	0.03 ± 0.14	-0.13 ± 0.11	0.04 ± 0.11	-0.05 ± 0.25
	0.23 ± 0.14	-0.04 ± 0.11	-0.00 ± 0.11	0.06 ± 0.25
	-0.03 ± 0.14	0.07 ± 0.11	0.01 ± 0.11	0.04 ± 0.25
$(0, 0.05)$	-0.28 ± 0.14	0.03 ± 0.11	-0.12 ± 0.11	-0.57 ± 0.25
	0.15 ± 0.14	-0.08 ± 0.11	0.01 ± 0.11	0.03 ± 0.24
	-0.06 ± 0.14	0.01 ± 0.11	0.12 ± 0.11	-0.25 ± 0.25
$(0.05, 0.1)$	0.09 ± 0.15	-0.10 ± 0.12	0.18 ± 0.11	-0.03 ± 0.25
	0.10 ± 0.15	0.04 ± 0.12	-0.10 ± 0.11	-0.21 ± 0.25
	-0.31 ± 0.15	-0.13 ± 0.12	0.22 ± 0.11	-0.07 ± 0.25
$(0.1, 0.2)$	0.02 ± 0.15	0.05 ± 0.12	0.08 ± 0.11	-0.20 ± 0.21
	-0.16 ± 0.15	0.04 ± 0.12	0.17 ± 0.11	0.10 ± 0.21
	0.10 ± 0.15	0.18 ± 0.11	-0.09 ± 0.11	0.01 ± 0.21
$(0.2, 0.3)$	0.03 ± 0.26	-0.08 ± 0.20	0.11 ± 0.18	0.89 ± 0.31
	0.21 ± 0.26	-0.36 ± 0.20	0.11 ± 0.18	-0.49 ± 0.31
	-0.15 ± 0.26	-0.08 ± 0.20	-0.24 ± 0.18	-0.73 ± 0.31
$(0.3, 0.4)$	1.51 ± 0.69	0.23 ± 0.42	0.27 ± 0.30	0.32 ± 0.48
	0.62 ± 0.70	0.08 ± 0.42	-0.57 ± 0.30	0.33 ± 0.48
	-0.54 ± 0.69	0.41 ± 0.42	0.15 ± 0.30	0.09 ± 0.48

Table D.1: For each x_F (rows) and p_T (columns) bin, three values P_i, $i = $ x, y, z (multiplied by 100) are present were shown at Fig. 5.29. See Sec. 5.8 for details.

(x_F, p_T) bins	$(0.2, 0.4)$ GeV/c	$(0.4, 0.8)$ GeV/c	$(0.8, 1.2)$ GeV/c
$(-0.3, -0.2)$	$0.059 \pm 0.080 \pm 0.150$	$0.059 \pm 0.032 \pm 0.046$	$0.103 \pm 0.032 \pm 0.059$
$(-0.2, -0.1)$	$0.115 \pm 0.033 \pm 0.028$	$0.150 \pm 0.020 \pm 0.040$	$0.032 \pm 0.024 \pm 0.043$
$(-0.1, -0.05)$	$0.043 \pm 0.029 \pm 0.036$	$0.086 \pm 0.021 \pm 0.031$	$0.093 \pm 0.032 \pm 0.030$
$(-0.05, 0)$	$0.005 \pm 0.026 \pm 0.024$	$0.019 \pm 0.020 \pm 0.032$	$0.029 \pm 0.036 \pm 0.046$
$(0, 0.05)$	$0.028 \pm 0.029 \pm 0.026$	$0.010 \pm 0.023 \pm 0.036$	$0.080 \pm 0.048 \pm 0.036$
$(0.05, 0.1)$	$-0.006 \pm 0.040 \pm 0.032$	$0.042 \pm 0.031 \pm 0.043$	$0.013 \pm 0.063 \pm 0.058$
$(0.1, 0.2)$	$-0.068 \pm 0.050 \pm 0.081$	$-0.007 \pm 0.043 \pm 0.057$	$-0.008 \pm 0.071 \pm 0.058$

Table D.2: Polarization values with statistical and systematic uncertainties are shown for (x_F, p_T) bins in $x_F \in (-0.3, 0.2)$ and $p_T \in (0.2, 1.2)$ GeV/c shown in Fig. 6.3. See Sec. 6 for details.

	x_F bins	WFA cut	Primary Vertex z cut	VTPC clusters cut	Δz cut	dE/dx cut	$\cos\theta_z$ cut	$b_{x,y}$ cut	m_{inv} range variation	m_{inv} fit parameters	q value variation	FTFP MC dataset	Unfolding method
$p_T \in (0.2, 0.4)$ GeV/c	$(-0.3, -0.2)$	1.7	3.7	12.4	1.9	1.6	1.8	1.6	1.9	3.6	4.6	1.2	1.2
	$(-0.2, -0.1)$	0.3	0.8	1.8	0.7	0.4	0.5	0.8	0.3	0.3	0.3	0.1	1.4
	$(-0.1, -0.05)$	0.7	0.7	1.9	1.4	1.3	0.7	0.1	0.4	0.7	0.5	0.1	1.7
	$(-0.05, 0)$	0.2	0.4	0.2	1.2	0.3	0.1	0.2	0.7	0.4	0.6	1.5	0.8
	$(0, 0.05)$	0.4	0.4	0.3	1.2	1.1	0.4	0.4	0.7	0.7	0.5	1.4	0.5
	$(0.05, 0.1)$	0.4	0.6	1.7	1.8	0.7	0.2	0.4	0.6	0.7	0.4	0.6	1.1
	$(0.1, 0.2)$	1.1	0.9	2.4	2.1	2.0	1.9	1.3	1.7	0.6	1.9	0.1	6.1
$p_T \in (0.4, 0.8)$ GeV/c	$(-0.3, -0.2)$	1.1	0.6	1.8	1.8	1.3	1.0	0.7	0.3	0.3	1.0	2.9	0.2
	$(-0.2, -0.1)$	0.3	0.7	1.8	1.6	1.3	0.3	0.8	0.2	0.9	0.5	2.4	0.3
	$(-0.1, -0.05)$	0.3	0.5	1.7	0.2	1.3	0.9	0.3	0.7	0.5	0.7	1.6	0.2
	$(-0.05, 0)$	0.5	0.3	1.7	0.9	1.4	0.2	0.5	0.4	0.6	0.5	1.1	1.4
	$(0, 0.05)$	0.7	1.0	1.3	0.9	1.2	0.4	0.7	0.7	0.6	0.9	2.0	0.9
	$(0.05, 0.1)$	0.8	1.2	0.9	1.5	1.3	0.3	0.8	0.4	0.7	1.1	1.9	2.4
	$(0.1, 0.2)$	1.1	1.5	1.5	0.6	1.8	4.1	1.2	0.9	0.7	0.3	0.2	1.7
$p_T \in (0.8, 1.2)$ GeV/c	$(-0.3, -0.2)$	1.3	0.6	1.8	2.2	1.2	1.1	0.6	1.3	1.0	1.6	4.0	0.2
	$(-0.2, -0.1)$	1.3	0.6	0.3	1.1	0.8	0.5	0.5	0.2	1.3	0.3	3.5	0.1
	$(-0.1, -0.05)$	0.6	0.2	1.8	0.7	0.9	0.2	0.6	0.2	0.6	0.2	1.8	0.3
	$(-0.05, 0)$	1.1	1.2	1.0	1.4	1.7	1.3	1.2	1.2	1.2	1.3	1.8	1.3
	$(0, 0.05)$	0.3	0.6	1.8	0.6	1.8	0.9	0.4	0.5	0.5	0.8	0.4	1.8
	$(0.05, 0.1)$	1.2	1.1	2.2	1.8	1.5	1.0	1.6	1.5	1.2	1.7	2.6	2.0
	$(0.1, 0.2)$	1.0	0.4	1.9	0.4	3.3	0.6	0.9	1.1	0.6	0.8	2.3	3.1

Table D.3: Contributions to the systematical uncertainty (multiplied by 100) of measured Λ transverse polarization by each cut variation and other sources, defined in Sec. 5.7 and shown in Fig. 6.6.

p_T interval	$\langle p_T \rangle$	$\langle x_F \rangle$	P
$(0.3, 0.4)$	0.36 ± 0.03	0.16 ± 0.01	$-0.057 \pm 0.015^{+0.006}_{-0.032}$
$(0.4, 0.5)$	0.45 ± 0.03	0.21 ± 0.01	$-0.098 \pm 0.015^{+0.005}_{-0.018}$
$(0.5, 0.6)$	0.54 ± 0.03	0.25 ± 0.01	$-0.133 \pm 0.021^{+0.009}_{-0.030}$
$(0.6, 0.7)$	0.64 ± 0.03	0.30 ± 0.01	$-0.179 \pm 0.030^{+0.013}_{-0.034}$
$(0.7, 1.0)$	0.86 ± 0.05	0.37 ± 0.02	$-0.256 \pm 0.064^{+0.022}_{-0.066}$

Table D.4: The selected values of Λ polarization produced by 400 GeV/c proton beam with Be target in NA48 experiment [18] displayed in Fig. 6.8.

$\langle p_T \rangle$	$\langle x_F \rangle$	P
0.67	0.172	-0.057 ± 0.033
0.87	0.226	-0.055 ± 0.014
1.09	0.283	-0.068 ± 0.012
1.32	0.342	-0.076 ± 0.012
1.56	0.403	-0.108 ± 0.013
1.80	0.465	-0.140 ± 0.016
2.15	0.556	-0.170 ± 0.020

Table D.5: The selected values of Λ polarization produced by 800 GeV/c proton beam with Be target in E799 experiment [17] at scattering angle $\theta \approx 4.8$ mrad, displayed in Fig. 6.8. Fig. 6.8.

$\langle p_T \rangle$	$\langle x_F \rangle$	P
0.621	0.247	-0.054 ± 0.003
0.806	0.331	-0.077 ± 0.003
0.955	0.405	-0.107 ± 0.004
1.106	0.479	-0.154 ± 0.006
1.253	0.553	-0.191 ± 0.009
1.397	0.628	-0.215 ± 0.016
1.528	0.702	-0.213 ± 0.029
1.693	0.777	-0.280 ± 0.058

Table D.6: The selected values of Λ polarization produced by 400 GeV/c proton beam with Be target in M2 experiment [18] displayed in Fig. 6.8. Results are given as functions of bin-averaged values $\langle p_T \rangle$ (GeV/c) and $\langle x_F \rangle$ at scattering angle $\theta \approx 6$ mrad. The contribution of the systematic uncertainty was considered negligible compared to the statistical ones.

x_F	p_T	P
0.25	0.89	-0.044 ± 0.016
0.38	0.89	-0.117 ± 0.011
0.38	1.02	-0.137 ± 0.013
0.58	0.89	-0.172 ± 0.016
0.58	1.02	-0.213 ± 0.020
0.77	0.89	-0.319 ± 0.043
0.77	1.02	-0.322 ± 0.040

Table D.7: The selected values of Λ polarization in $p+p$ interactions at $\sqrt{s} = 62$ GeV by the R608 Collaboration [157] at $0.8 < p_T < 1.2$ GeV/c displayed in Fig. 6.8. The detected Λ hyperons are produced in the forward direction with center-of-mass polar angles in the range $0.023 < \theta < 0.150$ rad.

x_F interval	P
$(-0.250, -0.060)$	$0.116 \pm 0.040 \pm 0.015$
$(-0.060, -0.040)$	$0.005 \pm 0.036 \pm 0.025$
$(-0.040, -0.025)$	$-0.009 \pm 0.037 \pm 0.020$
$(-0.025, 0.100)$	$-0.022 \pm 0.036 \pm 0.017$

Table D.8: The values of Λ polarization in bins of x_F at $p+$Ne collisions at $\sqrt{s} = 68.4$ GeV by the LHCb Collaboration [23] displayed in Fig. 6.8. The first uncertainties are statistical and the second are systematic. The data is integrated over the $0.3 < p_T < 3$ GeV/c.

Bibliography

[1] S. Erhan et al., "Λ^0 polarization in proton-proton interactions at $\sqrt{s}$ = 53 and 62 GeV", *Phys. Lett. B*, vol. 82, no. 2, pp. 301–304. DOI: `10.1016/0370-2693(79)90761-5`.

[2] A. D. Panagiotou, "Λ^0 polarization in hadron-nucleon, hadron-nucleus and nucleus-nucleus interactions", *Int. J. Mod. Phys. A*, vol. 05, no. 07, pp. 1197–1266. DOI: `10.1142/S0217751X90000568`.

[3] N. Abgrall et al., "NA61/SHINE facility at the CERN SPS: beams and detector system", *JINST*, vol. 9, P06005. DOI: `10.1088/1748-0221/9/06/P06005`.

[4] W. Gerlach and O. Stern, "Der experimentelle nachweis der richtungsquantelung im magnetfeld", *Z. Phys.*, vol. 9, no. 1, pp. 349–352. DOI: `10.1007/BF01326983`.

[5] E. Boldt, D. O. Caldwell, and Y. Pal, "Λ^0, $\theta_1^{\ 0}$, $\theta_2^{\ 0}$, and $\overline{\theta}^0$ lifetimes", *Phys. Rev. Lett.*, vol. 1, no. 4, pp. 148–150. DOI: `10.1103/PhysRevLett.1.148`.

[6] A. Pais, "Some remarks on the *V*-particles", *Phys. Rev.*, vol. 86, no. 5, pp. 663–672. DOI: `10.1103/PhysRev.86.663`.

[7] T. Nakano and K. Nishijima, "Charge Independence for V-particles*", *Prog. Theor. Phys.*, vol. 10, no. 5, pp. 581–582. DOI: `10.1143/PTP.10.581`.

[8] K. Nishijima, "Charge Independence Theory of V Particles*", *Prog. Theor. Phys.*, vol. 13, no. 3, pp. 285–304. DOI: `10.1143/PTP.13.285`.

[9] M. Gell-Mann, "The interpretation of the new particles as displaced charge multiplets", *Il Nuovo Cimento (1955-1965)*, vol. 4, no. 2, pp. 848–866. DOI: `10.1007/BF02748000`.

[10] M. Gell-Mann, "A schematic model of baryons and mesons", *Phys. Lett.*, vol. 8, no. 3, pp. 214–215. DOI: `10.1016/S0031-9163(64)92001-3`.

[11] J. Letessier and J. Rafelski, *Hadrons and Quark–Gluon Plasma* (Cambridge Monographs on Particle Physics, Nuclear Physics and Cosmology). Cambridge University Press, 2002, ISBN: 9781139433037.

[12] S. Navas et al., "Review of Particle Physics", *Phys. Rev. D*, vol. 110, no. 3, p. 030 001. DOI: `10.1103/PhysRevD.110.030001`.

[13] S. A. Gourlay et al., "Polarization of $\Lambda' s$ and $\overline{\Lambda}' s$ in pp, $\overline{p}p$, and $K^- p$ interactions at 176 GeV/c", *Phys. Rev. Lett.*, vol. 56, no. 21, pp. 2244–2247. DOI: `10.1103/PhysRevLett.56.2244`.

[14] G. Aad et al., "Measurement of the transverse polarization of Λ and $\overline{\Lambda}$ hyperons produced in proton-proton collisions at $\sqrt{s}$ = 7 TeV using the ATLAS detector", *Phys. Rev. D*, vol. 91, no. 3, p. 032 004. DOI: `10.1103/PhysRevD.91.032004`.

[15] I. Abt et al., "Polarization of Λ and $\overline{\Lambda}$ in 920 GeV fixed-target proton–nucleus collisions", *Phys. Lett. B*, vol. 638, no. 5, pp. 415–421. DOI: `10.1016/j.physletb.2006.05.040`.

[16] V. Fanti et al., "A measurement of the transverse polarization of Λ-hyperons produced in inelastic pN-reactions at 450 GeV proton energy", *Eur. Phys. J. C*, vol. 6, no. 2, pp. 265–269. DOI: `10.1007/s100529801045`.

[17] E. Ramberg et al., "Polarization of Λ and $\overline{\Lambda}$ produced by 800-GeV protons", *Phys. Lett. B*, vol. 338, no. 2, pp. 403–408. DOI: `10.1016/0370-2693(94)91397-8`.

[18] B. Lundberg et al., "Polarization in inclusive Λ and $\overline{\Lambda}$ production at large p_T", *Phys. Rev. D*, vol. 40, no. 11, pp. 3557–3567. DOI: `10.1103/PhysRevD.40.3557`.

[19] M. Adamovich et al., "A measurement of Λ polarization in inclusive production by Σ^- of 340 GeV/c in C and Cu targets", *Eur. Phys. J. C*, vol. 32, no. 2, pp. 221–228. DOI: `10.1140/epjc/s2003-01357-3`.

[20] A. Airapetian et al., "Transverse polarization of Λ and $\overline{\Lambda}$ hyperons in quasireal photoproduction", *Phys. Rev. D*, vol. 76, no. 9, p. 092 008. DOI: `10.1103/PhysRevD.76.092008`.

[21] M. Anikina et al., "Characteristics of Λ and K^0 particles produced in central nucleus nucleus collisions at a 4.5 GeV/c momentum per incident nucleon", *Z. Phys. C*, vol. 25, no. 1, pp. 1–11. DOI: `10.1007/BF01571951`.

[22] G. Agakishiev et al., "Lambda hyperon production and polarization in collisions of p(3.5 GeV)+Nb", *Eur. Phys. J. A*, vol. 50, no. 5, p. 81. DOI: `10.1140/epja/i2014-14081-2`.

[23] R. Aaij et al., "Transverse polarization measurement of Λ hyperons in pNe collisions at $\sqrt{s_{\mathrm{NN}}}$ = 68.4 GeV with the LHCb detector", *JHEP*, vol. 2024, no. 9, p. 82. DOI: `10.1007/JHEP09(2024)082`.

[24] A. Airapetian et al., "Transverse polarization of Λ hyperons from quasireal photoproduction on nuclei", *Phys. Rev. D*, vol. 90, no. 7, p. 072 007. DOI: `10.1103/PhysRevD.90.072007`. [Online]. Available: `https://link.aps.org/doi/10.1103/PhysRevD.90.072007`.

[25] S. N. Ganguli et al., "Inclusive production of lambda in the proton fragmentation region from K⁻p → ΛX at 4.2 GeV/c", *Nuovo Cim. A*, vol. 44, pp. 345–366. DOI: `10.1007/BF02812977`.

[26] T. Haupt et al., "Polarization of Λ^0 hyperons in $K^- p$ interactions", *Z. Phys. C*, vol. 28, no. 1, pp. 57–63. DOI: `10.1007/BF01550249`.

[27] J. L. Sánchez-López et al., *Polarization of Λ^0 and $\bar{\Lambda}^0$ inclusively produced by 610 GeV/c Σ^- and 525 GeV/c proton beams*, 2007. arXiv: `0706.3660` [hep-ex].

[28] P. H. Stuntebeck, N. M. Cason, J. M. Bishop, N. N. Biswas, V. P. Kenney, and W. D. Shephard, "Inclusive production of K_1^0, Λ^0, and Λ^0 in $18.5 - \mathrm{GeV}/c\pi^{\pm}p$ interactions", *Phys. Rev. D*, vol. 9, no. 3, pp. 608–620. DOI: `10.1103/PhysRevD.9.608`.

[29] R. Sugahara et al., "Inclusive strange particle production in $\pi^- p$ intereactions at 6-GeV/c", *Nucl. Phys. B*, vol. 156, pp. 237–251. DOI: `10.1016/0550-3213(79)90029-4`.

[30] P. Astier et al., "Measurement of the Λ polarization in ν_μ charged current interactions in the NOMAD experiment", *Nucl. Phys. B*, vol. 588, no. 1, pp. 3–36. DOI: `10.1016/S0550-3213(00)00503-4`.

[31] I. A. Alikhanov and O. G. Grebenyuk, "Transverse Λ^0 polarization in inclusive quasi-real photoproduction: Quark scattering model", *Phys. Atom. Nucl.*, vol. 71, no. 8, pp. 1424–1430. DOI: `10.1134/S1063778808080139`. arXiv: `hep-ph/0604239`.

[32] Y. Guan et al., "Observation of transverse $\Lambda/\overline{\Lambda}$ hyperon polarization in e^+e^- annihilation at belle", *Phys. Rev. Lett.*, vol. 122, no. 4, p. 042 001. DOI: `10.1103/PhysRevLett.122.042001`.

[33] K. Heller et al., "Polarization of Ξ^0 and Λ hyperons produced by 400-GeV/c protons", *Phys. Rev. Lett.*, vol. 51, no. 22, pp. 2025–2028. DOI: `10.1103/PhysRevLett.51.2025`.

[34] J. Duryea et al., "Polarization of Ξ^- hyperons produced by 800-GeV protons", *Phys. Rev. Lett.*, vol. 67, no. 10, pp. 1193–1196. DOI: `10.1103/PhysRevLett.67.1193`.

[35] C. Wilkinson et al., "Polarization of Σ^+ hyperons produced by 400-GeV protons", *Phys. Rev. Lett.*, vol. 46, no. 13, pp. 803–806. DOI: `10.1103/PhysRevLett.46.803`.

[36] Y. W. Wah et al., "Measurement of Σ^- production polarization and magnetic moment", *Phys. Rev. Lett.*, vol. 55, no. 23, pp. 2551–2554. DOI: `10.1103/PhysRevLett.55.2551`. [Online]. Available: `https://lss.fnal.gov/archive/1985/pub/Pub-85-128-E.pdf`.

[37] E. C. Dukes et al., "Polarization of Σ^0 hyperons in inclusive production from 28.5 GeV/c protons on beryllium", *Phys. Lett. B*, vol. 193, no. 1, pp. 135–139. DOI: `10.1016/0370-2693(87)90471-0`.

[38] K. Heller et al., "Polarization of Λ's and $\overline{\Lambda}'$s produced by 400-GeV protons", *Phys. Rev. Lett.*, vol. 41, no. 9, pp. 607–611. DOI: `10.1103/PhysRevLett.41.607`. [Online]. Available: `https://lss.fnal.gov/archive/1978/pub/fermilab-pub-78-145-e.pdf`, Erratum: "Polarization of Λ's and $\overline{\Lambda}$'s produced by 400-GeV protons", *Phys. Rev. Lett.*, vol. 45, no. 12, pp. 1043–1043. DOI: `10.1103/PhysRevLett.45.1043`.

[39] K. B. Luk et al., "Polarization of Ω^- hyperons produced in 800 GeV proton-beryllium collisions", *Phys. Rev. Lett.*, vol. 70, no. 7, pp. 900–903. DOI: `10.1103/PhysRevLett.70.900`.

[40] P. M. Ho et al., "Measurement of the polarization and magnetic moment of $\overline{\varXi}^+$ antihyperons produced by 800-GeV/c protons", *Phys. Rev. D*, vol. 44, no. 11, pp. 3402–3418. DOI: `10.1103/PhysRevD.44.3402`.

[41] P. M. Ho et al., "Production polarization and magnetic moment of $\overline{\varXi}^+$ antihyperons produced by 800-GeV/c protons", *Phys. Rev. Lett.*, vol. 65, no. 14, pp. 1713–1716. DOI: `10.1103/PhysRevLett.65.1713`.

[42] A. Morelos et al., "Polarization of $\varSigma^+$ and $\overline{\varSigma}^-$ hyperons produced by 800-GeV/c protons", *Phys. Rev. Lett.*, vol. 71, no. 14, pp. 2172–2175. DOI: `10.1103/PhysRevLett.71.2172`. [Online]. Available: `https://lss.fnal.gov/archive/1993/pub/Pub-93-167-E.pdf`.

[43] C. Nunez, "Studying hyperon polarization at the large hadron collider beauty experiment", Ph.D. dissertation, Michigan U., 2024. [Online]. Available: `https://cds.cern.ch/record/2920914/`.

[44] M. Jacob and J. Rafelski, "Longitudinal $\overline{\varLambda}$ polarization, $\overline{\varXi}$ abundance and quark gluon plasma formation", *Phys. Lett. B*, vol. 190, no. 1, pp. 173–176. DOI: `10.1016/0370-2693(87)90862-8`.

[45] K. Heller, "Inclusive hyperon polarization: A review", *J. Phys. Colloques*, vol. 46, no. C2, pp. C2-121-C2–129. DOI: `10.1051/jphyscol:1985212`.

[46] V. V. Abramov, *Universal scaling behaviour of the transverse polarization for inclusively produced hyperons in hadron-hadron collisions*, 2001. DOI: `10.48550/arXiv.hep-ph/0111128`.

[47] J. W. Harris et al., "$\varLambda$ production near threshold in central nucleus-nucleus collisions", *Phys. Rev. Lett.*, vol. 47, no. 4, pp. 229–232. DOI: `10.1103/PhysRevLett.47.229`.

[48] R. Bellwied, "The measurement of transverse polarization of $\varLambda$ hyperons in relativistic heavy ion collisions", *Nucl. Phys. A*, vol. 698, no. 1, 15th Int. Conf. on Ultra-Relativistic Nucleus-Nucleus Collisions (Quark Matter 2001), pp. 499–502. DOI: `10.1016/S0375-9474(01)01413-0`.

[49] E. Schillings, "$\varLambda$ polarization in lead-lead collisions", Ph.D. dissertation, Universiteit Utrecht, 2003. [Online]. Available: `https://dspace.library.uu.nl/bitstream/handle/1874/694/full.pdf`.

[50] B. Andersson, G. Gustafson, and G. Ingelman, "A semiclassical model for the polarization on inclusively produced $\varLambda^0$-particles at high energies", *Phys. Lett. B*, vol. 85, no. 4, pp. 417–420. DOI: `10.1016/0370-2693(79)91286-3`.

[51] B. Andersson, G. Gustafson, G. Ingelman, and T. Sjöstrand, "Parton fragmentation and string dynamics", *Phys. Rep.*, vol. 97, no. 2, pp. 31–145. DOI: `10.1016/0370-1573(83)90080-7`.

[52] T. A. DeGrand and H. I. Miettinen, "Quark dynamics of polarization in inclusive hadron production", *Phys. Rev. D*, vol. 23, no. 5, pp. 1227–1230. DOI: `10.1103/PhysRevD.23.1227`, Erratum: T. A. DeGrand and H. I. Miettinen, "Erratum: Models for polarization asymmetry in inclusive hadron production", *Phys. Rev. D*, vol. 31, no. 3, pp. 661–661. DOI: `10.1103/PhysRevD.31.661`.

[53] T. A. DeGrand and H. I. Miettinen, "Models for polarization asymmetry in inclusive hadron production", *Phys. Rev. D*, vol. 24, no. 9, pp. 2419–2427. DOI: `10.1103/PhysRevD.24.2419`.

[54] K.-i. Kubo, Y. Yamamoto, and H. Toki, "New Mechanisms for the Anomalous Spin Observables in High Energy Hyperon Productions", *Prog. Theor. Phys.*, vol. 101, no. 3, pp. 615–625. DOI: `10.1143/PTP.101.615`.

[55] D. J. Herndon, P. Söding, and R. J. Cashmore, "Generalized isobar model formalism", *Phys. Rev. D*, vol. 11, no. 11, pp. 3165–3182. DOI: `10.1103/PhysRevD.11.3165`.

[56] S. Ganguli and D. Roy, "Regge phenomenology of inclusive reactions", *Phys. Rep.*, vol. 67, no. 2, pp. 201–395. DOI: `10.1016/0370-1573(80)90067-8`.

[57] V. V. Abramov et al., "Conceptual design of the SPASCHARM experiment", *Phys. Part. Nucl.*, vol. 54, no. 1, pp. 69–184. DOI: `10.1134/S1063779623010021`.

[58] J. Félix, "On theoretical studies of Λ^0 polarization", *Mod. Phys. Lett. A*, vol. 14, no. 13, pp. 827–842. DOI: `10.1142/S0217732399000870`.

[59] Z.-t. Liang and C. Boros, "Single spin asymmetries in inclusive high-energy hadron hadron collision processes", *Int. J. Mod. Phys. A*, vol. 15, no. 07, pp. 927–982. DOI: `10.1142/S0217751X0000046X`. arXiv: `hep-ph/0001330`.

[60] S. M. Troshin and N. E. Tyurin, "The challenge of hyperon polarization", *AIP Conf. Proc.*, vol. 675, no. 1, pp. 579–583. DOI: `10.1063/1.1607201`. arXiv: `hep-ph/0201267`.

[61] S. M. Troshin and N. E. Tyurin, "Hyperon polarization in the constituent quark model", *Phys. Rev. D*, vol. 55, no. 3, pp. 1265–1272. DOI: `10.1103/PhysRevD.55.1265`. arXiv: `hep-ph/9602392`.

[62] L. Zuo-tang and C. Boros, "Hyperon polarization and single spin left-right asymmetry in inclusive production processes at high energies", *Phys. Rev. Lett.*, vol. 79, no. 19, pp. 3608–3611. DOI: `10.1103/PhysRevLett.79.3608`. arXiv: `hep-ph/9708488`.

[63] J. Szwed, "Hyperon polarization at high energies", *Phys. Lett. B*, vol. 105, no. 5, pp. 403–405. DOI: `10.1016/0370-2693(81)90788-7`.

[64] J. Gago, R. Mendes, and P. Vaz, "Is the Λ polarization in inclusive K^-p compatible with QCD?", *Phys. Lett. B*, vol. 183, no. 3, pp. 357–360. DOI: `10.1016/0370-2693(87)90978-6`.

[65] D. Sivers, "Single-spin production asymmetries from the hard scattering of pointlike constituents", *Phys. Rev. D*, vol. 41, no. 1, pp. 83–90. DOI: `10.1103/PhysRevD.41.83`.

[66] J. Collins, "Fragmentation of transversely polarized quarks probed in transverse momentum distributions", *Nucl. Phys. B*, vol. 396, no. 1, pp. 161–182. DOI: `10.1016/0550-3213(93)90262-N`. arXiv: `hep-ph/9208213`.

[67] Y. Kanazawa and Y. Koike, "Polarization in hadronic Λ hyperon production and chiral-odd twist-3 distribution", *Phys. Rev. D*, vol. 64, no. 3, p. 034 019. DOI: `10.1103/PhysRevD.64.034019`. arXiv: `hep-ph/0012225`.

[68] Y. Koike, A. Metz, D. Pitonyak, K. Yabe, and S. Yoshida, "Twist-3 fragmentation contribution to polarized hyperon production in unpolarized hadronic collisions", *Phys. Rev. D*, vol. 95, no. 11, p. 114 013. DOI: `10.1103/PhysRevD.95.114013`. arXiv: `1703.09399 [hep-ph]`.

[69] R. Ikarashi, Y. Koike, K. Yabe, and S. Yoshida, "New derivation of the twist-3 gluon fragmentation contribution to polarized hyperon production", *Phys. Rev. D*, vol. 106, no. 7, p. 074 006. DOI: `10.1103/PhysRevD.106.074006`.

[70] V. Barone, F. Bradamante, and A. Martin, "Transverse-spin and transverse-momentum effects in high-energy processes", *Prog. Part. Nucl. Phys.*, vol. 65, no. 2, pp. 267–333. DOI: `10.1016/j.ppnp.2010.07.003`. arXiv: `1011.0909 [hep-ph]`.

[71] T. A. DeGrand, J. Markkanen, and H. I. Miettinen, "Hyperon polarization asymmetry: Polarized beams and Ω^- production", *Phys. Rev. D*, vol. 32, no. 9, pp. 2445–2448. DOI: `10.1103/PhysRevD.32.2445`.

[72] T. Anticic et al., "Λ and $\overline{\Lambda}$ Production in Central Pb-Pb Collisions at 40, 80, and 158A GeV", *Phys. Rev. Lett.*, vol. 93, no. 2, p. 022 302. DOI: `10.1103/PhysRevLett.93.022302`. arXiv: `nucl-ex/0311024`.

[73] M. Merschmeyer et al., "K^0 and Λ production in Ni+Ni collisions near threshold", *Phys. Rev. C*, vol. 76, no. 2, p. 024 906. DOI: `10.1103/PhysRevC.76.024906`. arXiv: `nucl-ex/0703036`.

[74] M. Justice et al., "Λ hyperons in 2 A GeV Ni + Cu collisions", *Phys. Lett. B*, vol. 440, pp. 12–19. DOI: `10.1016/S0370-2693(98)01159-9`. arXiv: `nucl-ex/9708005`.

[75] S. Albergo et al., "Λ Spectra in 11.6$AGeV/c$ Au-Au Collisions", *Phys. Rev. Lett.*, vol. 88, no. 6, p. 062 301. DOI: `10.1103/PhysRevLett.88.062301`.

[76] J. Barrette et al., "Λ production and flow in Au+Au collisions at 11.5A GeV/c", *Phys. Rev. C*, vol. 63, no. 1, p. 014 902. DOI: `10.1103/PhysRevC.63.014902`. arXiv: `nucl-ex/0007007`.

[77] C. Adler et al., "Midrapidity Λ and $\overline{\Lambda}$ production in Au + Au collisions at $\sqrt{s_{NN}} = 130$ GeV", *Phys. Rev. Lett.*, vol. 89, no. 9, p. 092 301. DOI: `10.1103/PhysRevLett.89.092301`. arXiv: `nucl-ex/0203016`.

[78] K. Adcox et al., "Measurement of Λ and $\overline{\Lambda}$ particles in Au + Au collisions at $\sqrt{s_{NN}} = 130$ GeV", *Phys. Rev. Lett.*, vol. 89, no. 9, p. 092 302. DOI: `10.1103/PhysRevLett.89.092302`. arXiv: `nucl-ex/0204007`.

[79] J. Adams et al., "Scaling properties of hyperon production in Au + Au collisions at $\sqrt{s_{NN}} = 200$ GeV", *Phys. Rev. Lett.*, vol. 98, no. 6, p. 062 301. DOI: `10.1103/PhysRevLett.98.062301`. arXiv: `nucl-ex/0606014`.

[80] B. I. Abelev, M. M. Aggarwal, Z. Ahammed, B. D. Anderson, D. Arkhipkin, and G. S. Averichev, "Enhanced strange baryon production in Au+Au collisions compared to $p + p$ at $\sqrt{s_{NN}} = 200$ GeV", *Phys. Rev. C*, vol. 77, no. 4, p. 044 908. DOI: `10.1103/PhysRevC.77.044908`. arXiv: `0705.2511 [nucl-ex]`.

[81] A. D. Panagiotou, "Λ^0 nonpolarization: Possible signature of quark matter", *Phys. Rev. C*, vol. 33, no. 6, pp. 1999–2002. DOI: `10.1103/PhysRevC.33.1999`.

[82] A. Ayala, E. Cuautle, G. Herrera, and L. M. Montaño, "Λ^0 polarization as a probe for production of deconfined matter in ultrarelativistic heavy-ion collisions", *Phys. Rev. C*, vol. 65, no. 2, p. 024 902. DOI: `10.1103/PhysRevC.65.024902`. arXiv: `nucl-th/0110027`.

[83] M. Jacob, "$\Lambda\overline{\Lambda}$ longitudinal polarization: A signature for the formation of a quark-gluon plasma in heavy ion collisions", *Z. Phys. C*, vol. 38, no. 1, pp. 273–276. DOI: `10.1007/BF01574549`.

[84] G. Herrera, J. Magnin, and L. M. Montaño, "Longitudinal $\overline{\Lambda}_0$ polarization in heavy-ion collisions as a probe for QGP formation", *Eur. Phys. J. C*, vol. 39, no. 1, pp. 95–99. DOI: `10.1140/epjc/s2004-02073-2`. arXiv: `hep-ph/0411019`.

[85] B. L. Ioffe and D. E. Kharzeev, "Quarkonium polarization in heavy ion collisions as a possible signature of the quark-gluon plasma", *Phys. Rev. C*, vol. 68, no. 6, p. 061 902. DOI: `10.1103/PhysRevC.68.061902`. arXiv: `hep-ph/0306176`.

[86] E. L. Bratkovskaya, W. Cassing, and U. Mosel, "Probing hadronic polarizations with dilepton anisotropies", *Z. Phys. C*, vol. 75, no. 1, pp. 119–126. DOI: `10.1007/s002880050453`. arXiv: `nucl-th/9605025`.

[87] Z.-T. Liang and X.-N. Wang, "Globally polarized quark-gluon plasma in noncentral $A + A$ collisions", *Phys. Rev. Lett.*, vol. 94, no. 10, p. 102 301. DOI: `10.1103/PhysRevLett.94.102301`. arXiv: `nucl-th/0410079`.

[88] Z.-T. Liang and X.-N. Wang, "Spin alignment of vector mesons in non-central A+A collisions", *Phys. Lett. B*, vol. 629, no. 1, pp. 20–26. DOI: `10.1016/j.physletb.2005.09.060`. arXiv: `nucl-th/0411101`.

[89] B. I. Abelev et al., "Global polarization measurement in Au+Au collisions", *Phys. Rev. C*, vol. 76, no. 2, p. 024 915. DOI: `10.1103/PhysRevC.76.024915`.

[90] L. Adamczyk et al., "Global Λ hyperon polarization in nuclear collisions", *Nature*, vol. 548, no. 7665, pp. 62–65. DOI: `10.1038/nature23004`. arXiv: `1701.06657 [nucl-ex]`.

[91] S. Acharya, D. Adamová, S. P. Adhya, and A. Adler, "Global polarization of Λ and $\overline{\Lambda}$ hyperons in Pb-Pb collisions at $\sqrt{s_{NN}}$ = 2.76 and 5.02 TeV", *Phys. Rev. C*, vol. 101, no. 4, p. 044 611. DOI: `10.1103/PhysRevC.101.044611`.

[92] R. Abou Yassine et al., "Measurement of global polarization of Λ hyperons in few-GeV heavy-ion collisions", *Phys. Lett. B*, vol. 835, p. 137 506. DOI: `10.1016/j.physletb.2022.137506`.

[93] J. Adam et al., "Global polarization of Ξ and Ω hyperons in Au + Au collisions at $\sqrt{s_{NN}}$ = 200 GeV", *Phys. Rev. Lett.*, vol. 126, no. 16, p. 162 301. DOI: `10.1103/PhysRevLett.126.162301`. arXiv: `2012.13601 [nucl-ex]`.

[94] J. Adam et al., "Polarization of Λ ($\overline{\Lambda}$) hyperons along the beam direction in Au + Au collisions at $\sqrt{s_{NN}}$ = 200 GeV", *Phys. Rev. Lett.*, vol. 123, no. 13, p. 132 301. DOI: `10.1103/PhysRevLett.123.132301`.

[95] S. Acharya et al., "Polarization of Λ and $\overline{\Lambda}$ Hyperons along the Beam Direction in Pb-Pb Collisions at $\sqrt{s_{NN}}$ = 5.02 TeV", *Phys. Rev. Lett.*, vol. 128, no. 17, p. 172 005. DOI: `10.1103/PhysRevLett.128.172005`.

[96] W. Florkowski, B. Friman, A. Jaiswal, and E. Speranza, "Relativistic fluid dynamics with spin", *Phys. Rev. C*, vol. 97, no. 4, p. 041 901. DOI: `10.1103/PhysRevC.97.041901`. arXiv: `1705.00587 [nucl-th]`.

[97] F. Becattini and M. A. Lisa, "Polarization and vorticity in the quark–gluon plasma", *Annu. Rev. Nucl. Part. Sci.*, vol. 70, pp. 395–423. DOI: `10.1146/annurev-nucl-021920-095245`.

[98] V. L. Lyuboshitz and V. V. Lyuboshitz, "Spin correlations in the $\Lambda\Lambda$ and $\Lambda\overline{\Lambda}$ systems generated in relativistic heavy-ion collisions", *Phys. At. Nucl.*, vol. 73, no. 5, pp. 805–814. DOI: `10.1134/S106377881005008X`.

[99] Z.-B. Kang, K. Lee, and F. Zhao, "Polarized jet fragmentation functions", *Phys. Lett. B*, vol. 809, p. 135 756. DOI: `10.1016/j.physletb.2020.135756`.

[100] U. D'Alesio, L. Gamberg, F. Murgia, and M. Zaccheddu, "Transverse Λ polarization in unpolarized $pp \to$ jet $\Lambda^{\uparrow} X$", *Phys. Lett. B*, vol. 851, p. 138 552. DOI: `10.1016/j.physletb.2024.138552`.

[101] S. Khan et al., "Machine learning application for Λ hyperon reconstruction in CBM at FAIR", *EPJ Web Conf.*, vol. 259, p. 13 008. DOI: `10.1051/epjconf/202225913008`.

[102] V. P. Ladygin, A. P. Jerusalimov, and N. B. Ladygina, "Polarization of Λ^0 hyperons in nucleus-nucleus collisions at high energies", *Phys. Part. Nucl. Lett.*, vol. 7, no. 5, pp. 349–354. DOI: `10.1134/S1547477110050080`. arXiv: `0806.3867` [`nucl-ex`].

[103] "NICA White Paper", NICA, Tech. Rep., Jan. 2014. [Online]. Available: `https://mpdroot.jinr.ru/wp-content/uploads/2020/01/WhitePaper_10.01.pdf`.

[104] J. Drnoyan, E. Levterova, V. Vasendina, A. Zinchenko, and D. Zinchenko, "Perspectives of Multistrange Hyperon Study at NICA/MPD from Realistic Monte Carlo Simulation", *Phys. Part. Nucl. Lett.*, vol. 17, no. 1, pp. 32–43. DOI: `10.1134/S1547477120010057`.

[105] E. Nazarova, R. Akhat, M. Baznat, O. Teryaev, and A. Zinchenko, "Monte Carlo Study of Λ Polarization at MPD", *Phys. Part. Nucl. Lett.*, vol. 18, no. 4, pp. 429–438. DOI: `10.1134/S1547477121040142`.

[106] LHCb, "LHCb SMOG Upgrade", CERN, Geneva, Tech. Rep., 2019. DOI: `10.17181/CERN.SAQC.EOWH`.

[107] A. Bursche et al., "Physics opportunities with the fixed-target program of the LHCb experiment using an unpolarized gas target", CERN, Tech. Rep., 2018. [Online]. Available: `https://cds.cern.ch/record/2649878/`.

[108] S. Afanasiev et al., "The NA49 large acceptance hadron detector", *Nucl. Instrum. Meth. A*, vol. 430, pp. 210–244. DOI: `10.1016/S0168-9002(99)00239-9`.

[109] M. Gazdzicki, M. Gorenstein, and P. Seyboth, "Onset of Deconfinement in Nucleus–Nucleus Collisions: Review for Pedestrians and Experts", *Acta Phys. Polon. B*, vol. 42, no. 2, p. 307. DOI: `10.5506/aphyspolb.42.307`.

[110] Z. Fodor and S. D. Katz, "Critical point of QCD at finite T and μ, lattice results for physical quark masses", *JHEP*, vol. 2004, no. 04, p. 050. DOI: `10.1088/1126-6708/2004/04/050`.

[111] K. Abe et al., "The T2K experiment", *Nucl. Instrum. Meth. A*, vol. 659, no. 1, pp. 106–135. DOI: `10.1016/j.nima.2011.06.067`.

[112] L. Aliaga et al., "Design, calibration, and performance of the MINERvA detector", *Nucl. Instrum. Meth. A*, vol. 743, pp. 130–159. DOI: `10.1016/j.nima.2013.12.053`.

[113] D. S. Ayres et al., "The NOvA Technical Design Report", Tech. Rep., Oct. 2007. DOI: `10.2172/935497`. [Online]. Available: `https://inspirehep.net/files/1e897a237c85bae0087a7f644e9ad832`.

[114] R. Acciarri et al., *Long-Baseline Neutrino Facility (LBNF) and Deep Underground Neutrino Experiment (DUNE) conceptual design report volume 2: The physics program for DUNE at LBNF*, 2016. arXiv: `1512.06148 [physics.ins-det]`.

[115] J. Abraham et al., "Properties and performance of the prototype instrument for the Pierre Auger Observatory", *Nucl. Instrum. Meth. A*, vol. 523, no. 1, pp. 50–95. DOI: `10.1016/j.nima.2003.12.012`.

[116] G. Navarra et al., "KASCADE-Grande: A large acceptance, high-resolution cosmic-ray detector up to 10^{18} eV", *Nucl. Instrum. Meth. A*, vol. 518, no. 1, pp. 207–209. DOI: `10.1016/j.nima.2003.10.061`.

[117] Y. Génolini, D. Maurin, I. V. Moskalenko, and M. Unger, "Current status and desired precision of the isotopic production cross sections relevant to astrophysics of cosmic rays. II. Fluorine to silicon and updated results for Li, Be, and B", *Phys. Rev. C*, vol. 109, no. 6, p. 064 914. DOI: `10.1103/PhysRevC.109.064914`. arXiv: `2307.06798 [astro-ph.HE]`.

[118] N. Abgrall et al., "Measurement of negatively charged pion spectra in inelastic p+p interactions at p_{lab} = 20, 31, 40, 80 and 158 GeV/c", *Eur. Phys. J.*, vol. C74, p. 2794. DOI: `10.1140/epjc/s10052-014-2794-6`.

[119] N. Abgrall et al., "Measurements of cross sections and charged pion spectra in proton-carbon interactions at 31 GeV/*c*", *Phys. Rev. C*, vol. 84, p. 034 604. DOI: `10.1103/PhysRevC.84.034604`. arXiv: `1102.0983 [hep-ex]`.

[120] N. Abgrall et al., "Measurements of production properties of K_S^0 mesons and Λ hyperons in proton-carbon interactions at 31 GeV/*c*", *Phys. Rev. C*, vol. 89, no. 2, p. 025 205. DOI: `10.1103/PhysRevC.89.025205`. arXiv: `1309.1997 [physics.acc-ph]`.

[121] W. Blum, L. Rolandi, and W. Riegler, *Particle detection with drift chambers* (Particle Acceleration and Detection). Springer, 2008, ISBN: 978-3-540-76684-1. DOI: `10.1007/978-3-540-76684-1`.

[122] K. Werner, F.-M. Liu, and T. Pierog, "Parton ladder splitting and the rapidity dependence of transverse momentum spectra in deuteron-gold collisions at RHIC", *Phys. Rev.*, vol. C74, p. 044 902. DOI: `10.1103/PhysRevC.74.044902`. arXiv: `hep-ph/0506232`.

[123] T. Pierog and K. Werner, "EPOS Model and Ultra High Energy Cosmic Rays", *Nucl. Phys. B Proc. Suppl.*, vol. 196, pp. 102–105. DOI: `10.1016/j.nuclphysbps.2009.09.017`. arXiv: `0905.1198 [hep-ph]`.

[124] R. Ulrich, T. Pierog, and C. Baus, *Cosmic ray monte carlo package, crmc*, Aug. 2021. DOI: `10.5281/zenodo.5270381`. [Online]. Available: `https://gitlab.iap.kit.edu/AirShowerPhysics/crmc`.

[125] B. Andersson, G. Gustafson, and B. Nilsson-Almqvist, "A model for low-p_T hadronic reactions with generalizations to hadron-nucleus and nucleus-nucleus collisions", *Nucl. Phys. B*, vol. 281, no. 1, pp. 289–309. DOI: `10.1016/0550-3213(87)90257-4`.

[126] B. Nilsson-Almqvist and E. Stenlund, "Interactions between hadrons and nuclei: The Lund Monte Carlo - FRITIOF version 1.6 -", *Comput. Phys. Commun.*, vol. 43, no. 3, pp. 387–397. DOI: `10.1016/0010-4655(87)90056-7`.

[127] S. Agostinelli et al., "GEANT4: A Simulation toolkit", *Nucl. Instrum. Meth.*, vol. A506, p. 250. DOI: `10.1016/S0168-9002(03)01368-8`.

[128] J. Allison et al., "Geant4 developments and applications", *IEEE Trans. Nucl. Sci.*, vol. 53, p. 270. DOI: `10.1109/TNS.2006.869826`.

[129] J. Allison et al., "Recent developments in Geant4", *Nucl. Instrum. Methods Phys. Res. A*, vol. 835, pp. 186–225. DOI: `10.1016/j.nima.2016.06.125`.

[130] R. Brun and F. Carminati, "GEANT detector description and simulation tool", CERN, note, 1993. [Online]. Available: `https://cds.cern.ch/record/1082634/files/geantall_CERN-W5013.pdf`.

[131] "DSPACK software package", Tech. Rep. [Online]. Available: `http://na49info.web.cern.ch/na49info/na49/Software/DSPACK/`.

[132] R. Brun and F. Rademakers, "ROOT: An object oriented data analysis framework", *Nucl. Instrum. Meth. A*, vol. 389, M. Werlen and D. Perret-Gallix, Eds., pp. 81–86. DOI: `10.1016/S0168-9002(97)00048-X`. [Online]. Available: `root.cern`.

[133] J. Myrheim and L. Bugge, "A fast Runge-Kutta method for fitting tracks in a magnetic field", *Nucl. Instrum. Meth.*, vol. 160, no. 1, pp. 43–48. DOI: `10.1016/0029-554X(79)90163-0`.

[134] J. Podolanski and R. Armenteros, "III. Analysis of V-events", *Lond. Edinb. Dubl. Phil. Mag.*, vol. 45, no. 360, pp. 13–30. DOI: `10.1080/14786440108520416`.

[135] K. Levenberg, "A method for the solution of certain non-linear problems in least squares", *Quarterly of Applied Mathematics*, vol. 2, no. 2, pp. 164–168. DOI: `10.1090/qam/10666`.

[136] D. W. Marquardt, "An algorithm for least-squares estimation of nonlinear parameters", *J. Soc. Indust. Appl. Math.*, vol. 11, no. 2, pp. 431–441. DOI: `10.1137/0111030`.

[137] N. Abgrall, "Report from the NA61/SHINE experiment at the CERN SPS", CERN, Geneva, Tech. Rep., 2010. [Online]. Available: `https://cds.cern.ch/record/1292313`.

[138] G. Stefanek, *Elliptical flow and event-by-event fluctuations in heavy ion collisions at SPS energies*. Uniwersytet Jana Kochanowskiego, 2016, p. 168, ISBN: 978-83-7133-664-5.

[139] G. I. Veres, "Baryon momentum transfer in hadronic and nuclear collisions at the CERN NA49 experiment", Ph.D. dissertation, Eötvös Loránd University, Budapest, 2001. [Online]. Available: `https://edms.cern.ch/file/818513/1/gabor_veres_phd.ps`.

[140] M. van Leeuwen, "A practical guide to dE/dx analysis in NA49", CERN EDMS, note, 2008. [Online]. Available: `https://edms.cern.ch/ui/file/983015/2/na49_dedx_mvanleeuwen.pdf`.

[141] G. I. Veres, "New developments in understanding and correction of dE/dx", CERN EDMS, note, 2007. [Online]. Available: `https://edms.cern.ch/ui/file/815871/1/note.pdf`.

[142] M. van Leeuwen, "Kaon and open charm production in central lead-lead collisions at the CERN SPS", Ph.D. dissertation, NIKHEFF, Amsterdam, 2003. [Online]. Available: `https://cds.cern.ch/record/624231`.

[143] A. Marcinek, "ϕ meson production in proton-proton collisions in the NA61/SHINE experiment at CERN SPS", Ph.D. dissertation, Jagiellonian University, 2016. [Online]. Available: `https://cds.cern.ch/record/2234262`.

[144] A. Aduszkiewicz et al., "Measurements of $\pi^{\pm}$, $K^{\pm}$, p and $\bar{p}$ spectra in proton-proton interactions at 20, 31, 40, 80 and 158 GeV/c with the NA61/SHINE spectrometer at the CERN SPS", *Eur. Phys. J. C*, vol. 77, no. 10, p. 671. DOI: `10.1140/epjc/s10052-017-5260-4`.

[145] A. Aduszkiewicz et al., "Production of Λ-hyperons in inelastic p+p interactions at 158 GeV/c", *"Eur. Phys. J. C"*, vol. 76, no. 4, p. 198. DOI: `10.1140/epjc/s10052-016-4003-2`.

[146] G. Cowan, *Statistical data analysis*. Oxford University Press, 1998, ISBN: 9780198501558.

[147] W. Verkerke and D. Kirkby, "RooFit Users Manual", CERN, Tech. Rep., 2019. [Online]. Available: `https://root.cern/download/doc/RooFit_Users_Manual_2.91-33.pdf`.

[148] "MINUIT 2 (C++ port of MINUIT library)", Tech. Rep. [Online]. Available: `http://www.cern.ch/minuit`.

[149] F. James and M. Roos, "Minuit - a system for function minimization and analysis of the parameter errors and correlations", *Comput. Phys. Commun.*, vol. 10, no. 6, pp. 343–367. DOI: `10.1016/0010-4655(75)90039-9`.

[150] F. James, "Interpretation of errors in MINUIT", Tech. Rep. [Online]. Available: `http://seal.web.cern.ch/seal/documents/minuit/mnerror.pdf`.

[151] L. Brenner et al., "Comparison of unfolding methods using RooFitUnfold", *Int. J. Mod. Phys. A*, vol. 35, no. 24, p. 2 050 145. DOI: `10.1142/S0217751X20501456`. arXiv: `1910.14654 [physics.data-an]`. [Online]. Available: `https://gitlab.cern.ch/RooUnfold/RooUnfold/`.

[152] G. Bohm and G. Zech, *Introduction to statistics and data analysis for physicists*. Hamburg: DESY, 2014, ISBN: 978-3-935702-88-1. DOI: `10.3204/DESY-BOOK/statistics`.

[153] G. D'Agostini, "A multidimensional unfolding method based on Bayes' theorem", *Nucl. Instrum. Methods Phys. Res. A*, vol. 362, no. 2, pp. 487–498. DOI: `10.1016/0168-9002(95)00274-X`.

[154] C. Langenbruch, "Parameter uncertainties in weighted unbinned maximum likelihood fits", *Eur. Phys. J. C*, vol. 82, no. 5. DOI: `10.1140/epjc/s10052-022-10254-8`.

[155] J. D. Jackson, *Classical Electrodynamics*, 3rd ed. Wiley, 1999, ISBN: 978-0-471-30932-1.

[156] B. Efron, "Bootstrap Methods: Another Look at the Jackknife", *Ann. Statist.*, vol. 7, no. 1, pp. 1–26. DOI: `10.1214/aos/1176344552`.

[157] A. M. Smith et al., "$\Lambda 0$ polarization in proton-proton interactions from $\sqrt{s} = 31$ to 62 GeV", *Phys. Lett. B*, vol. 185, no. 1. DOI: `10.1016/0370-2693(87)91556-5`.

[158] M. Tanabashi et al., "Review of Particle Physics", *Phys. Rev. D*, vol. 98, p. 030 001. DOI: `10.1103/PhysRevD.98.030001`.

[159] A. Aduszkiewicz et al., "A high-resolution pixel silicon Vertex Detector for open charm measurements with the NA61/SHINE spectrometer at the CERN SPS", *Eur. Phys. J. C*, vol. 83, no. 6, p. 471. DOI: `10.1140/epjc/s10052-023-11624-6`.

[160] P. von Doetinchem, "Addendum to the NA61/SHINE Proposal: Request for high-statistics p+p measurements in Run 3", CERN, Geneva, Tech. Rep., 2024. [Online]. Available: `https://cds.cern.ch/record/2914265`.

[161] R. P. Feynman, "Very high-energy collisions of hadrons", *Phys. Rev. Lett.*, vol. 23, no. 24, pp. 1415–1417. DOI: `10.1103/PhysRevLett.23.1415`.

[162] M. Abramowitz and I. A. Stegun, Eds., *Handbook of Mathematical Functions with Formulas, Graphs, and Mathematical Tables*, Tenth Printing. Washington, DC, USA: U.S. Government Printing Office, 1972, pp. 555–566.

[163] M. L. Faccini-Turluer et al., "Λ and $\overline{\Lambda}$ polarization in $K^{\pm}P$ interactions at 32 GeV/c France-Soviet Union and CERN-Soviet Union collaborations", *Z. Phys. C*, vol. 1, no. 1, pp. 19–24. DOI: `10.1007/BF01450377`.

List of Figures

List of Tables

Yehor Bondar
....
Imię i nazwisko doktoranta

Kielce, dn....29.09.2025.

....
PESEL

Nauk Ścisłych i
Przyrodniczych
Sekcja/dyscyplina

Nauki Fizyczne
....
Dyscyplina naukowa/artystyczna

OŚWIADCZENIE

Przedkładając rozprawę doktorską pod tytułem ....

Lambda transverse polarization in proton-proton interactions in NA61/SHINE

at the CERN SPS
....

oświadczam, że:

[X] pracę napisałam/napisałem* samodzielnie,

[X] praca nie stanowi istotnego fragmentu lub innych elementów cudzego utworu,

[X] praca nie narusza żadnych innych istniejących praw autorskich,

[X] wykorzystane w pracy materiały źródłowe zastosowane zostały z zachowaniem zasad prawa cytatu,

[X] przedstawiona praca w całości ani też w części nie była wcześniej podstawą do ubiegania się o nadanie stopnia naukowego doktora,

[X] wersja elektroniczna (na nośniku elektronicznym) pracy jest tożsama z wersją drukowaną.

....
data i czytelny podpis wnioskodawcy

*niewłaściwe skreślić